MULTISCALE MODELING OF LI-ION CELLS: MECHANICS, HEAT GENERATION AND ELECTROCHEMICAL KINETICS

by

Xiangchun Zhang

A dissertation submitted in partial fulfillment
of the requirements for the degree of
Doctor of Philosophy
(Mechanical Engineering)
in The University of Michigan
2009

Doctoral Committee:

Professor Ann Marie Sastry, Co-Chair
Professor Wei Shyy, Co-Chair
Professor James R. Barber
Professor Levi T. Thompson Jr

To My Parents Xueqin Liu and Lixian Zhang

ACKNOWLEDGEMENTS

First of all, I would like to express my grateful thanks to my research advisors Professor Ann Marie Sastry and Professor Wei Shyy for their guidance and support. I am very grateful that they led me into this interesting and important topic of Li-ion battery research that is the key to solving global energy and environmental problems. I appreciate the opportunity I had to work with these two true scholars and professionals. From the wonderful experience working with my two advisors, I learned fundamental science and engineering and also professional skills.

Many thanks go to my committee members, Prof. Levi T. Thompson and Prof. James R. Barber, for serving on my committee and providing valuable advice on my thesis.

I would also like to thank the current and former members of both Sastry group and Shyy group, Dr. Fabio Albano, Dr. Hikaru Aono, Dr. Yen-Hung Chen, Mr. Young-Chang Cho, Mr. Myoungdo Chung, Mr. Wenbo Du, Mr. Sangwoo Han, Mr. Ez Hassan, Dr. Munish V. Inamdar, Ms. Qiuye Jin, Mr. Chang-Kwon Kang, Dr. HyonCheol Kim, Mr. Chih-Kuang Kuan, Dr. Jonghyun Park, Dr. Myounggu Park, Dr. Jeong Hun Seo, Mr. Jaeheon Sim, Mr. Dong Hoon Song, Mr. Emre Sozer, Dr. Jian Tang, Mr. Patrick Trizila, Mr. Chien-Chou Tseng, Mr. Peter Verhees, Dr. Chia-Wei Wang, Mr. Seokjun Yun, and Mr. Min Zhu, for their support and sharing wonderful moments during the past years.

I really appreciate the help from Ms. Lisa Szuma and Ms. Eve Bernos for meeting

scheduling and other administrative matters.

I specially thank Dr. Tushar Goel and Mr. Felipe A. C. Viana for the help on using Surrogate Toolbox.

I gratefully acknowledge the support of my research sponsors, including the U.S. Department of Energy through the BATT program (Dr. Tien Duong, Program Manager), Ford Motor Company (Mr. Ted Miller and Mr. Kent Snyder, Program Managers), NASA under the Constellation University Institute Program (CUIP) (Ms. Claudia Meyer, program monitor), and General Motors Corporation (Mr. Bob Kruse, GM/UM ABCD Co-Director).

TABLE OF CONTENTS

DEDICATION ii

ACKNOWLEDGEMENTS iii

LIST OF TABLES viii

LIST OF FIGURES ix

LIST OF SYMBOLS xi

LIST OF ABBREVIATIONS xiv

ABSTRACT xv

CHAPTER I. INTRODUCTION 1

LI-ION BATTERY TECHNOLOGY: A SOLUTION TO GLOBAL ENERGY AND ENVIRONMENT PROBLEMS 1

LI-ION BATTERY RESEARCH OVERVIEW 3

Selected Research on Novel Materials 5

Selected Research on Cell Diagnosis and Testing 8

Selected Research on Cell Modeling, Simulations and Optimization 10

STRESS AND HEAT GENERATION INSIDE ELECTRODE PARTICLES 10

MULTISCALE MODELING OF LI-ION BATTERIES 13

Homogenization Approach 15

Volume Averaging 16

Scale Bridging 18

SURROGATE-BASED MODELING AND ANALYSIS 20

SCOPE AND OUTLINE OF THE DISSERTATION 29

BIBLIOGRAPHY 30

CHAPTER II. NUMERICAL SIMULATION OF INTERCALATION-INDUCED STRESS IN LI-ION BATTERY ELECTRODE PARTICLES 36

INTRODUCTION 36
METHODS 39
Stress-Strain Relations 39
Diffusion Equation 41
Numerical Methods 43
Material Properties 47
RESULTS AND DISCUSSION 49
1D Finite Difference Simulations 49
3D Finite Elements Simulation Results 54
CONCLUSION 63
BIBLIOGRAPHY 64
CHAPTER III. SURROGATE-BASED ANALYSIS OF STRESS AND HEAT GENERATION WITHIN SINGLE CATHODE PARTICLES UNDER POTENTIODYNAMIC CONTROL 66
INTRODUCTION 66
ELECTROCHEMICAL, MECHANICAL AND THERMAL MODELING 69
Model of Intercalation 71
Intercalation-Induced Stress Model 75
Heat Generation Model 77
Spherical Particle Simulation Results 80
SURROGATE-BASED ANALYSIS OF ELLIPSOIDAL PARTICLES UNDER DIFFERENT CYCLING RATES 88
Selection of Variables And Design of Experiments 91
Model Construction and Validation 94
Analysis Based on Obtained Surrogate Models 97
ASSUMPTION OF A UNIFORM ELECTRIC POTENTIAL 100
CONCLUSIONS 104
BIBLIOGRAPHY 106
CHAPTER IV. SURROGATE-BASED SCALE BRIDGING AND MICROSCOPIC SCALE MODELING OF CATHODE ELECTRODE MATERIALS 110
INTRODUCTION 110
Challenges for Li-Ion Battery Modeling 110
Review of the Existing Li-Ion Battery Modeling Work in the Literature 112
The Objectives of This Study 115

METHODS 116
Li-Ion Cell Cycling Mechanisms and Governing Equations on Microscopic Scale ... 116
Multiscale Modeling Framework 121
3D Microscopic Modeling of Electrode Particle Clusters 129
Surrogate-Based Scale Bridging 133
Summary of the Multiscale Modeling Framework 136
RESULTS AND DISCUSSION 138
Analysis of 3D Microscopic Simulation Results 138
Effective Material Property Calculations 146
Surrogate Model Construction for Reaction Current Density 148
CONCLUSIONS 152
BIBLIOGRAPHY 155
CHAPTER V. CONCLUSIONS AND FUTURE WORK 158

LIST OF TABLES

Table 1.1: Comparison of key battery technologies.. 2

Table 2.1: Stress and strain in cathode materials in the intercalation process.. 37

Table 2.2: Material properties of Mn_2O_4.. 48

Table 3.1: Representative cathode compositions and particle sizes.. 70

Table 3.2: Parameters and material properties for the intercalation model (where r_0 is the radius of a spherical particle).. 76

Table 3.3: Averaged heat generation rates during charge process.. 90

Table 3.4: Design variables and design space..... 93

Table 3.5: Evaluation of the response surface approximations..... 96

Table 3.6: Global sensitivity indices (total effect) for stress and resistive heat.. 101

Table 4.1: Characteristic time scales for physicochemical processes inside a Li-ion battery..... 113

Table 4.2: Material properties for 3D microscopic scale simulations..... 132

Table 4.3: Input variables and their range for 3D microscopic scale simulations.. 135

Table 4.4: Comparison of simulation results from pseudo 2D and 3D microscopic models..... 142

Table 4.5: Ratio between effective and bulk (intrinsic) transport properties.. 147

Table 4.6: Evaluation of the constructed surrogate models.. 149

Table 4.7: Global sensitivity indices calculated from kriging model. 153

LIST OF FIGURES

Figure 1.1: Schematic diagram of a Li-ion cell 4

Figure 1.2: EV commercialization Li-ion battery technology spider chart..... 6

Figure 1.3: Experimental observation of fracture in cathode particles: (a) $LiFePO_4$ particle after 60 cycles [24]; (b) gold-codeposited $LiMn_2O_4$ electrode particles after cyclic voltammetric tests at a scan rate of 4mV/s [25]; (c)$LiCoO_2$ particles after 50 cycles [26]. 12

Figure 1.4: Summary of scale bridging approaches. 19

Figure 1.5: Surrogate modeling: (a) key steps of surrogate modeling; (b) design of experiments by FCCD; (c) design of experiments by LHS. 22

Figure 1.6: An example of various surrogate models constructed based on training data obtained from the analytical function y=exp(x^4)..... 25

Figure 2.1: Comparison of simulation results of two models. 50

Figure 2.2: Maximum dimensionless radial stress versus dimensionless current density. 51

Figure 2.3: Numerical results for the effects of stress. 53

Figure 2.4: Convergence plot of finite element solutions for: (a) hydrostatic stress and (b) concentration. 55

Figure 2.5: Schematic of an ellipsoidal particle, with coordinate system. 57

Figure 2.6: Solutions at the end of discharge for an ellipsoid of aspect ratio 1.953, (a) concentration, (b) von Mises stress, and (c) shear stress 58

Figure 2.7: Maximum von Mises stress during discharge, for various ellipsoids..... 59

Figure 2.8: The effect of aspect ratio, for fixed particle volume 60

Figure 2.9: The effect of aspect ratio, for fixed shorter semi axes..... 62

Figure 3.1: Potentials: (a) OCP of $LiMn_2O_4$ and (b) applied potential sweeping profile during one cycle.. 74

Figure 3.2: Material properties: (a) the derivative of OCP over temperature: curve fitting of the measured data from Ref. 20, and (b) the derivative of partial molar enthalpy over concentration obtained by $\partial \bar{H} / \partial c = -F \partial \left(U - T \mathrm{d}u / \mathrm{d}T \right) / \partial c$ based on the curve fit in (a)..... 79

Figure 3.3: Simulation results of a spherical particle with $v = 0.4\mathrm{mV/s}$, $r_0 = 5\mu m$: (a) diffusion flux on the particle surface, (b) radial stress at the center of the particle, and (c) von Mises stress on the particle surface.. 81

Figure 3.4: Simulation results of a spherical particle in the charge half cycle ($v = 0.4\mathrm{mV/s}$, $r_0 = 5\mu m$): (a) reaction flux on the particle surface, (b) von Mises stress on the particle surface, (c) surface overpotential, and (d) exchange current density (divided by Faraday's constant)..... 83

Figure 3.5: Distribution of lithium-ion concentration inside a spherical particle at different time instants during the charge half cycle..... 85

Figure 3.6: Simulation results of a spherical particle under 20C charge: (a) reaction flux on the particle surface, and (b) von Mises stress on the particle surface.. 87

Figure 3.7: Simulation results of various heat generation sources during the charge half cycle: (a) resistive heating, (b) entropic heating, and (c) heat of mixing..... 89

Figure 3.8: Geometric illustration of an ellipsoidal particle.. 92

Figure 3.9: The dependency between objective functions and design variables (a) maximum von Mises stress (in megapascal), (b) time-averaged resistive heat rate (in picowatts).. 98

Figure 3.10: Simulation with a predescribed potential variation: (a) potential variation on particle surface at t=1534s, (b) time history of von Mises stress on particle surface, (c) concentration distribution inside the particle at t=1534s, and (d) von Mises stress distribution inside the particle at t=1534s..... 103

Figure 4.1: Scales in Li-ion batteries: (a) dimension for a single cell, (b) components and their dimensions inside a single cell along the thickness direction, and (c) a SEM image for $LiMn_2O_4$ positive electrode.. 111

Figure 4.2: Surrogate-based scale bridging for multiscale modeling framework.. 130

Figure 4.3: Summary of the multiscale framework. 137

Figure 4.4: Generated microstructure: (a) liquid phase of electrolyte, (b) solid phase of active material, and (c) the whole simulation domain containing both phases.. 139

Figure 4.5: Results of a 3D microscopic scale simulation: (a) Li-ion concentration in the solid phase (mol/m^3), (b) Li-ion concentration in the liquid phase (mol/m^3), and (c) reaction current density at the phase interface (A/m^2).. 140

Figure 4.6: Comparison of (normalized) reaction current density: (a) the temporal variation for pseudo 2D and 3D microscopic models, (b) distribution of reaction current density (A/m^2) at t=10.77min by 3D microscopic model, and (c) distribution of reaction current density (A/m^2) at t=26.16min by 3D microscopic model..... 145

Figure 4.7: Histogram of surrogate model prediction errors on 21 testing points.. 151

LIST OF SYMBOLS

a , b , c	lengths of the three semi-axes of ellipsoid	μm
a	specific interfacial area	m^2/m^3 (or m^{-1})
c	concentration of lithium ions	$mol\,m^{-3}$
$\tilde{c}$	concentration change from initial value	$mol\,m^{-3}$
C_p	heat capacity	J/(mol-kg)
D	lithium diffusion coefficient	$m^2\ s^{-1}$
E	Young's modulus	GPa
F	Faraday's constant	96487 C mol^{-1}
f	molar activity coefficient of the electrolyte	
g_s	volume fraction of phase s	
ΔH	enthalpy of reaction	J mol^{-1}
$\overline{H}$	partial molar enthalpy	J mol^{-1}
I	dimensionless current density	
I	current of cell	A
$\mathbf{i}_n$ (i_n)	current density vector (scalar)	A m^{-2}
i_0	exchange current density	A m^{-2}
$\mathbf{J}$ (J)	species flux vector (scalar)	$mol\,m^{-2}\ s^{-1}$
k	reaction constant	$m^{5/2}s^{-1}mol^{-1/2}$
k_x , k_y , k_z	thermal conductivity	W/(K-m)
M	mobility	$m^2 \cdot mol/(J \cdot s)\,A$
N_s	number of sampling points	
N_v	dimension of the design space	
$\dot{Q}$	heat transfer/generation rate	W

R	gas constant	$8.314\ \mathrm{J\ mol^{-1}\ K^{-1}}$
$\overline{R}$	equivalent radius of ellipsoidal particles	μm
R^2_{adj}	adjusted coefficient of multiple determination	
r_0	particle radius	μm
r_k	rate of reaction k	$\mathrm{mol\ s^{-1}}$
T	temperature	K
t	time	s
t_+^0	transference number	
U	open circuit potential	V
U_H	enthalpy potential	V
u	displacement	m
$\mathbf{v}$	ion movement velocity inside solid particles	m/s
$V_1(V_2)$	electric potential in solid (liquid) phase	V
V	variance of objective functions in surrogate modeling	
v	potential sweep rate	$\mathrm{mV\ s^{-1}}$
X	molar fraction of lithium in the electrode	
x, y, z	spatial coordinate	μm
y	state of charge	
Z	systematical departure in the kriging model	

Greek symbols

α	aspect ratio	
β	symmetry factor	
β	coefficients in polynomial response surface	
ε	a scale parameter ($\varepsilon << 1$)	
ε_{ij}	strain	
η	surface overpotential	V
σ_1	conductivity of solid phase	s/m
κ	conductivity of liquid phase	s/m
ν	Poisson's ration	

μ	chemical potential	J/mol
σ_{ij}	stress	Pa
Ω	partial molar volume	$m^3\ mol^{-1}$
ρ	density	kg/m^3

Subscripts:

0	exchange current density i_0; particle radius r_0; initial concentration c_0
1	solid phase
2	liquid phase
adj	adjusted (coefficient of multiple determination)
avg	time averaged (heat generation rate)
e	entropic heat
g	heat generation
h	hydrostatic (stress)
i, j	index for tensor elements, or index of species
k	index for a chemical reaction
l	concentration of Li-ion in the electrolyte
max	maximum
mixing	heat of mixing
r	resistive heating
rad	radial direction
s	concentration of Li-ion in the solid phase
tang	tangential direction
v	von Mises stress
θ	concentration of available vacant sites

Superscripts:

avg	average over volume
bulk	bulk (intrinsic) material properties
eff	effective material properties

Others:

^	dimensionless variables

LIST OF ABBREVIATIONS

AFM	Atomic Force Microscopy
EC	Ethylene Carbonate
EIS	Electrochemical Impedance Spectroscopy
EMC	Ethyl Methyl Carbonate
EV	Electric Vehicle
FCCD	Face Centered Central-Composite Design
LHS	Latin Hypercube Sampling
OCP	Open Circuit Potential
PDE	Partial Differential Equation
PRESS	Prediction Error Sum of Squares
PRS	Polynomial Response Surface
PVdF	Poly Vinylidene Fluoride
RBNN	Radial Basis Neural Network
REV	Representative Elementary Volume
RMS	Root Mean Square
RMSE	Root Mean Square Error
SEI	Solid Electrolyte Interface
SEM	Scanning Electron Microscope
USABC	United States Advanced Battery Consortium
XPS	X-Ray Photoelectron Spectroscopy

ABSTRACT

MULTISCALE MODELING OF LI-ION CELLS: MECHANICS, HEAT GENERATION, AND ELECTROCHEMICAL KINETICS

by

Xiangchun Zhang

Co-Chairs: Ann Marie Sastry and Wei Shyy

To assists implementing Li-ion battery technology in automotive drivetrain electrification, this study focuses on improving calendar life by reducing degradation due to stress-induced electrode particle fracture and heat generation, and creating models for computer simulations that can lead to optimizing battery design.

To improve the calendar life of Li-ion batteries, capacity degradation during battery cycling has to be understood and minimized. One of the degradation mechanisms is fracture of electrode particles due to intercalation-induced stress. A model with the analogy to thermal stress modeling is proposed to determine localized intercalation-induced stress in electrode particles. Intercalation-induced stress is calculated within ellipsoidal electrode particles with a constant diffusion flux assumed at the particle surface. It is found that internal stress gradients significantly enhance diffusion. Simulation results suggest that it is desirable to synthesize electrode particles with smaller sizes and larger aspect ratios, to reduce intercalation-induced stress during cycling of lithium-ion batteries.

Thermal runaway caused by excessive heat generation can lead to catastrophic failure of Li-ion batteries. Stress and heat generation are calculated for single ellipsoidal particles under potentiodynamic control. To systematically investigate how stress and heat generation are affected by electrode particle shape and cycling rate, a surrogate-based analysis is conducted. It is shown that smaller sizes and larger aspect ratios of (prolate) particles reduce the heat and stress generation inside electrode particles.

Battery scale modeling is required for optimizing battery design through computer simulations. To include the electrode microstructure information in battery scale modeling, a multiscale framework is proposed. The resulting closure terms for macroscopic scale governing equations derived from the volume averaging technique are calculated directly from 3D microscopic scale simulations of microstructure consisting of multiple solid electrode particles and liquid electrolyte. It is shown that 3D microscopic simulations give different values for closure terms from the traditional pseudo 2D treatment. To efficiently exchange the information between microscopic and macroscopic scales, a surrogate-based approach is proposed for scale bridging. The surrogate model characterizes the interplay between geometric and physical parameters, and is shown to be able to significantly enhance the macroscopic model.

CHAPTER I

INTRODUCTION

1. LI-ION BATTERY TECHNOLOGY: A SOLUTION TO GLOBAL ENERGY AND ENVIRONMENT PROBLEMS

Ground transportation using gasoline engines is a major factor in global energy and environmental problems. Automotive vehicles contribute a significant portion of the total carbon emissions around the world. In 2003, an estimated 21 percent of world's carbon emissions were generated by the United States. For these 6900 Tg (6.9 billion tons) CO2 equivalent emissions by the U.S. in 2003, the transportation sector accounted for approximately 27 percent of the total. 62 percent of the transportation emissions came from passenger vehicles or light trucks [1]. One solution to energy and environment problems caused by ground transportation is to electrify automotive drivetrains by developing hybrid electric, plug-in hybrid, or pure electric vehicles. Analysis shows that hybrid electric vehicles reduce use phase greenhouse emissions by 30-37% compared to conventional gasoline vehicles, and plug-in hybrid electric vehicles reduce emissions by 38-41% compared to conventional gasoline vehicles [2]. Pure electric vehicles are considered to produce zero carbon emissions during the use phase.

The major candidates for electric vehicle power sources are fuel cells and batteries. Fuel cells are less attractive than batteries due to current issues with hydrogen storage and transportation. Table 1.1 shows a comparison of several key battery

Battery technology / Characteristics	Lead-acid	Nickel-cadmium	Nickel-metal hydride	Lithium-ion
Specific energy (Wh/kg)	10-35	10-40	~75	~150
Energy density (Wh/L)	50-90	40-100	~240	~400
Nominal voltage (V)	2.0	1.2	1.2	4.0
Cycle life (cycles)	200-1500	500-10,000	300-600	1,000+

Table 1.1: Comparison of key battery technologies. [3]

technologies [3]. It is shown that Li-ion batteries have superior voltage, energy per unit mass and per unit volume. For all commercial hybrid vehicles available in the market, nickel metal hydride batteries are used. As shown in Table 1.1, Li-ion batteries have twice the specific energy of nickel metal hydride batteries. Other advantages of Li-ion batteries include no memory effect, broad temperature range of operation, and high rate and high power discharge capability.

2. LI-ION BATTERY RESEARCH OVERVIEW

Figure 1.1 illustrates the electrochemical process within a lithium-ion cell. A cell has one negative and one positive electrode. A separator is used between the two electrodes to prevent short-circuiting. A current collector is attached to each electrode, aluminum for positive and copper for negative electrodes respectively. During the discharge process, lithium ions are extracted from the negative electrode (deintercalation) and inserted into the positive electrode (intercalation). In the recharge process, lithium ions move in the opposite direction. Electrons are conducted through the external circuit corresponding to the movement of lithium ions. The negative electrode of Li-ion batteries commonly uses carbonaceous materials; recently silicon and $Li_4Ti_5O_{12}$ have been proposed for this use. Common positive electrode materials include $LiCoO_2$, $LiNiO_2$, $LiMn_2O_4$, $LiFePO_4$ and $Li(Ni_{1/3}Co_{1/3}Mn_{1/3})O_2$. The porous electrodes consist of active material particles, binders and other additives. The porous configuration of electrodes provides a high surface area for reactions and reduces the distance between reactants and the surface where reactions occur. In the intercalation and deintercalation process, the lattice structure of intercalation hosts changes, causing volume change and strain inside the electrode. The corresponding stress is called intercalation-induced stress. The porous

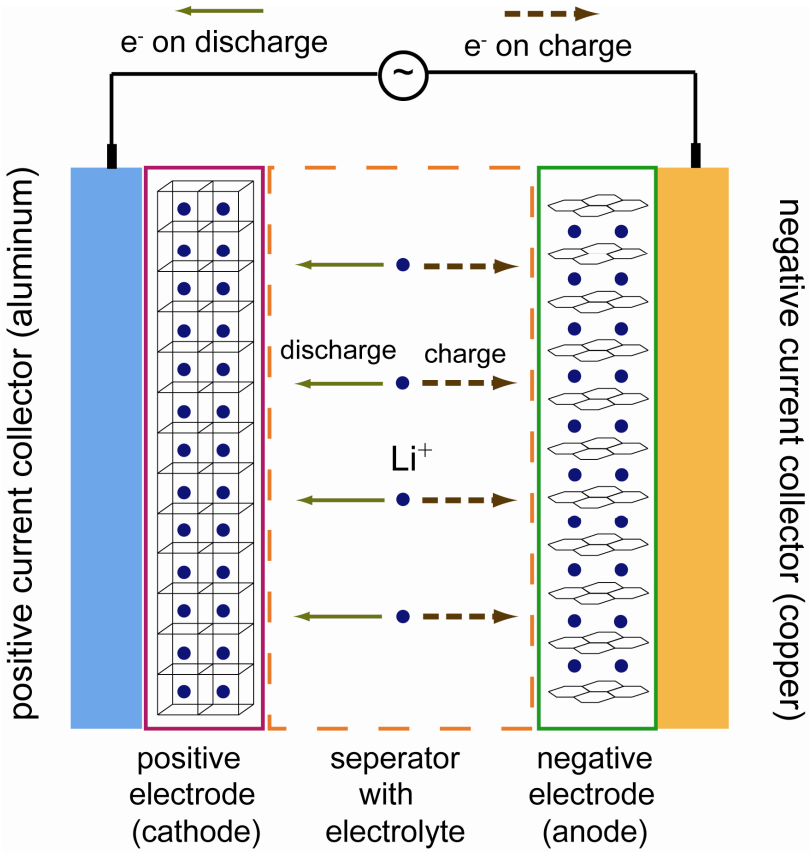

Figure 1.1: Schematic diagram of a Li-ion cell

electrode and separator is filled with electrolyte for transport of Li ions. An example for the most commonly used electrolyte is $LiPF_6$ dissolved in carbonate solvents.

Li-ion batteries are widely used in consumer electronics, such as cell phones and laptop computers, and in military electronics. To successfully implement Li-ion technology in pure electric vehicles, further improvements for Li-ion technology are required. The United States Advanced Battery Consortium (USABC) set goals [4] for advanced batteries for electric vehicles as shown in Figure 1.2. It could be seen that the current Li-ion battery technology fulfills the requirements of cycle life, power density and specific power. However, further improvements in energy density, specific energy, calendar life, operating temperature range and further reduction of cost are required. Moreover, even though the abuse tolerance goal that could not be quantified is not shown in Figure 1.2, improvements are necessary for Li-ion batteries' response to abuse conditions such as crush, overcharge and overheating. Therefore, to successfully implement Li-ion technology in electric vehicles, the following issues have to be addressed: (1) reducing cost, (2) improving calendar life, (3) increasing tolerance to abusive conditions, and (4) further improving energy per unit volume and mass. To address these issues, Li-ion battery related research has concentrated on: (1) novel material synthesis and evaluation, (2) Li-ion cell diagnosis and testing, and (3) cell design optimization through modeling and simulations. Li-ion battery related research is briefly reviewed in the following sections.

2.1. Selected Research on Novel Materials

Novel materials for anode, cathode and electrolyte have been synthesized and evaluated to improve cell performance, life and cost. Carbon materials traditionally used

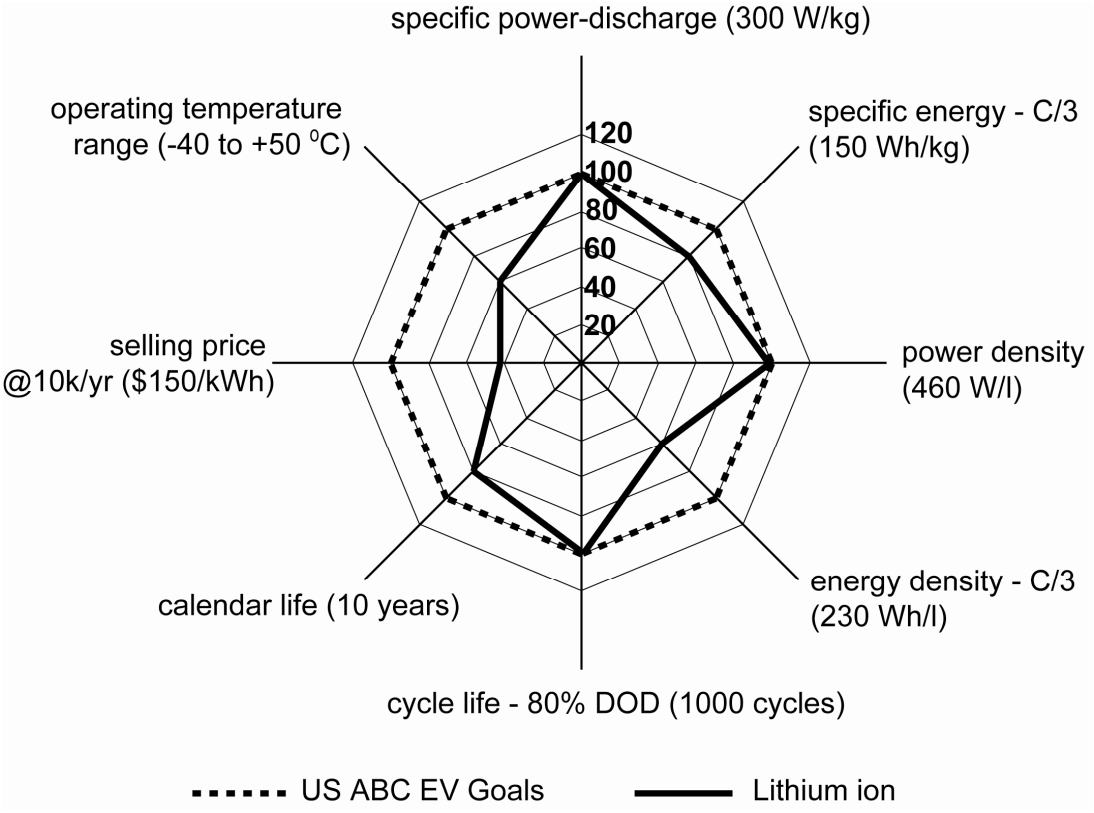

Figure 1.2: EV commercialization Li-ion battery technology spider chart. (The figure is adopted from "Electrochemical Energy Storage Technical Team Technology Development Roadmap" by USABC [4].)

as Li-ion cell anodes give a theoretical capacity 372 mAh/g. To increase this theoretical capacity, silicon was used as anode material because lithium can alloy with Si up to 4.4 per Si that gives a theoretical capacity of 4200mAh/g. However, the excessive expansion and contraction of the alloy lattice structure causes material pulverization that leads to capacity degradation due to loss of electric contact. Nano particles [5] and nanowires [6] have been proposed to solve the excessive volume expansion problem of silicon as an intercalation compound. To completely avoid the volume expansion that might lead to capacity degradation, $Li_4Ti_5O_{12}$ was proposed for anodes as a zero-strain insertion material [7] to improve battery cycle life. Due to the high open circuit potential of $Li_4Ti_5O_{12}$ versus Li, no passivation film is formed during cycling. Therefore, lithium can be inserted and extracted from the compound at a high rate. However, cells using this material as anode have lower voltage output.

For cathode materials, layered structure material $LiCoO_2$ was first used for the first commercial Li-ion cells by Sony Corporation. However, $LiCoO_2$ is expensive and toxic because of the element cobalt. Other cathode candidate materials have been proposed and studied, such as $LiNiO_2$, $LiMn_2O_4$ [8], $LiFePO_4$ [9] and $Li(Ni_{1/3}Co_{1/3}Mn_{1/3})O_2$ [10]. Layer structure material $LiNiO_2$ is thermally instable. Another layer structure $Li(Ni_{1/3}Co_{1/3}Mn_{1/3})O_2$ has the combination of nickel, manganese and cobalt that can provide advantages including higher reversible capacity with milder thermal stability at charged state and lower cost and less toxicity than $LiCoO_2$. However, it is difficult to prepare and synthesize this complicated material. Spinel structure material $LiMn_2O_4$ is inexpensive and environmentally benign, but it has the disadvantage of lower capacity and higher rate of capacity degradation when cycled or stored. Olivine

structure material $LiFePO_4$ has the advantage of low cost, environmentally benignness, and relatively high capacity, but has the disadvantage of low electronic conductivity that results in lower power output. Several approaches were proposed to improve the electronic conductivity of $LiFePO_4$, such as coating the active material with a thin layer of carbon [11, 12], and selective doping with supervalent cations [13].

2.2. Selected Research on Cell Diagnosis and Testing

Li-ion cells and battery have been diagnosed and tested to understand (1) the capacity degradation mechanisms, especially from the aspects of solid-electrolyte interphase (SEI) [14] and material structural change, and (2) the abuse tolerance of cells [15].

Solid electrolyte interphase (SEI), a protective passivation film formed on anode material surfaces during the first charge cycle, decides the retention capacity and storage life of Li-ion batteries because it creates a barrier between the negative electrode and the electrolyte that reduces transfer of electrons from the electrodes to the electrolyte and transfer of solvent molecules and salt anions from the electrolyte to the electrodes. Both *in-situ* and *ex-situ* characterization of SEI layers have been carried out to understand the formation and composition SEI layers. For example, an *ex-situ* study by atomic force microscopy (AFM) and x-ray photoelectron spectroscopy (XPS) revealed the electric potential-dependent character of the surface-film species formation and evidenced a process of dissolution/redeposition of SEI layer in the first five cycles [16]. An *in-situ* electrochemical impedance spectroscopy approach was used to measure the resistance of the SEI layer during cell cycling and it was found that addition of vinylene carbonate (VC) as an additive to $LiPF_6$–ethylene carbonate/ethyl methyl carbonate (EC/EMC)

electrolyte solution helps to reduce SEI layer resistance by forming a high quality SEI film [17].

When active materials of battery electrode undergo electrochemical cycling, they experience phase change and volume expansion/contraction that affects the battery performance. Material structural change during battery cycling has been studied experimentally. For example, an *in-situ* X-Ray diffraction technique was used to study the phase changes and regions of phase stability during the lithiation and delithiation of Si electrodes, and it was found that improved battery cycle life can be obtained if the Si electrodes are cycled above 70mV [18]. An *in-situ* synchrotron X-Ray diffraction technique was used to study the phase changes of $LiMn_2O_4$ cathode materials during cell cycling to understand the capacity fade caused by inhomogenetity of the spinel local structure [19]. The study proposed a phase transition model from a lithium-rich phase to a lithium-deficient phase and finally to a λ-MnO_2-like cubic phase, instead of a continuous lattice constant contraction in a single phase.

To improve the calendar life of Li-ion cells, cell testing has been conducted to understand aging phenomena and mechanisms. For example, electrochemical testing of different cell designs with different shapes and cathode materials showed that extra lithium (or lithium reserve) for nickel-based oxides as cathode materials enhances the calendar life of batteries [20].

Abuse tolerance of Li-ion batteries is a major concern limiting their applications. Abuse can be categorized as physical abuse (crush and nail penetration), electrical abuse (short circuit and overcharge), and thermal abuse (overheating). Thermal abuse can occur during relatively normal operating conditions when excessive heat generated is not

efficiently dissipated. This condition can eventually cause catastrophic failure of batteries along with ignition of battery active materials, so called thermal runaway. Many cell testing studies have been conducted to understand battery abuse tolerance. For example, an experimental study with cycling of high power 18650 cells was carried out to study the contribution of individual cell components to overall cell thermal abuse tolerance [21]. It was found that microcarbon mesobeads increase thermal stability of cells due to more effective solid electrolyte interface formation.

2.3. Selected Research on Cell Modeling, Simulations and Optimization

Li-ion cell models have been developed for computer simulations and battery design optimization. For example, a pseudo 2D model was used to numerically study the effect of cathode thickness and electrode porosity on energy and power output of Li-ion cells [22]. A coupled electrochemical and thermal model was developed to study heat transfer and thermal management of lithium polymer batteries [23]. In this study, electrochemical and thermal behavior of batteries was studied under different discharge temperatures. Current and active material particle size and several thermal management systems approaches were discussed to prevent overheating of batteries.

This study will focus on (1) improving calendar life by reducing performance degradation due to stress induced electrode particle fracture and heat generation through modeling and numerical simulations, and (2) creating models including electrode materials microstructural information for computer simulations that can lead to optimizing battery design for improved energy output per unit volume and mass.

3. STRESS AND HEAT GENERATION INSIDE ELECTRODE PARTICLES

To improve the calendar life of Li-ion batteries, capacity degradation during battery cycling has to be understood and minimized. One of the capacity degradation mechanisms is fracture of electrode particles due to intercalation-induced stress. Fracture has been experimentally [24][25][26] observed in cathode particles of lithium-ion batteries after a relatively small number of cycles as shown in Figure 1.3. When Li ions are intercalated into the lattice of active material in electrodes, the lattice is expanded accordingly. This lattice expansion causes strain inside the material. Non-uniform strain results in stress, the so-called intercalation-induced stress. As Li ions are inserted and extracted during cycling of batteries, the intercalation compound undergoes cyclic load of intercalation-induced stress. This eventually causes electrode particle fracture after a certain number of discharge/charge cycles. Particle-scale fracture of active materials results in battery performance degradation due to the loss of electrical contact and subsequent increase in the surface area subjected to side reactions [27].

To predict the intercalation-induced stress in electrode materials, a model is needed. A one-dimensional model was developed to estimate stress generation within spherical electrode particles [28]. However, this model does not predict three dimensional stresses inside three dimensional electrode particles. Therefore, a three dimensional model based on the thermal stress analogy, following the treatment of diffusion-induced stress by analogy to thermal stresses first proposed by Prussin [29], will be proposed in this study to simulate the intercalation-induced stresses inside ellipsoidal particles.

Heat generation inside batteries is a major safety concern because excessive heat generation in Li batteries, resulting in thermal runaway, results in complete cell failure

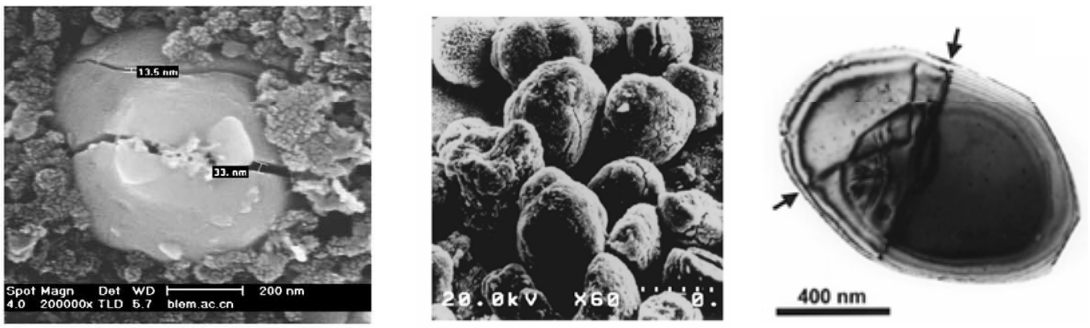

(a) (b) (c)

Figure 1.3: Experimental observation of fracture in cathode particles: (a) $LiFePO_4$ particle after 60 cycles [24]; (b) gold-codeposited $LiMn_2O_4$ electrode particles after cyclic voltammetric tests at a scan rate of 4mV/s [25]; (c)$LiCoO_2$ particles after 50 cycles [26].

accompanied by violent venting and rupture, along with ignition of battery active materials. Heat generation inside batteries comes from irreversible resistive heating, reversible entropic heat, heat change of chemical side reactions, and heat of mixing due to the generation and relaxation of concentration gradients [30].

To date, there has been no study in the literature on how to design electrode particles to reduce both stress and heat generation. In this study, a surrogate-based approach is used to systematically study the effect of both particle shape and cycling parameter on stress and heat generation inside single ellipsoidal cathode particles under potentiodynamic control and to provide design guidelines for reducing stress and heat generation. Experiments [31] and simulations [32] have been conducted using a single particle electrode to study the kinetic and transport properties of Li ion intercalation and deintercalation. The single particle electrode model is extended in this study to include stress and heat generation analysis.

4. MULTISCALE MODELING OF LI-ION BATTERIES

Li-ion battery models in the existing literature with different fidelity include equivalent-circuit-based models, physics-based pseudo 2D models, and a mesoscale 3D model. Equivalent-circuit-based models, which originated from conventional electrochemical impedance spectroscopy (EIS) battery characterization techniques, use an equivalent electric circuit composed of resistors and capacitors to simulate cell performance and behavior [33, 34, 35]. Pseudo 2D models were first developed from porous electrode theory [36] by solving continuum scale governing equations for all the physicochemical processes over homogeneous media along the thickness direction of a cell [37]. The required effective material properties are commonly modeled by the

classical Bruggeman's equation. The volumetric reaction rate is calculated using a simplified separated spherical electrode particle by introducing a pseudo dimension. A mesoscale modeling approach was proposed to implement the 3D detailed modeling of electrode materials consisting of regularly and randomly arranged cathode particles [38]. However, the number of electrode particles included in the model was limited due to the excessive computation power requirement.

Scales inside a Li-ion cell span from microns for electrode particles to millimeters for cell thickness. To successfully include electrode microstructure information in a battery scale model, a multiscale framework is needed. The main objective of multiscale modeling is to capture the physics to a certain desired accuracy in an efficient way. Microscopic models (for electrode microstructure) are accurate but computationally expensive, while macroscopic models (for a Li-ion cell) are simplified and efficient. The combinational use of models on these two scales will help to achieve accuracy and efficiency at the same time.

Microscopic and macroscopic models could be fundamentally different in terms of the physics principles applied. For example, one could apply molecular dynamics to the microscopic scale and continuum fluid dynamics to the macroscopic scale. Sometimes, one basic physics principle is applicable for all scales and the scale disparity is caused by geometric complexity, which is the case for the processes in porous battery electrode materials. For multiscale modeling of the processes in porous media, there are two approaches to derive the macroscopic governing equations from their counterparts on the microscopic scale, volume averaging [39] and homogenization [40][41].

4.1. Homogenization Approach

The homogenization approach is an upscaling procedure that lets the microscopic scale approach zero asymptotically. A systematic way of performing this approach is to do asymptotic expansion of variables.

To illustrate the basic idea of homogenization, the following diffusion equation is used.

$$\begin{cases} \nabla \cdot \left[D^{\varepsilon}\left(\mathbf{x}\right) \nabla c^{\varepsilon}\left(\mathbf{x}\right) \right] + f\left(\mathbf{x}\right) = 0, & \mathbf{x} \in \Omega \subset \mathbf{R}^3 \\ c\left(\mathbf{x}\right) = c_D\left(\mathbf{x}\right), & \mathbf{x} \in \partial\Omega \end{cases} . \tag{1}$$

It is assumed that the diffusion coefficient D^{ε} is rapidly oscillating, and it is of the form $D^{\varepsilon} = D\left(x/\varepsilon\right)$, where function D is periodic (with periodicity smaller than unity) and ε a scale parameter ($\varepsilon << 1$). With this assumption, the diffusion coefficient of porous media changes periodically from pores and solid matrix. Define a new variable $\mathbf{y} = \mathbf{x}/\varepsilon$. $\mathbf{y}$ is the coordinate for the microscale, and it is commonly called fast variable ($\mathbf{x}$ is often referred as slow variable). All variables should depends on the coordinates ($\mathbf{x}$ and $\mathbf{y}$) for both scales. Therefore, we can do the asymptotic expansion with respect to ε

$$c^{\varepsilon}\left(\mathbf{x}\right) = c_0\left(\mathbf{x},\mathbf{y}\right) + \varepsilon c_1\left(\mathbf{x},\mathbf{y}\right) + \varepsilon^2 c_2\left(\mathbf{x},\mathbf{y}\right) + \cdots . \tag{2}$$

Submit the expansion into Equation (1) and rearrange the terms according to the order for ε, one finally obtains a homogenized equation based on the terms of the order ε^0

$$\begin{cases} \nabla \cdot \left[\mathbf{D}^0 \nabla c\left(\mathbf{x}\right) \right] + f\left(\mathbf{x}\right) = 0, & \mathbf{x} \in \Omega \subset \mathbf{R}^3 \\ c\left(\mathbf{x}\right) = c_D\left(\mathbf{x}\right), & \mathbf{x} \in \partial\Omega \end{cases} . \tag{3}$$

This is the equation for the macroscopic scale. Tensor $\mathbf{D}^0$ is obtained by solving a cell problem on the microscopic scale

$$D_{ij}^0 = \int_Y D(y)\left(\delta_{ij} + \partial_{y_i} w_j(y)\right)\mathrm{d}y\,, \tag{4}$$

where Y is the volume of periodicity cell and $w_j(y)$ is the solution of cell problem

$$\nabla_y \cdot \left(D(y)\nabla_y w_j(y)\right) = -\nabla_y \cdot \left(D(y)\mathbf{e}_j\right). \tag{5}$$

The process results in a set of equations for both macroscopic and microscopic scales. Homogenization approach is more complicated to implement than the volume averaging technique, but the obtained equations on micro and macroscopic scales constitute a closed system. The homogenization approach fits more into the methodology of multiscale modeling since the equations on each scale are already available, and two-way coupling can be achieved relatively easily. Homogenization approach has been used for stress analysis in porous media and composites. For example, Matous et al. [42] used this methodology to analyze damage evolution, under different loads, in a model 2D composite system composed of particles and binder. Ghosh et al. [43] applied homogenization technique to develop a multi-level model for stress analysis of an elastic fibrous composite. Homogenization has also been used to model transport phenomena in porous media (for example [44][45]).

4.2. Volume Averaging

In the volume averaging technique, the variable of interest is first averaged over a representative elementary volume (REV).

$$\overline{c_s} = \frac{1}{\mathrm{d}V}\int_{\mathrm{d}V} c_s \gamma_s \mathrm{d}V\,, \tag{6}$$

where $\mathrm{d}V$ is the volume of REV, $\gamma_s = 1$ in phase s and 0 elsewhere. The governing equations on the microscopic scale are then averaged over REV. For example, when a transient diffusion equation is averaged on both sides,

$$\frac{1}{\mathrm{d}V}\int_{\mathrm{d}V}\left(\frac{\partial c_s}{\partial t}\right)\gamma_s \mathrm{d}V = \frac{1}{\mathrm{d}V}\int_{\mathrm{d}V}\nabla\cdot\left(D_s\nabla c_s\right)\gamma_s \mathrm{d}V\,. \tag{7}$$

In the differential equations, the volumetric average of the temporal and spatial derivatives is transformed into the temporal and spatial derivatives of the averaged quantities by using the two theorems dealing with the averages of derivatives,

$$\frac{1}{\mathrm{d}V}\int_{\mathrm{d}V}\left(\frac{\partial c_s}{\partial t}\right)\gamma_s \mathrm{d}V = \frac{\partial \overline{c_s}}{\partial t} - \frac{1}{\mathrm{d}V}\int_{A_s} c_s \mathbf{v}\cdot\mathbf{n}\mathrm{d}A\,, \tag{8}$$

$$\frac{1}{\mathrm{d}V}\int_{\mathrm{d}V}\nabla\cdot\left(D_s\nabla c_s\right)\gamma_s \mathrm{d}V = \nabla\cdot\left(\overline{D_s\nabla c_s}\right) + \frac{1}{\mathrm{d}V}\int_{A_s}\left(D_s\nabla c_s\right)\cdot\mathbf{n}\mathrm{d}A\,. \tag{9}$$

There are additional closure terms $\nabla\cdot\left(\overline{D_s\nabla c_s}\right)$ and $J = 1/\mathrm{d}V\int_{A_s}\left(D_s\nabla c_s\right)\cdot\mathbf{n}\mathrm{d}A$ that require further modeling, appearing as the consequence of the averaging process. It is easier to obtain the macroscopic governing equations using the volume averaging technique than the homogenization approach. However, the resulting closure terms require further modeling to close the system. Also, this technique does not pass the information from macro to micro scale, but the resolution on the microscopic scale is sometimes desirable. This approach has been widely used to model the fluid flow and heat transfer in porous media (for example [46, 47]). It has also been used to analyze the mechanics inside porous media [48].

Volume averaging-like techniques have been applied for battery modeling to deal with the porous feature of electrode materials [22, 49, 50, 51]. However, closure terms for effective material properties and volumetric reaction rate have only been treated

analytically using oversimplified assumptions instead of detailed numerical modeling of microstructural architecture. In this study, volume averaging technique is used and the closure terms are proposed to be calculated directly from 3D microscopic simulations instead of simplified analytical modeling.

4.3. Scale Bridging

In the scale bridging concept from [52, 53], a REV on the microscopic scale is assigned to each integration point of the macro-mesh. Appropriate boundary conditions, derived from information available from the macroscopic scale, are imposed on REV on the microscopic scale. A separate computation is then conducted for the REV, and the obtained variable values are averaged over REV to provide macroscopic closure terms with which the governing equations on macroscopic scale are solved. This provides an approach to determine the macroscopic response of heterogeneous materials with accurate accounting of microstructural characteristics.

There are two categories of approaches to couple microscopic and macroscopic scales, concurrent coupling and serial coupling [54] as summarized in Figure 1.4. In the concurrent coupling approach, microscopic and macroscopic simulations are conducted concurrently with simultaneous information exchange. In serial coupling, an effective macroscopic model is determined from the microscopic model in a pre-processing step. Concurrent coupling is computationally expensive. Therefore, in this study we prefer to adopt the serial coupling approach. To systematically arrange the simulations on microscopic scale and couple the two scales efficiently, the database approach [55] and look up table approach [56] have been used to map the microscopic information and macroscopic closure terms. In this study we propose a surrogate-based approach to bridge

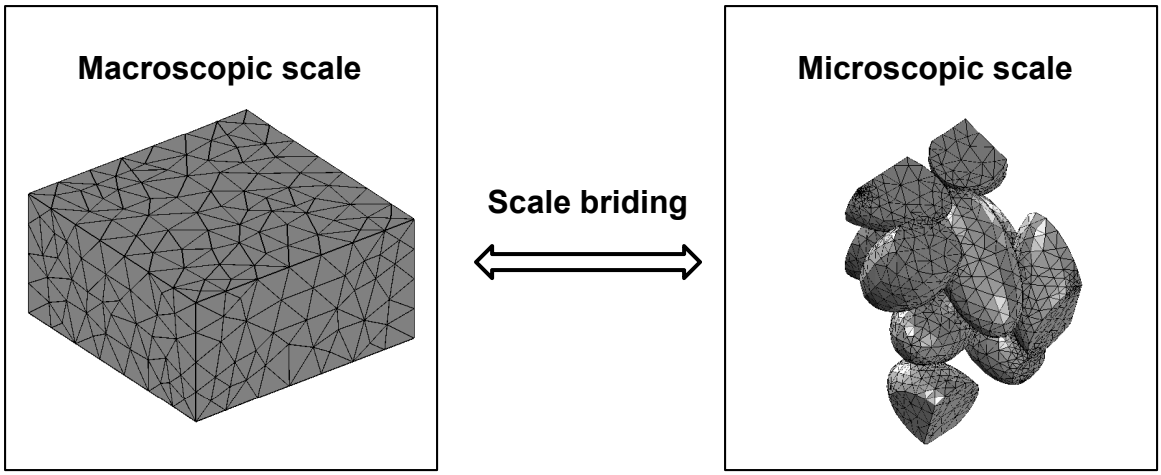

- Concurrent coupling

simultaneous, two-way information exchange; expensive

- Serial coupling

microscopic modeling in the pre-processing step; efficient; one-way coupling

- database approach [55]
- look up table approach [56]
- surrogate based approach (this study)

Figure 1.4: Summary of scale bridging approaches.

the scales serially. Surrogate-based approaches have been used for design optimization and analysis [57]. Surrogate models are constructed using numerical results obtained from simulations on carefully sampled points; they are capable of predicting the objective functions efficiently over the whole design space once these models are validated for sufficient accuracy. In applying a surrogate-based approach for scale bridging in battery modeling, the input variables for the surrogate models are the microscopic structure information and the microscopic scale simulation boundary conditions from nodes values on macroscopic scale mesh, and the output variables are those closure terms calculated from microscopic scale simulations.

5. SURROGATE-BASED MODELING AND ANALYSIS

The surrogate-based approach is used in two occasions in this study: (1) to systematically analyze the effect of particle shape and cycling rate on stress and heat generation, and (2) to efficiently bridge microscopic and macroscopic scale simulations in the multiscale modeling framework.

Surrogate models, which are constructed using the available data generated from pre-selected designs, offer an effective way of evaluating geometrical and physical variables. For expensive computer simulations and experiments, surrogate models offer a low cost alternative to evaluate designs because surrogate models are constructed using the limited data generated using carefully selected designs. Moreover, surrogate models provide a global view of the objective functions' response to the design variables. Surrogate-based approach has been widely used in analysis and design optimization, for example, model parameter calibration for cryogenic cavitation modeling [58], axial compressor blade shape optimization [59], hydraulic turbine diffuser shape optimization

[60], dielectric barrier discharge plasma actuator performance characterization [61], and flapping wing aerodynamic analysis [62]. The key steps of surrogate modeling, as illustrated in Figure 1.5 (a), include design of experiments, running numerical simulations or conducting experimental measurements, constructing surrogate models, validating and further refining the models if necessary [57, 63, 64].

Commonly used design of experiments approaches include face centered central-composite design (FCCD) [65], Latin hypercube sampling (LHS) [66], and orthogonal arrays [67]. FCCD includes designs on 2^{N_v} vertices, $2N_v$ axial points (where N_v is the dimension of the design space) and N_c repetitions of the central point. Rrepetitions at the center reduce the variance and improve stability. An illustration for FCCD in three dimensional design space is shown in Figure 1.5 (b). FCCD is not practical for higher dimensional spaces ($N_v > 8$) because the number of simulations or experiments needed becomes very high. LHS is a stratified sampling approach with the restriction that each of the input variables has all portions of its distribution represented by input values. A sample of size N_s can be constructed by dividing the range of each input variable into N_s strata of equal marginal probability $1/N_s$ and sampling once from each stratum. Figure 1.5 (c) shows an example of LHS design for N_s=6 points in a two dimensional design space.

The obtained simulations or experiment results on the sampling points are used to construct surrogate models; sampling points from the design of experiments for surrogate model construction are sometimes also referred to as training points. Commonly used surrogate models include polynomial response surface (PRS), kriging [68], radial basis neural network (RBNN). Polynomial response surface represent the objective function as

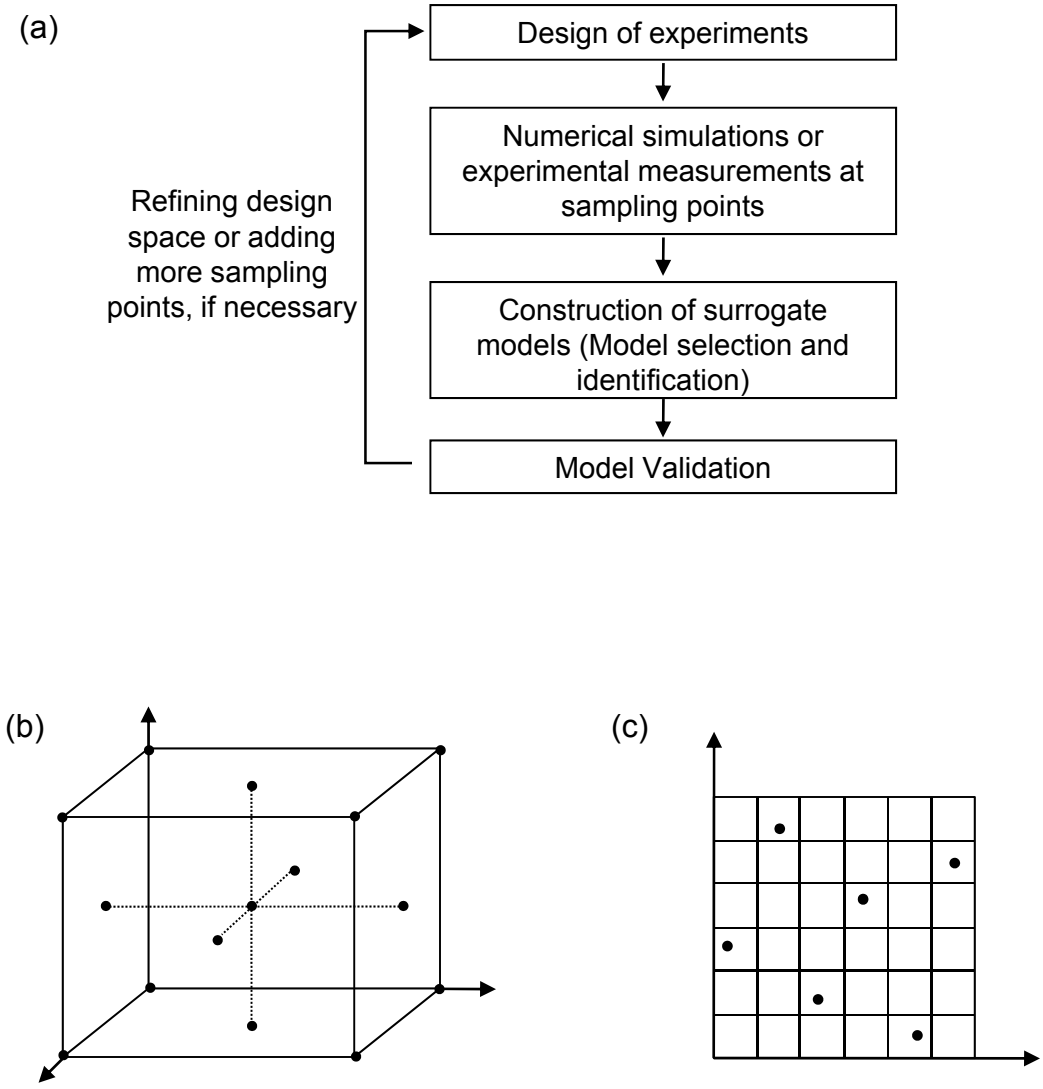

Figure 1.5: Surrogate modeling: (a) key steps of surrogate modeling; (b) design of experiments by FCCD; (c) design of experiments by LHS.

a linear combination of monomial basis functions. An example for the second order polynomial response surface approximation is

$$\hat{f}(\mathbf{x}) = \beta_0 + \sum_{i=1}^{N_v} \beta_i x_i + \sum_{i=1}^{N_v} \sum_{j \le i} \beta_{ij} x_i x_j \ , \tag{10}$$

where the coefficients β are determined by minimizing the approximation error in a least square sense. The kriging model estimates the value of a function (response) at some unsampled location as the sum of two components: the linear model (e.g. polynomial trend) $\sum_{i=1}^{p} \beta_i f_i(\mathbf{x})$ and a systematic departure $Z(\mathbf{x})$ representing low (large scale) and high frequency (small scale) variation components, respectively. The systematic departure components are assumed to be correlated as a function of distance between the locations under consideration. Gaussian function is commonly used for the correlation,

$$C\left(Z(\mathbf{x}), Z(\mathbf{s}), \boldsymbol{\theta}\right) = \prod_{i=1}^{N_v} \exp\left(-\theta_i (x_i - s_i)^2\right). \tag{11}$$

Optimal parameters θ_i are determined for maximum likelihood estimation. The RBNN model uses linear weighted combinations of radially symmetric functions $a_i(\mathbf{x})$ based on Euclidean distance or other such metrics to approximate response functions. A typical radial function is the Gaussian function,

$$a(\mathbf{x}) = \text{radbas}\left(\|\mathbf{s} - \mathbf{x}\| b\right), \ \text{where} \ \ \text{radbas}(n) = e^{-n^2} \ . \tag{12}$$

Parameter *b* in the above equation is inversely related to a user-defined parameter 'spread constant' that controls the response of the radial basis function. Typically, spread constant is selected between zero and one. A very high spread constant would result in a highly non-linear response function. An example of surrogate models (PRS, kriging and

RBNN) constructed based on training data of 5 sampling points obtained from the analytical functions $y=\exp(x^4)$ is shown in Figure 1.6.

After surrogate models are constructed, their accuracy is evaluated using error measures. Error in approximation of surrogate models at any given point **x** is defined as the difference between the actual function $y(\mathbf{x})$ and the predicted response $\hat{y}(\mathbf{x})$. However, the actual response in the design space is unknown. We can not compute the actual errors of surrogate model prediction. Therefore, error measures are practically obtained on the available training data used for surrogate model construction or additional testing data obtained from numerical simulations or experimental measurements. Commonly used error measures based on the available training data include the adjusted coefficient of multiple determination R^2_{adj} for polynomial response surface and prediction error sum of squares (PRESS) [69]. The coefficient of multiple determination is defined as

$$R^2 = 1 - \frac{SS_E}{SS_T}, \tag{13}$$

where $SS_E = \sum_{i=1}^{N_s} \left(y_i - \hat{y}_i\right)^2$ is the sum of square of residuals and $SS_T = \sum_{i=1}^{N_s} \left(y_i - \bar{y}\right)^2$ is the total sum of squares ($\bar{y} = \frac{1}{N_s} \sum_{i=1}^{N_s} y_i$). This coefficient can be interpreted as the proportion of response variation explained by the surrogate model (PRS). $R^2 = 1$ indicates that the fitted model explains all variability in y. However, this coefficient increases weakly with the number of terms used in PRS. Therefore, it is important to take into account the number of terms used in the regression mode, which results in the definition for the adjusted coefficient of multiple determination R^2_{adj} . R^2_{adj} is defined as

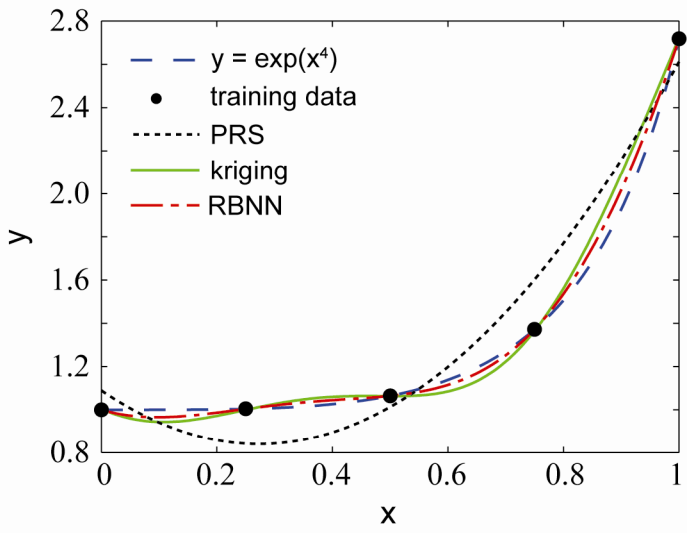

Figure 1.6: An example of varies surrogate models constructed based on training data obtained from the analytical function y=exp(x^4).

$$R^2_{\text{adj}} = 1 - \frac{SS_E/(N_s - p)}{SS_T/(N_s - 1)} = 1 - \frac{(N_s - 1)}{(N_s - p)}\left(1 - R^2\right), \tag{14}$$

where p is the number of terms used in polynomial response surface model. The adjusted coefficient increases only if the newly added term improves the model. For a good fit, this coefficient should be close to one. PRESS is a cross-validation error. It is the summation of squares of all PRESS residues, each of which is calculated as the difference between the simulation by computer experiments and the prediction by surrogate models constructed from the remaining sampling points while excluding the point of interest [69]. PRESS RMS (root mean square) is the root mean square of the PRESS residues,

$$\text{PRESS RMS} = \sqrt{\frac{1}{N_s}\sum_{i=1}^{N_s}(y_i - \hat{y}_i^{(-i)})^2}\,, \tag{15}$$

where N_s is the number of training points, y_i is the value of the objective function obtained from numerical simulations or experimental measurements at training point i, and $\hat{y}_i^{(-i)}$ is the prediction by the surrogate model constructed by leaving point i out and using the remaining N_s-1 training points. This strategy is also called leave-one-out. The smaller the PRESS RMS, the more accurate the surrogate model will be. PRESS RMS is expensive to calculate using leave-one-out strategy for larger number of training points since N_s different surrogate models need to be constructed based N_s different sets of training data containing N_s-1 points. To solve this problem, a k-fold strategy was used to approximate PRESS RMS [70, 71]. In this approach, the available data (p points) are first divided into p/k clusters. Each fold is constructed using a point randomly selected from

each of the clusters. Out of the k folds, a single fold is retained as the validation data for testing the model, and the remaining k-1 folds are used as training data. k-fold turns out to be the leave-one-out when $k=p$. This k-fold strategy provides a much faster approach for calculating PRESS. Surrogate models are also evaluated by comparing surrogate model prediction and actual numerical simulation or experimental measurement results on testing points. The actual root mean square error could be approximated by using the prediction error on testing points as

$$\text{RMSE} = \sqrt{\frac{1}{N_{\text{test}}} \sum_{i=1}^{N_{\text{test}}} (y_i - \hat{y}_i)^2} \,, \tag{16}$$

where y_i is the actual data from numerical simulation or experimental measurements at testing points i, and $\hat{y}_i$ is the prediction by surrogate models at testing points i. With the calculated error measures for surrogate models constructed, one can try to select the best surrogate model based on a given error measure as the criterion. However, since the actual response of the objective function is unknown, one does not really know which error measure criterion performs the best. Sometimes, it can be risky to use individual surrogate models for predicting objective functions. Weighted average surrogates or ensemble of surrogates was proposed to provide more robust prediction of objective functions than individual surrogates [72]. Surrogate models validated to have adequate accuracy can be used for further analysis such as global sensitivity analysis and optimization of objective functions. If the desired accuracy is not achieved, another iteration of the surrogate modeling process should be repeated with refined design space or additional sampling points in the same design space.

With the constructed surrogate models, global sensitivity analysis can be conducted to study the importance of design variables. Global sensitivity analysis quantifies the variation of the objective functions caused by design variables. The importance of design variables is presented by main factor and total effect indices [57]. Main factor is the fraction of the total variance of the objective function contributed by a particular variable in isolation, while the total effect includes contribution of all partial variances in which the variable of interest is involved. When Sobol's method [73] is commonly used to calculate global sensitivity indices, a surrogate model $f(\mathbf{x})$ of a square integrable objective as a function of a vector of independent input variables $\mathbf{x}$ in domain [0, 1] is decomposed as the sum of functions of increasing dimensionality as

$$f(\mathbf{x}) = f_0 + \sum_i f_i(x_i) + \sum_{i<j} f_{ij}(x_i, x_j) + \cdots + f_{12\ldots N}(x_1, x_2, \ldots, x_N). \tag{17}$$

In the context of global sensitivity analysis, the total variance denoted as $V(f)$ can be shown to be equal to

$$V(f) = \sum_{i=1}^{N_v} V_i + \sum_{1 \le i, j \le N_v} V_{ij} + \ldots + V_{1\ldots N_v}. \tag{18}$$

Each of the terms V_i, V_{ij}, V_{ijk} $\cdots$ represents the partial contribution or partial variance of the independent variables or set of variables to the total variance and provides an indication of their relative importance. The main factor index of variable x_i is defined as

$$S_i^{\text{main}} = \frac{V_i}{V(f)}. \tag{19}$$

The total effect index of variable x_i is defined as

$$S_i^{\text{total}} = \frac{V_i + \sum_{j,j\neq i} V_{ij} + \sum_{j,j\neq i}\sum_{k,k\neq i} V_{ijk} + \ldots}{V(f)}. \quad (20)$$

Constructed surrogate models can also be used for objective function optimization. With the objective function globally mapped over the design space by surrogate models, global minima or maxima of the objective function can be identified for the single objective optimization. For two-objective optimization, a pareto front can be generated using surrogate models constructed to identify the trade-offs between two objective functions.

6. SCOPE AND OUTLINE OF THE DISSERTATION

In Chapter 2, an intercalation-induced stress model with the analogy to thermal stress modeling is developed to determine localized intercalation-induced stress in electrode particles. Intercalation-induced stress is calculated within ellipsoidal electrode particles with a constant diffusion flux assumed at the particle surface. In Chapter 3, surrogate-based analysis is conducted to systematically investigate the effect of both particle shape and cycling parameter on stress and heat generation inside single ellipsoidal cathode particles under potentiodynamic control. The diffusion flux on the particles is determined by the rate of electrochemical reactions modeled by the Butler-Volmer equation. The outcome from this surrogate-based analysis provides guidelines for electrode particle design that will reduce stress and heat generation during battery cycling. Chapters 2 and 3 facilitate the understanding of physicochemical mechanisms by choosing a simple geometry, single electrode particles, without dealing with geometric complexity. Chapter 4 develops a battery scale model that takes into account the complicated 3D microstructure information of battery electrode materials. A multiscale

modeling framework is proposed to deal with the disparate length scales present in Li-ion cells. Closure terms from macroscopic scale governing equations are extracted from microscopic scale modeling of electrode particle clusters. Scale bridging is achieved by serial coupling using a surrogate-based approach.

BIBLIOGRAPHY

1. U.S. Environmental Protection Agency, Greenhouse Gas Emissions from the U.S. Transportation Sector, 1990-2003, www.epa.gov/otaq/climate.htm, accessed June 6, 2006.

2. C. Samaras, and K. Meisterling, Life Cycle Assessment of Greenhouse Gas Emissions from Plug-in Hybrid Vehicles: Implications for Policy, Environmental Science & Technology, 42, 3170–3176 (2008).

3. D. Linden and T. B. Reddy (editors), Handbook of Batteries (third edition), McGraw-Hill, 2002.

4. Official web page of the United States Advanced Battery Consortium (USABC), http://www.uscar.org/guest/view_team.php?teams_id=12, accessed June 6, 2009.

5. H. Li, X. Huang, L. Chen, Z. Wu, and Y. Liang, A High Capacity Nano-Si Composite Anode Material for Lithium Rechargeable Batteries, Electrochemical and Solid-State Letters, 2(11), 547-549 (1999).

6. C. K. Chan, H. Peng, G. Liu, K. MclLwrath, X. F. Zhang, R. A. Huggins and Y. Cui, High-Performance Lithium Battery Anodes Using Silicon Nanowires, Nature Nanotechnology, 3(1), 31-35 (2008).

7. T. Ohzuku, A. Ueda, and N. Yamamoto, Zero-Strain Insertion Material of Li[Li1/3Ti5/3]O4 for Rechargeable Lithium Cells, Journal of the Electrochemical Society, 142(5), 1431-1435 (1995).

8. R. J. Gummow, A. de Kock, and M. M. Thackeray, Improved Capacity Retention in Rechargeable 4V Lithium/Lithium Manganese Oxide (Spinel) Cells, Solid State ionics, 69, 59-67 (1994).

9. A. K. Padhi, K. S. Nanjundaswamy, and J. B. Goodenough, Phospho-olivines as Positive-Electrode Materials for Rechargeable Lithium Batteries, Journal of the Electrochemical Society, 144(4), 1188-1194 (1997).

10. T. Ohzuku and Y. Makimura, Layered Lithium Insertion Material of LiCo1/3Ni1/3Mn1/3O2 for Lithium-Ion Batteries, Chemistry Letters, 7, 642-643 (2001).

11. N. Ravet, Y. Chouinard, J. F. Magnan, S. Besner, M. Gauthier, and M. Armand, Electroactivity of Natural and Synthetic Triphylite, Journal of Power Sources, 97-98, 503-507 (2001).

12. H. Joachin, T. D. Kaun, K. Zaghib, and J. Prakash, Electrochemical and Thermal Studies of Carbon-Coated LiFePO4 Cathode, Journal of The Electrochemical Society, 156 (6), A401-A406 (2009).

13. S.-Y. Chung, J. T. Bloking and Y.-M. Chiang, Electronically Conductive Phospho-Olivines as Lithium Storage Electrodes, Nature Materials, 1, 123-128 (2002).

14. P. B. Balbuena and Y. Wang (editors), Lithium-Ion Batteries; Solid-Electrolyte Interphase, Imperial College Press, London, 2004.

15. R. Spotnitz and J. Franklin, Abuse Behavior of High-Power, Lithium-Ion Cells, Journal of Power SOurnces, 113, 81-100 (2003).

16. S. Leroy, F. Blanchard, R. Dedryvere, H. Martinez, B. Carre, D. Lemordant, and D. Gonbeau, Surface Film Formation on a Grahite Electrode in Li-Ion Batteries: AFM and XPS Study, Surface and Interface Analysis, 37, 773-781 (2005).

17. M. Itagaki, N. Kobari, S. Yotsuda, K. Watanabe, S. Kinoshita, and M. Ue, In Situ Electrochemical Impedance Spectroscopy to Investigate Negative Electrode of Lithium-Ion Rechargeable Batteries, Journal of Power Sources, 135, 255-261 (2004).

18. J. Li and J. R. Dahn, An In Situ X-Ray Diffraction Study of the Reaction of Li with Crystalline Si, Journal of The Electrochemical Society, 154(3), A156-A161 (2007).

19. X. Q. Yang, X. Sun, S. J. Lee, J. McBreen, S. Mukerjee, M. L. Daroux, and X. K. King, In Situ Synchrontron X-Ray Diffraction Studies of the Phase Transitions in LixMn2O4 Cathode Materials, Electrochemical and Solid-State Letters, 2(4), 157-160 (1999).

20. M. Broussely, S. Herreyre, P. Biensan, P. Kasztejna, K. Nechev, and R. J. Staniewicz, Aging Mechanism in Li Ion Cells and Calendar Life Predictions, Journal of Power Sources 97-98, 13-21 (2001).

21. E. P. Roth and D. H. Doughty, Thermal Abuse Performance of High-Power 18650 Li-Ion Cells, Journal of Power Sources 128, 308-318 (2004).

22. T. F. Fuller, M. Doyle, and J. Newman, Simulation and Optimization of the Dual Lithium Ion Insertion Cell, Journal of the Electrochemical Society, 141(1), 1-10 (1994).

23. L. Song and J. W. Evans, Electrochemical-Thermal Modeling of Lithium Polymer Batteries, Journal of The Electrochemical Society, 147(6), 2086-2095 (2000).

24. D. Wang, X. Wu, Z. Wang, and L. Chen, Cracking Causing Cyclic Instabilit of LiFePO4 Cathode Material, Journal of Power Sources, 140, 125-128 (2005).

25. M.-R. Lim, W.-I. Cho, and K.-B. Kim, Preparation and Characterization of Gold-Codeposited LiMn2O4 Electrodes, Journal of Power Sources 92, 168-176 (2001).

26. H. Wang, Y.-I. Jang, B. Huang, D. R. Sadoway, and Y.-M. Chiang, TEM Study of Electrochemical Cycling-Induced Damage and Disorder in LiCoO2 Cathodes for Rechargeable Lithium Batteries, Journal of the Electrochemical Society, 146(2), 473-480 (1999).

27. K. E. Aifantis and J. P. Dempsey, Stable crack growth in nanostructured Li-batteries, Journal of Power Sources, 143, 203–211 (2005).

28. J. Christensen and J. Newman, Stress Generation and Fracture in Lithium Insertion Materials, Journal of Solid State Electrochemistry, 10, 293–319 (2006).

29. S. Prussin, Generation and Distribution of Dislocations by Solute Diffusion, *Journal of Applied Physics*, 32(10), 1876-1881 (1961).

30. K. E. Thomas, and J. Newman, Thermal Modeling of Porous Insertion Electrodes, Journal of the Electrochemical Society, 150, A176-A192 (2003).

31. I. Uchida, H. Fujiyoshi, and S. Waki, Microvoltammetric Studies on Single Particles of Battery Active Materials, Journal of Power Sources, 68, 139-144 (1997).

32. D. Zhang, B. N. Popov, and R. E. White, Modeling Lithium Intercalation of a Single Spinel Particle under Potentiodynamic Control, Journal of The Electrochemical Society, 147, 831-838 (2000).

33. M. W. Verbrugge and R. S. Conell, Electrochemical and Thermal Characterization of Battery Modules Commensurate with Electric Vehicle Integration, Journal of The Electrochemical Society, 149, A45-A53 (2002).

34. B. Y. Liaw, G. Nagasubramanian, R. G. Jungst, and D. H. Doughty, Modeling of Lithium Ion Cells – A Simple Equivalent-Circuit Model Approach, Solid State Ionics, 175, 835-839 (2004).

35. P. L. Moss, G. Au, E. J. Plichta, and J. P. Zheng, An Electrical Circuit for Modeling the Dynamic Response of Li-Ion Polymer Batteries, Journal of The Electrochemical Society, 155, A986-A994 (2008).

36. J. Newman and W. Tiedemann, Porous-Electrode Theory with Battery Applications, AIChE Journal, 21, 25-41 (1975).

37. M. Doyle, T. F. Fuller, and J. Newman, Modeling of Galvanostatic Charge and Discharge of the Lithium Polymer Insertion Cell, Journal of The Electrochemical Society, 140, 1526-1533 (1993) .

38. C.-W. Wang and A. M. Sastry, Mesoscale Modeling of a Li-Ion Polymer Cell, Journal of The Electrochemical Society, 154, A1035-A1047 (2007).

39. W. Shyy et al., Computational Technques for Complex Transport Phenomena, Cambridge, 1997.

40. U. Hornung (editor), Homogenization and Porous Media, Springer, New York, 1997.

41. E. Sanchez-Palencia, Non-Homogeneous Media and Vibration Theory, edited by J. Ehlers et al, Lecture Notes in Physics, Springer-Verlag, New York, 1980.

42. K. Matous, H. M. Inglis, X. Gu, D. Rypl, T. L. Jackson, and P. H. Geubelle, Multiscale Modeling of Solid Propellants: from Particle Packing to Failure, Composites Science and Technology, 67, 1694-1708 (2007).

43. S. Ghosh, K. Lee and P. Raghavan, A Multi-level Computational Model for Multi-scale Damage Analysis in Composite and Porous Materials, International Journal of Solids and Structures 38, 2335-2385 (2001).

44. C. C. Mei, Method of Homogenization Applied to Dispersion in Porous Media, Transport in Porous Media 9: 261-274 (1992).

45. I. Lunati, S. Attinger, and W. Kinzelbach, Macrodispersivity for Transport in Arbitrary Nonuniform Flow Fields: Asymptotic and Preasymptotic Results, Water Resources Research 38 (10): Art. No. 1187 OCT 2002.

46. A. R. Martin, C. Saltiel, W. Shyy, Heat Transfer Enhancement with Porous Inserts in Recirculating Flows, Journal of Heat Transfer, 120, 458-467 (1998).

47. E. Sozer and W. Shyy, Multi-scale Thermo-fluid Transport in Porous Media, International Journal of Numerical Methods for Heat & Fluid Flow, 18(7/8) 883-899 (2008).

48. J. G. Berryman and S. R. Pride, Volume Averaging, Effective Stress Rules, and Inversion for Microstructural Response of Multicomponent Porous Media, Int. J. Solids Structures, 35, 4811-4843 (1998).

49. M. Doyle, T. F. Fuller, and J. Newman, Modeling of Galvanostatic Charge and Discharge of the Lithium Polymer Insertion Cell, Journal of The Electrochemical Society, 140, 1526-1533 (1993) .

50. P. D. Vidts and R. E. White, Governing Equations for Transport in Porous Electrodes, Journal of The Electrochemical Society, 144, 1343-1353 (1997).

51. W. B. Gu, C. Y. Wang, and B. Y. Liaw, Micro-Macroscopic Coupled Modeling of Batteries and Fuel Cells, Journal of the Electrochemical Society, 145, 3407-3418 (1998).

52. R. J. M. Smit, W. A. M. Brekelmans, and H. E. H. Meijer, Prediction of the Mechanical Behavior of Nonlinear Heterogeneous Systems by Multi-Level Finite Element Modeling, Computer Methods in Applied Mechanics and Engineering, 155, 181-192 (1998).

53. V. Kouznetsova, W. A. M. Brekelmans, and F. P. T. Baaijens, An Approach to Micro-Macro Modeling of Heterogeneous Materials, Computational Mechanics 27, 37-48 (2001).

54. W. E, B. Engquist, X. Li, W. Ren, and E. Vanden-Eijnden, Heterogeneous Multiscale Methods: a Review, Communications in Computational Physics, 2, 367-450 (2007).

55. L. Tan and N. Zabaras, Multiscale Modeling of Alloy Solidification Using a Database Approach, Journal of Computational Physics 227, 728–754 (2007).

56. O. Rohrle, J. B. Davidson, and A. J. Pullan, Bridging Scales: A Three-Dimensional Electromechanical Finite Element Model of Skeletal Muscle, SIAM Journal on Scientific Computing, 30, 2882–2904 (2008).

57. N. V. Queipo, R. T. Haftka, W. Shyy, T. Goel, R. Vaidyanathan, and P. K. Tucker, Surrogate-based Analysis and Optimization, Progress in Aerospace Sciences, 41, 1-28 (2005).

58. T. Goel, S. Thakur, R. T. Haftka, W. Shyy, and J. Zhao, Surrogate model-based strategy for cryogenic cavitation model validation and sensitivity evaluation, International Journal of Numerical Methods in Fluids, 58, 969-1007 (2008).

59. A. Samad, K.-Y. Kim, T. Goel, R. T. Haftka, and W. Shyy, Multiple Surrogate Modeling for Axial Compressor Blade Shape Optimization, Journal of Propulsion and Power, 24 (2), 302-310 (2008).

60. B. D. Marjavaara, T. S. Lundstrom, T. Goel, Y. Mack, and W. Shyy, Hydraulic Turbine Diffuser Shape Optimization by Multiple Surrogate Model Approximations of Pareto Fronts, 129, 1228-1240 (2007).

61. Y.-C. Cho, B. Jayaraman, F. A. C. Viana, R. T. Haftka, and W. Shyy, Surrogate Modeling for Characterizing the Performance of Dielectric Barrier Discharge Plasma Actuator, 46th AIAA Aerospace Sciences Meeting and Exhibit, January 7-10, 2008, Reno, Nevada.

62. P. Trizila, C.-K. Kang, M. Visbal, and W. Shyy, A Surrogate Model Approach in 2D versus 3D Flapping Wing Aerodynamic Analysis, 12th AIAA/iSSMO Multidisciplinary Analysis and Optimization Conference, Spetember 10-12, 2008, Victoria, British Columbia, Canada.

63. J. I. Madsen, W. Shyy and R. T. Haftka, Response Surface Techniques for Diffuser Shape Optimization, AIAA Journal, 38, 1512-1518 (2000).

64. T. Goel, R. Vaidyanathan, R. T. Haftka, W. Shyy, N. V. Queipo, and K. Tucker, Response Surface Approximation of Pareto Optimal Front in Multi-Objective Optimization, Computer Methods in Applied Mechanics and Engineering, 196, 879–893 (2007).

65. G. E. P. Box and K. B. Wilson, On the Experimental Attainment of Optimum Conditions, Journal of the Royal Statistical Society, Series B (Methodological), 13, pp. 1-45 (1951).

66. M. D. McKay and R. J. Beckman and W. J. Conover, A Comparison of Three Methods for Selecting Values of Input Variables in the Analysis of Output from a Computer Code, Technometrics, 21, 239-245 (1979).

67. A. Hedayat, N. Sloane, and J. Stufken, Orthogonal Arrays: Theory and Applications, Springer, Series in Statistics, Berlin: Springer, 1999.

68. G. Matheron, Principles of Geostatistics, Economic Geology, 58:1246–66 (1963).

69. R. H. Myers, and D. C. Montgomery, Response Surface Methodology: Process and Product Optimization Using Designed Experiments, pp. 17-48, John Wiley & Sons Inc: New York, 1995.

70. R. Kohavi, A Study of Cross-Validation and Bootstrap for Accuracy Estimation and Model Selection, "Proceedings of the Fourteenth International Joint Conference on Artificial Intelligence, 2, 1137-1143 (1995).

71. F. A. C. Viana, R. T. Haftka, and V. Steffen, Multiple Surrogates: How Cross-Validation Errors Can Help Us to Obtain the Best Predictor, Structural and Multidisciplinary Optimization, In Press, DOI 10.1007/s00158-008-0338-0.

72. T. Geol, R. T. Haftka, W. Shyy and N. V. Queipo, Ensemble of Surrogates, Structural and Multidisciplinary Optimization, 33(3), 199-216 (2007).

73. I. M. Sobol, Sensitivity Analysis for Nonlinear Mathematical Models. Mathematical Modeling and Computational Experiment, 1(4), 407–414 (1993).

CHAPTER II

NUMERICAL SIMULATION OF INTERCALATION-INDUCED STRESS IN LI-ION BATTERY ELECTRODE PARTICLES*

1. INTRODUCTION

Severe, particle-level strains induced during both production and cycling have been putatively linked to lifetime limiting damage in lithium-ion cells. Intercalation and deintercalation of Li ions into cathodic lattices, including $LiCoO_2$ [1], $LiMn_2O_4$ [2] and $LiFePO_4$ [3], have been postulated to result in fraction inside the particles, as determined by experimentation on model systems. In $LiMn_2O_4$ for example, 6.5% percent of volume change has been reported when Mn_2O_4 is lithiated into $LiMn_2O_4$ [4]. The simulation of $LiMn_2O_4$ indicated that intercalation-induced stress could exceed the ultimate strength of the material [5]. Also, stress generation due to cell-scale loads by compression during manufacturing has been shown to result in localized particle stresses that are much higher in the graphite anode material [6] (the ratio between local and global stresses is around 25 to 140). Indeed, stresses of these orders exceed known strength of the materials which comprise the most commonly used, and most promising, cathode materials (Table 2.1 [4, 7, 8, 9]).

* The material in this chapter is a published paper: X. Zhang, W. Shyy, and A. M. Sastry, Numerical Simulation of Intercalation-Induced Stress in Li-Ion Battery Electrode Particles, *Journal of the Electrochemical Society,* 154(10) A910-A916 (2007).

material	measurement technique	stress or strain
$LiCoO_2$ film [7]	laser beam deflection	~1GPa (stress)
$LiMn_2O_4$ film [8]	laser beam deflection	~0.64GPa (stress)
$LiMn_2O_4$ [4]	neutron-diffraction	0.027 (strain)
$LiFePO_4$ [9]	X-ray diffraction	0.022 (strain)

Table 2.1: Stress and strain in cathode materials in the intercalation process.

Stress generation due to Li-intercalation, and more generally in other processes, has been modeled in prior work at the particle scale. Christensen and Newman estimated stress generation in the lithium insertion process in carbon anode [10] and $LiMn_2O_4$ cathode [5] particles. More broadly, stresses induced by species diffusion have been studied in other fields including metal oxidation and semiconductor doping. Prussin [11] first treated diffusion induced stress by analogy to thermal stress. In this study, stress generation during doping of boron and phosphorus into silicon wafer was studied. Li [12] studied diffusion-induced stress or chemical stress in elastic media of simple geometries following this method, as well. Yang [13] studied the evolution of chemical stress in a thin plate by considering the interaction between chemical stress and diffusion Prussin's thermal stress analogy [11].

Though these sets of efforts offer a means of stress estimation at the particle scale, by different physical assumptions, the implementations to date have not been applied to the problem of three-dimensional stresses. Because of the presently unknown contributions of manufacturing- and intercalation-induced stresses in Li-cells, this correlation is critical: in determining optimal materials and manufacturing methods for these cells. Both global and localized loads must be estimated, in order to select materials able to resist fracture. Further, the role of localized particle fracture in capacity fade has been implied, but not quantified, given the general lack of understanding of localized loads in batteries.

Thus, the present work is focused on determining localized particle stresses in cathodic particles. Here we select the $LiMn_2O_4$ system following [14, 15, 16, 17, 18] on battery performance modeling, [19, 20] on atomic scale simulation of structure and

diffusion properties, and [5] on intercalation-induced stress simulation because of the low cost and environmental safety of $LiMn_2O_4$. We have the following objectives in this study:

1) To determine diffusion-induced stresses according to an analogy to thermal stress, following [11, 12 and 13] for single particles, and determine the correspondence with prior work in Li cells [5];
2) To verify the implementation of a single-particle model numerically, using a finite difference scheme and reproduction of simple results; and
3) To implement this model into a full finite element scheme, and simulate stresses induced by intercalation in particles of nonspherical geometry.

2. METHODS

2.1 Stress-Strain Relations

For intercalation processes, the lattice constants of the material may be assumed to change linearly [4] with the volume of ions inserted, which results in stresses. Therefore, one can calculate intercalation-induced stress by analogy to thermal stress. Prussin [11] previously treated concentration gradients analogously to those generated by temperature gradients in an otherwise unstressed body.

Stress-strain relations including thermal effects are written classically for an elastic body [21], as

$$\varepsilon_{xx} - \alpha T = \frac{1}{E}\left[\sigma_{xx} - \nu\left(\sigma_{yy} + \sigma_{zz}\right)\right] \tag{1a}$$

$$\varepsilon_{yy} - \alpha T = \frac{1}{E}\left[\sigma_{yy} - \nu\left(\sigma_{xx} + \sigma_{zz}\right)\right] \tag{1b}$$

$$\varepsilon_{zz} - \alpha T = \frac{1}{E}\left[\sigma_{zz} - \nu\left(\sigma_{xx} + \sigma_{yy}\right)\right] \tag{1c}$$

$$\varepsilon_{xy} = \frac{\sigma_{xy}}{2G}, \varepsilon_{yz} = \frac{\sigma_{yz}}{2G}, \varepsilon_{xz} = \frac{\sigma_{xz}}{2G} \tag{1d}$$

where ε_{ij} are strain components, σ_{ij} are stress components, E is Young's modulus, ν is Poisson's ratio, G is modulus of elasticity in shear, α is thermal expansion coefficient, and T is the temperature change from the original value. Analogously, the stress-strain relation with the existing of concentration gradients can be written as [13]

$$\varepsilon_{ij} = \frac{1}{E}\left[(1+\nu)\sigma_{ij} - \nu\sigma_{kk}\delta_{ij}\right] + \frac{\tilde{c}\Omega}{3}\delta_{ij} \tag{2}$$

where $\tilde{c} = c - c_0$ is the concentration change of the diffusion species from the original (stress-free) value, and Ω is partial molar volume of solute. Eq. (2) can be rewritten to obtain the expression for the components of stresses,

$$\sigma_{ij} = 2\mu\varepsilon_{ij} + \left(\lambda\varepsilon_{kk} - \beta\tilde{c}\right)\delta_{ij} \tag{3}$$

where $\mu = E/2(1+\nu)$, $\lambda = 2\nu\mu/(1-2\nu)$, and $\beta = \Omega(3\lambda + 2\mu)/3$. As usual in elasticity, the strain tensor is related to displacement $\mathbf{u}$ as [21]

$$\varepsilon_{ij} = \frac{1}{2}\left(\frac{\partial u_i}{\partial x_j} + \frac{\partial u_j}{\partial x_i}\right) \tag{4}$$

and the equilibrium equation, neglecting body forces, is [21]

$$\sigma_{ij,i} = 0 \quad (j = 1, 2, 3) \tag{5}$$

Substitution of Eq. (3) and (4) into (5), leads to the displacement equations [22]

$$\mu\nabla^2 u_i + (\lambda + \mu)u_{k,ki} - \beta\tilde{c}_{,i} = 0 \quad (i = 1, 2, 3). \tag{6}$$

The boundary condition for the case of a single particle is that the particle surface is traction-free. This condition can be expressed as [22]

$$p_{nx} = \sigma_{xx} l + \sigma_{yx} m + \sigma_{zx} n = 0 \tag{7a}$$

$$p_{ny} = \sigma_{xy} l + \sigma_{yy} m + \sigma_{zy} n = 0 \tag{7b}$$

$$p_{nz} = \sigma_{xz} l + \sigma_{yz} m + \sigma_{zz} n = 0 \tag{7c}$$

where l, m, n denote the direction cosines between the external normal and each axis. Substitution of Eq. (3) and (4) into boundary conditions (7), yields

$$\mu\left(u_{i,j} + u_{j,i}\right)n_j + \left(\lambda u_{k,k} - \beta c\right)n_i = 0 \quad i = 1, 2, 3 \tag{8}$$

where $n_1 = l$, $n_2 = m$ and $n_3 = n$. Therefore, we are left to solve Eq. (6), with boundary condition (8).

2.2 Diffusion Equation

As shown in Eq. (2) and (3), concentrations are needed to calculate intercalation-induced stresses. To obtain a concentration profile, the insertion and extraction of ions are modeled as a diffusion process. The effect of existing electrons in the solid on the species flux of lithium can be neglected, because electrons are much more mobile than intercalated atoms [23]. The chemical potential gradient is the driving force for the movement of lithium ions. The velocity of lithium ions can be expressed as

$$\mathbf{v} = -M\nabla\mu \tag{9}$$

where M is the mobility of lithium ions and μ is the chemical potential. The species flux can then be written as [23]

$$\mathbf{J} = c\mathbf{v} = -Mc\nabla\mu \tag{10}$$

where c is the concentration of the diffusion component (lithium ions).

The electrochemical potential in an ideal solid solution can be expressed as [13, 24]

$$\mu = \mu_0 + RT \ln X - \Omega \sigma_h \tag{11}$$

where μ_0 is a constant, R is gas constant, T is absolute temperature, X is the molar fraction of lithium ion, Ω is partial molar volume of lithium ion, and σ_h is the hydrostatic stress, which is defined as $\sigma_h = (\sigma_{11} + \sigma_{22} + \sigma_{33})/3$ (where σ_{ij} are the elements in stress tensor). Eq. (10) and (11) show that the diffusion flux depends on concentration, temperature, and stress field. Substitution of (11) into (10), assuming temperature is uniform, and noting that

$$\nabla(RT \ln X) = RT \frac{1}{X} \nabla X = RT \frac{1}{c} \nabla c \,, \tag{12}$$

an expression of species flux (when there is no temperature gradient inside the particle) can be obtained as

$$\mathbf{J} = -D\left(\nabla c - \frac{\Omega c}{RT} \nabla \sigma_h \right) \tag{13}$$

where $D = MRT$ is the diffusion coefficient. Conservation of species gives

$$\frac{\partial c}{\partial t} + \nabla \cdot \mathbf{J} = 0 \,. \tag{14}$$

Then, substituting Eq. (13) into (14) gives, finally,

$$\frac{\partial c}{\partial t} = D\left(\nabla^2 c - \frac{\Omega}{RT} \nabla c \cdot \nabla \sigma_h - \frac{\Omega c}{RT} \nabla^2 \sigma_h \right), \tag{15}$$

as the governing equation for the diffusion process. The initial condition is $c = c_0$, with the boundary condition

$$\mathbf{J} = -D\left(\nabla c - \frac{\Omega c}{RT} \nabla \sigma_h \right) = \frac{i_n}{F} \tag{16}$$

where i_n is the current density on the particle surface (which is assumed to be a constant, known value in this study), and F is Faraday's constant.

2.3 Numerical Methods

a. Finite Difference Method for 1-D Problem

For the case of a spherical particle, the above equations become one-dimensional. The stress tensor contains two independent components, radial stress σ_r and tangential stress σ_t. The equilibrium equation (refer to Eq. (5)) for this case is simply

$$\frac{\mathrm{d}\sigma_r}{\mathrm{d}r} + \frac{2}{r}\left(\sigma_r - \sigma_t\right) = 0\,, \tag{17}$$

and the stress-strain relations (referring to Eq. (2)) are

$$\varepsilon_r = \frac{1}{E}\left(\sigma_r - 2\nu\sigma_t\right) + \frac{\Omega}{3}\widetilde{c} \tag{18}$$

$$\varepsilon_t = \frac{1}{E}\left[\sigma_t - \nu\left(\sigma_r + \sigma_t\right)\right] + \frac{\Omega}{3}\widetilde{c}\,. \tag{19}$$

The strain-displacement relations (referring to Eq. (4)) are

$$\varepsilon_r = \frac{\mathrm{d}u}{\mathrm{d}r}\,, \quad \varepsilon_t = \frac{u}{r}\,, \tag{20}$$

and displacement equation (refer to Eq. (6)) is

$$\frac{\mathrm{d}^2u}{\mathrm{d}r^2} + \frac{2}{r}\frac{\mathrm{d}u}{\mathrm{d}r} - \frac{2u}{r^2} = \frac{1+\nu}{1-\nu}\frac{\Omega}{3}\frac{\mathrm{d}\widetilde{c}}{\mathrm{d}r}\,. \tag{21}$$

Integration of this equation yields a solution for u, from which stresses may be obtained. Noting that stresses are finite at the center of the sphere ($r = 0$), and that radial stresses are zero, $\sigma_r = 0$, at the particle surface ($r = r_0$), the two constants in the solution can be determined, as

$$\sigma_r = \frac{2\Omega E}{3(1-\nu)}\left(\frac{1}{r_0^{\,3}}\int_0^{r_0}\widetilde{c}\,r^2\mathrm{d}r - \frac{1}{r^3}\int_0^{r}\widetilde{c}\,r^2\mathrm{d}r\right), \text{ and} \tag{22}$$

$$\sigma_t = \frac{\Omega E}{3(1-\nu)}\left(\frac{2}{r_0^{\,3}}\int_0^{r_0}\widetilde{c}\,r^2\mathrm{d}r + \frac{1}{r^3}\int_0^{r}\widetilde{c}\,r^2\mathrm{d}r - \widetilde{c}\right). \tag{23}$$

Eq. (22) shows that radial stress actually depends upon the difference between the global and local averages of concentration.

The diffusion equation is (referring to Eq. (15)),

$$\frac{\partial c}{\partial t} = D\left[\frac{\partial^2 c}{\partial r^2} + \frac{2}{r}\frac{\partial c}{\partial r} - \frac{\Omega}{RT}\frac{\partial c}{\partial r}\frac{\partial \sigma_h}{\partial r} - \frac{\Omega c}{RT}\left(\frac{\partial^2 \sigma_h}{\partial r^2} + \frac{2}{r}\frac{\partial \sigma_h}{\partial r}\right)\right]. \tag{24}$$

Eqs. (22) (23) allow calculation of hydrostatic stress, as

$$\sigma_h = (\sigma_r + 2\sigma_t)/3 = \frac{2\Omega E}{9(1-\nu)}\left(\frac{3}{r_0^{\,3}}\int_0^{r_0}\widetilde{c}\,r^2\mathrm{d}r - \widetilde{c}\right). \tag{25}$$

By assuming that the characteristic time for elastic deformation of solids is much smaller than that for atomic diffusion, the elastic deformation can be treated as quasistatic [13]. Therefore, Eq. (25) can be substituted into Eq. (24) to obtain

$$\frac{\partial c}{\partial t} = D\left[\frac{\partial^2 c}{\partial r^2} + \frac{2}{r}\frac{\partial c}{\partial r} + \theta\left(\frac{\partial c}{\partial r}\right)^2 + \theta c\left(\frac{\partial^2 c}{\partial r^2} + \frac{2}{r}\frac{\partial c}{\partial r}\right)\right] \tag{26}$$

where $\theta = \dfrac{\Omega}{RT}\dfrac{2\Omega E}{9(1-\nu)}$.

Substituting (25) into boundary conditions (16), one has

$$\mathbf{J} = -D(1+\theta c)\frac{\partial c}{\partial r} = \frac{i_n}{F} \quad \text{at } r = r_0 \tag{27}$$

In this way, the two variables, concentration and stress, are decoupled.

To solve the above equation numerically, it, along with boundary and initial condition, is transformed into dimensionless form first, as

$$\frac{\partial \hat{c}}{\partial \hat{t}} = \frac{\partial^2 \hat{c}}{\partial \hat{r}^2} + \frac{2}{r}\frac{\partial \hat{c}}{\partial \hat{r}} + \hat{\theta}\left(\frac{\partial \hat{c}}{\partial \hat{r}}\right)^2 + \hat{\theta}\hat{c}\left(\frac{\partial^2 \hat{c}}{\partial \hat{r}^2} + \frac{2}{\hat{r}}\frac{\partial \hat{c}}{\partial \hat{r}}\right) \tag{28}$$

$$0 \le \hat{r} \le 1, \qquad 0 \le \hat{t} \le \hat{T} \text{ (where } \hat{T} \text{ satisfies } \hat{c}\left(\hat{r}=1, \hat{t}=\hat{T}\right)=1\text{)}$$

$$\hat{r}=1, \ -\left(1+\hat{\theta}\hat{c}\right)\frac{\partial \hat{c}}{\partial \hat{r}} = I; \qquad \hat{r}=0, \ \frac{\partial \hat{c}}{\partial \hat{r}} = 0$$

$$\hat{t}=0, \quad \hat{c} = c_0 / c_{\max}$$

where dimensionless variables are defined as

$$\hat{r} = \frac{r}{r_0} \qquad \hat{t} = \frac{tD}{r_0^{\ 2}} \qquad \hat{c} = \frac{c}{c_{\max}} \qquad \hat{\theta} = \theta c_{\max} \qquad I = \frac{i_n r_0}{D c_{\max} F}$$

In the above equations, $c_{\max}$ is the stoichiometric maximum concentration and c_0 is the initial concentration. It may be seen that the effect of discharge current density, particle radius and diffusion coefficient are all combined into the dimensionless current density I.

The numerical procedure is as follows. For each time step, concentration distribution is solved first by Eq. (28). Then, the concentration is substituted into Eq. (22) (23) to calculate stresses. Eq. (28) is a nonlinear, parabolic partial differential equation. The finite difference method is used here to solve the equation.

First Eq. (28) is rewritten as

$$\frac{\partial \hat{c}}{\partial \hat{t}} = (1+\hat{\theta}\hat{c})\frac{\partial^2 \hat{c}}{\partial \hat{r}^2} + \left(\frac{2}{\hat{r}} + \hat{\theta}\frac{\partial \hat{c}}{\partial \hat{r}} + \frac{2\hat{\theta}\hat{c}}{\hat{r}}\right)\frac{\partial \hat{c}}{\partial \hat{r}}. \tag{29}$$

To discretize the differential equation into difference equations, the problem is linearized by taking the value from the previous time step for the terms in the two parentheses on the right hand side. The Crank-Nicolson method is used for other terms. The difference equation obtained is

$$\frac{\hat{c}_i^{n+1}-\hat{c}_i^n}{\Delta\hat{t}} = (1+\hat{\theta}\hat{c}_i^n)\frac{\left(\hat{c}_{i+1}^{n+1}+\hat{c}_{i-1}^{n+1}-2\hat{c}_i^{n+1}\right)+\left(\hat{c}_{i+1}^{n}+\hat{c}_{i-1}^{n}-2\hat{c}_i^{n}\right)}{2\left(\Delta\hat{r}\right)^2} + \left(1+\frac{2}{\hat{r}_i}+\hat{\theta}\frac{\hat{c}_{i+1}^n-\hat{c}_{i-1}^n}{2\Delta\hat{r}}+\frac{2}{\hat{r}_i}\hat{\theta}\hat{c}_i^n\right)\frac{\left(\hat{c}_{i+1}^{n+1}-\hat{c}_{i-1}^{n+1}\right)+\left(\hat{c}_{i+1}^{n}-\hat{c}_{i-1}^{n}\right)}{2\left(2\Delta\hat{r}\right)} \tag{30}$$

Terms including $1/\hat{r}$ will be singular at the particle center $\hat{r}=0$. To solve this difficulty, noting that

$$\frac{\partial\hat{c}}{\partial\hat{r}} = 0 \qquad \text{when } \hat{r}=0 \tag{31}$$

L'Hopital's rule can be used

$$\lim_{\hat{r}\to 0}\frac{1}{\hat{r}}\frac{\partial\hat{c}}{\partial\hat{r}} = \frac{\partial^2\hat{c}}{\partial\hat{r}^2} \tag{32}$$

to eliminate the $1/\hat{r}$ factor. Thus, Eq. (28) becomes

$$\frac{\partial\hat{c}}{\partial\hat{t}} = (3+3\hat{\theta}\hat{c})\frac{\partial^2\hat{c}}{\partial\hat{r}^2}+\left(\hat{\theta}\frac{\partial\hat{c}}{\partial\hat{r}}\right)\frac{\partial\hat{c}}{\partial\hat{r}}, \tag{33}$$

which has no singularity at $\hat{r}=0$. Therefore, Equation (33) will be solved at $\hat{r}=0$ while Equation (29) is solved elsewhere.

At two boundary points, imaginary points (out of the boundary) are used to discretize the governing equation; the concentration values of these imaginary points are obtained by central differencing of the flux boundary condition at the boundary points.

The Thomas algorithm is used to solve the tridiagonal system of the difference equations. The simulation is halted when the concentration on the particle surface $\hat{r} = 1$ reaches the stoichiometric maximum.

b. Finite Element Method for 3-D Problem

The three-dimensional problem was simulated using FEMLAB (COMSOL Multiphysics®). Two models are included in the multiphysics simulation, PDE (partial differential equation) model (general form) and solid stress-strain model. In PDE model, the diffusion process is described by the generalized form of PDE

$$\frac{\partial c}{\partial t} + \nabla \cdot \Gamma = 0 \tag{34}$$

where

$$\Gamma = -D\left(\nabla c - \frac{\Omega c}{RT} \nabla \sigma_h \right). \tag{35}$$

In the solid stress-strain model, 'thermal expansion' is included as a load based on the variable of concentration c instead of temperature in thermal stress calculations.

2.4 Material Properties

All the material properties used in the simulation for Mn_2O_4 are listed in Table 2.2 [5, 25]. From Eq. (2), we see that that partial molar volume plays a role analogous to a thermal expansion coefficient, in calculating intercalation-induced stress. To obtain the value for this property, the volume change of 6.5% for $y = 0.2$ to $y = 0.995$ of $Li_yMn_2O_4$ is used [5]. The volume change of 6.5%, giving a strain of 0.0212, corresponds to the concentration change from $y = 0.2$ to $y = 0.995$. Therefore, by noting the analogy between thermal expansion coefficient and $\Omega/3$, partial molar volume is

parameter	symbol and dimensions	value
Young's modulus	E (GPa)	10 [25]
Poisson's ratio	ν	0.3 [25]
diffusion coefficient	D (m^2/s)	7.08×10^{-15} [5]
partial molar volume	Ω (m^3/mol)	3.497×10^{-6}
stoichiometric maximum concentration	c_{max} (mol/m^3)	2.29×10^{4}

Table 2.2: Material properties of Mn_2O_4.

$$\Omega = \frac{0.0212 \times 3}{(0.995 - 0.2)c_{\max}} = 3.497 \times 10^{-6} \text{ m}^3/\text{mol}.$$

3. RESULTS AND DISCUSSIONS

3.1 1-D Finite Difference Simulations

Christensen and Newman [5] modeled the stress generated in $Li_yMn_2O_4$ during lithium intercalation on the 4-V plateau (0.2<y<1). The same parameters and properties are used here, except for the diffusion coefficient. In their simulation, they used a state of charge dependant diffusion coefficient that includes a binary interaction parameter and a thermodynamic factor. Here, a constant diffusion coefficient is used, taking the value of the reference binary interaction parameter in their paper. The simulation results from the thermal stress analogy model and the Christensen and Newman model are shown in Figure 2.1. Although different approaches are applied to calculate the intercalation-induced stress, the results qualitatively show the same trend.

We used the 1D model to simulate cycling of the active material between y=0 and y=1, giving an initial condition for Eq. (26) of $c_0 = 0$. Results show that maximum radial stress locates at the center of the particle. The magnitude of the spatial maximum dimensionless radial stress is given by

$$\hat{\sigma}_{r,\max} = \frac{\sigma_{r,\max}}{E} = \frac{2\Omega c_{\max}}{3(1-\nu)}\left(\int_0^1 \hat{c}\hat{r}^2 \mathrm{d}\hat{r} - \frac{1}{3}\hat{c}\Big|_{\hat{r}=0}\right). \tag{36}$$

Figure 2.2 shows how dimensionless maximum radial stress $\hat{\sigma}_{r,\max}$ (both temporally and spatially during the discharge process) varies with dimensionless current density (or dimensionless boundary flux) I.

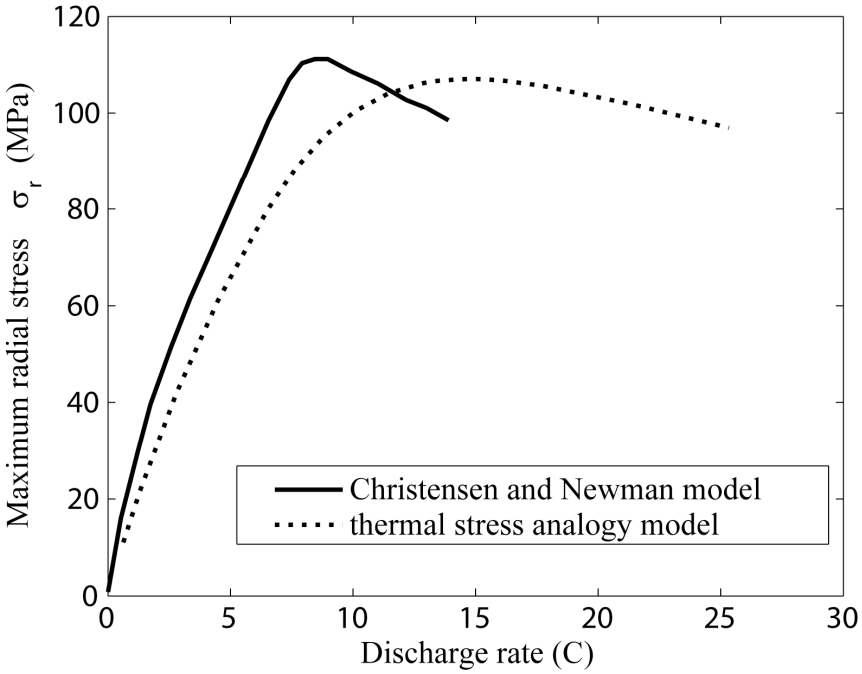

Figure 2.1: Comparison of simulation results of two models.

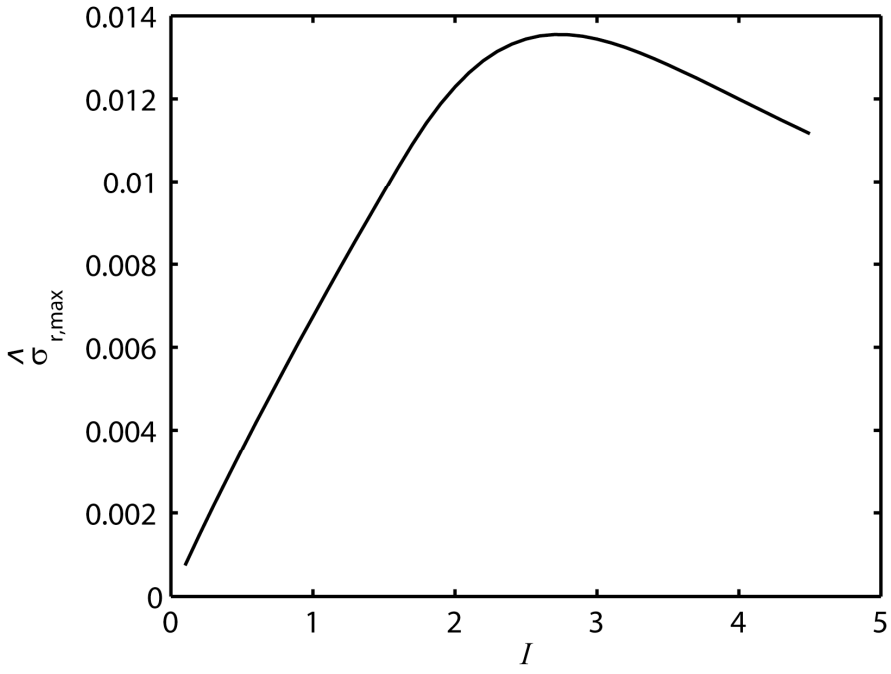

Figure 2.2: Maximum dimensionless radial stress versus dimensionless current density.

As shown in Figure 2.2, maximum radial stress (spatially and temporally) inside an electrode particle during the discharge process increases with increasing dimensionless current density when $0 < I < 2.7$. However, maximum radial stress decreases with increasing dimensionless current density when it is larger than 2.7. The decrease of stress occurs because the concentration profile is not fully developed, so that the global average term (first term in the parenthesis) in Eq. (36) decreases with dimensionless current density, while the local average (second term in the parenthesis) remains constant. This is not desirable in the cycling of batteries, because it reduces material utilization. Therefore, only the increasing branch of the curve is actually feasible. The increasing branch shows that increase of discharge current density and particle radius will increase the intercalation-induced stress. In other words, smaller particles should be used to reduce intercalation-induced stresses.

As mentioned earlier, the model used here to simulate the intercalation-induced stress is a diffusion-stress coupling model. The effect of stress on diffusion will be discussed briefly using the one-dimensional equations for a spherical particle. Substituting Eq. (25) into (13), we obtain

$$\mathbf{J} = -D(1+\theta c)\frac{\partial c}{\partial r}. \tag{37}$$

In Eq. (37), θc is always a positive number, and the effective diffusion coefficient is essentially $D(1+\theta c) > D$. Therefore, the diffusion is enhanced due to the extra term θc , which basically comes from hydrostatic stress gradient term in Eq. (13). In other words, stress enhances the diffusion. This stress enhancement effect is also demonstrated numerically, as shown in Figure 2.3. It shows the concentration profile at t=1000s with

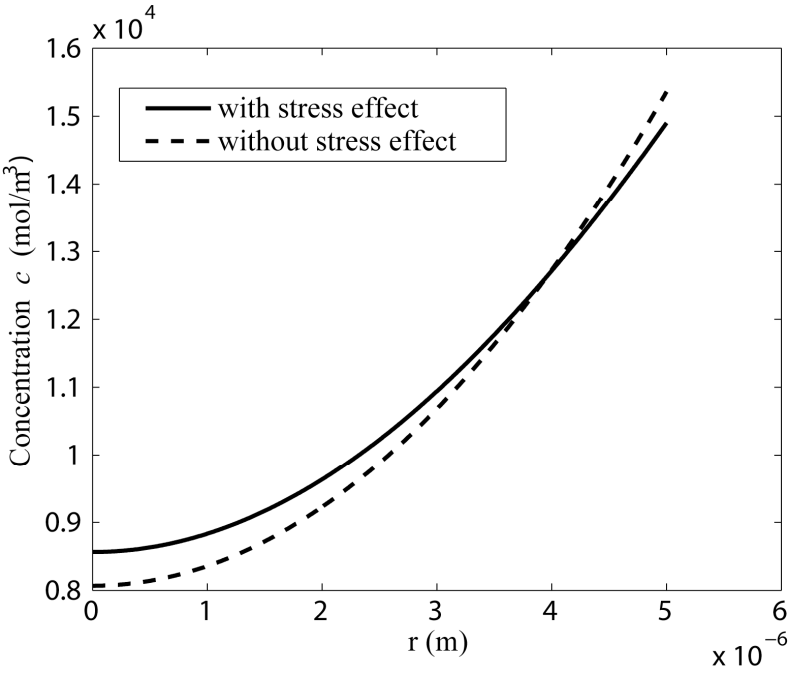

Figure 2.3: Numerical results for the effects of stress.

discharge current density $i = 2\ \mathrm{A/m^2}$ on the surface. The profile including the effect of stress has a smaller gradient than that excluding the stress effect, confirming that stress enhances diffusion.

Substituting the material properties into the expression of $\theta = 2\Omega^2 E/[9(1-\nu)RT]$, we obtain $\theta = 1.557\times10^{-5}\ \mathrm{m^3/mol}$. If the maximum concentration is used, $\theta c_{\max} = 0.356$, which is not negligible compared to unity. Therefore, for the case of $LiMn_2O_4$, the stress effect cannot be neglected. From the expression for θ, it can be observed that θ has smaller magnitude when the material has smaller modulus E and smaller partial molar volume Ω. Thus, the stress effect on diffusion may be negligible when the material is soft (i.e. having a low modulus).

3.2 3-D Finite Element Simulation Results

The 1-D finite difference simulation, with 4001 grid points and a time step of 0.001s, was used as the reference solution to study the convergence of finite element method. Figure 2.4 shows the 2-norm errors (differences) between the finite element solutions and finite difference reference solutions at t=1000s. The parameters used in the simulations are current density $i = 2\ \mathrm{A/m^2}$, and particle radius $r_0 = 5\mu\mathrm{m}$. The finite element solutions converged to the reference solution as the number of elements used increased. At the same time, Figure 2.4 also shows that solutions from 1-D finite difference method and 3-D finite element method were consistent, because the nondimensionalized errors of concentration and stress from 17359 elements simulation were 6.5×10^{-7} and 1.5×10^{-5} respectively (if nondimensionalized by the maximum values at t=1000s inside the particle).

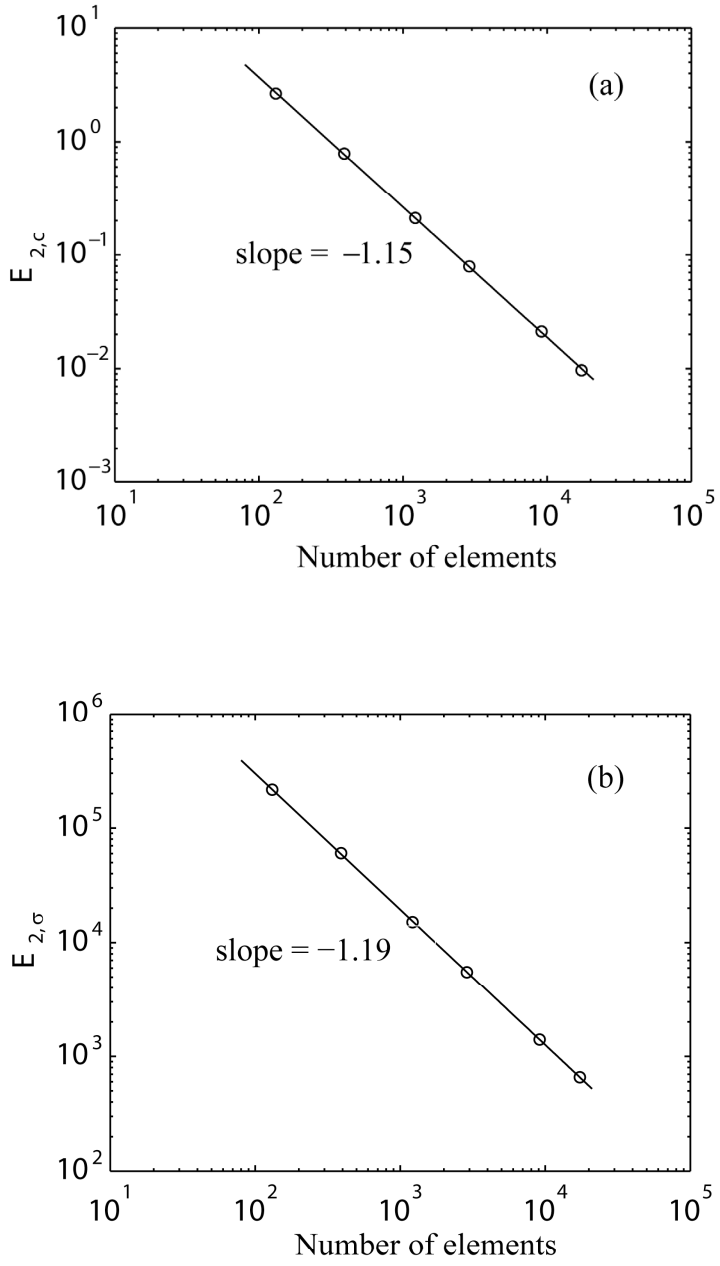

Figure 2.4: Convergence plot of finite element solutions for: (a) hydrostatic stress and (b) concentration.

To study the effect of aspect ratios on the intercalation-induced stress, ellipsoids with different aspect ratios were studied. The current density on the surface is fixed at $i = 2\ \mathrm{A/m^2}$. For the ellipsoid, the lengths of three semi-axes a , b and c satisfy $a = b$, and the aspect ratio is defined as $\alpha = c/a$, as sketched in Figure 2.5. The volumes of the ellipsoids were fixed, at $V = 4\pi \times 5^3/3\ \mu\mathrm{m}^3$. A set of simulations, with different aspect ratios, were run by FEMLAB.

Characteristic solution profiles of concentration, von Mises stress and shear stress σ_{yz} are shown in Figure 2.6 at the end of the discharge process (when the surface concentration reaches the stoichiometric maximum) for an ellipsoid with aspect ratio 1.953. Figure 2.6 shows that 1) the concentration is higher around the poles; 2) the von Mises stress is larger around the equator; and 3) shear stress has its maximum on the surface. The solution profiles have the same patterns for other ellipsoids with different aspect ratios.

Figure 2.7 shows how the maximum von Mises stress inside the particle varies during the discharge process for particles with different aspect ratios. It takes less time for particles with larger aspect ratios to completely discharge. Also, during discharge, von Mises stress increases first, and then drops. In Figure 2.7, it can be observed that when aspect ratio increases, the stress increases first (for aspect ratios from 1.0 to 1.37) and then decreases (for aspect ratios from 1.37 to 3.81). For ellipsoids with aspect ratio 2.92 and 3.81, the intercalation-induced stress is smaller than that inside a sphere (aspect ratio 1.0).

Figure 2.8 shows how aspect ratio affects (a) peak value of maximum von Mises stress, and (b) peak value of maximum shear when the volumes of particles are fixed.

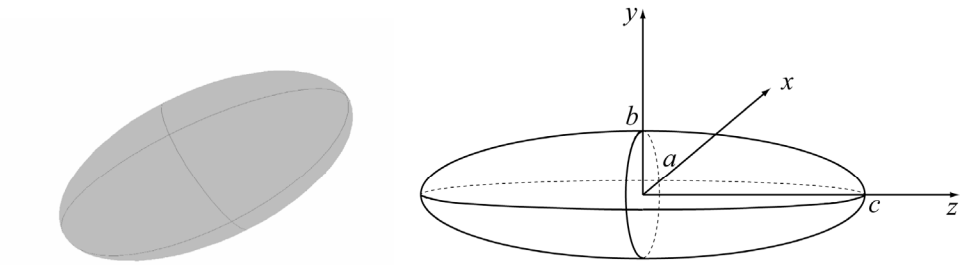

Figure 2.5: Schematic of an ellipsoidal particle, with coordinate system.

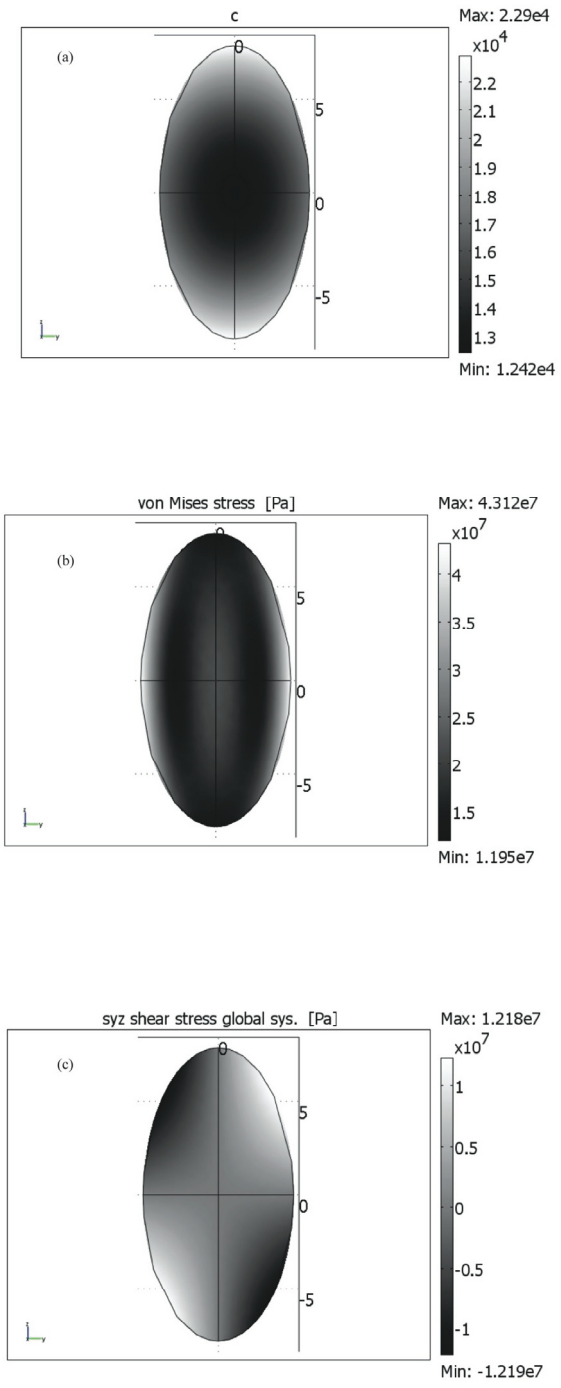

Figure 2.6: Solutions at the end of discharge for an ellipsoid of aspect ratio 1.953, (a) concentration, (b) von Mises stress, and (c) shear stress.

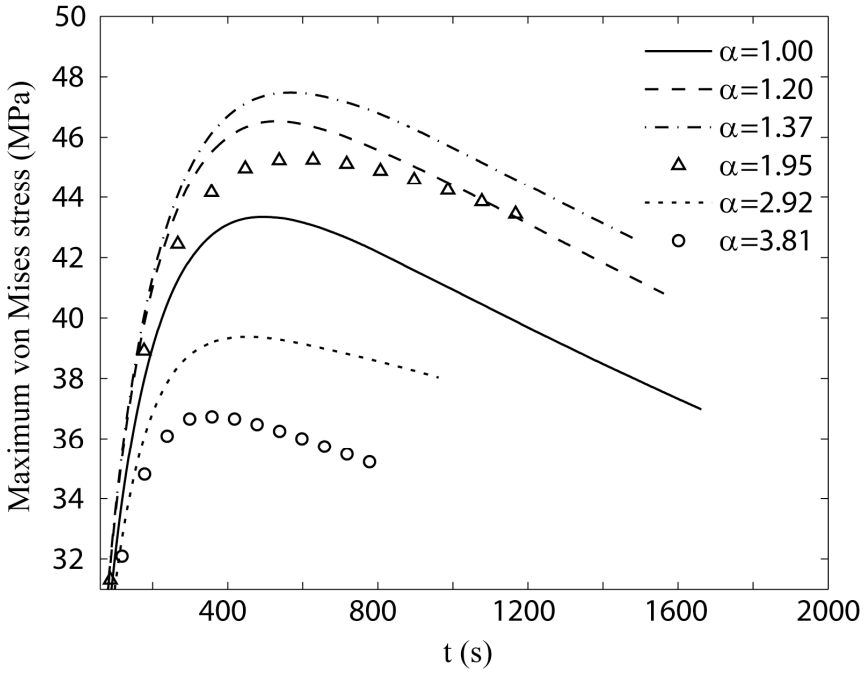

Figure 2.7: Maximum von Mises stress during discharge, for various ellipsoids.

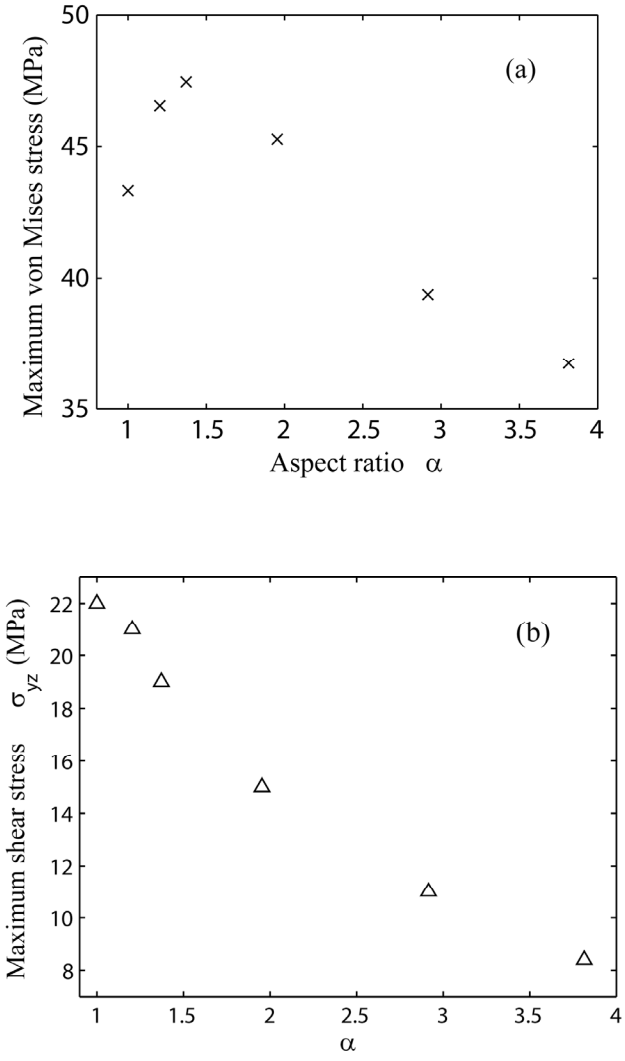

Figure 2.8: The effect of aspect ratio, for fixed particle volume.

Figure 2.8 (a) shows that the peak value of maximum von Mises stress inside the particle increases first and then decreases as the aspect ratio increases. Once the aspect ratios are larger than 2.2, the maximum von Mises stress is less than that inside spherical particles (aspect ratio 1). Figure 2.8 (b) shows that peak value of maximum shear stress decreases as aspect ratio increases. The results of Figure 2.8 show that particles with larger aspect ratios have less intercalation-induced stress generation, when the particle volume is preserved.

The peak values of maximum von Mises stresses are shown in Figure 2.8 (a). Maximum stress first increases, then decreases with aspect ratio. This is due to two competing effects. When particle volume is preserved, increased aspect ratios result in increase of the longer semi-axis *c,* and reduction of shorter, semi-axes *a* and *b*. Elongation of the longer semi-axis tends to increase maximum stress, while reduction of the shorter semi-axes tends to decrease the maximum stress. This competition results in a global maximum of stress at an aspect ratio of ~1.37.

To further illustrate the effect of semi-axes on maximum stress, an additional set of simulations were performed, in which the shorter semi-axes *a* and *b* were fixed, and aspect ratio α was increased by elongation of the longer semi-axis, *c*. Results, obtained with a discharge current density $i = 2\ \mathrm{A/m^2}$, are shown in Figure 2.9. Stress first increases with aspect ratio because of the increase of longer semi-axis, and then decreases slightly until asymptotically approaching the cylinder/fiber limit, *i.e.* $\alpha \rightarrow \infty$. As represented by the dashed line in Figure 2.9, no physically relevant solutions are obtained for $\alpha > 7.9$, because the discharge process stops when the concentration on the particle surface reaches stoichiometric maximum, before the maximum stress actually

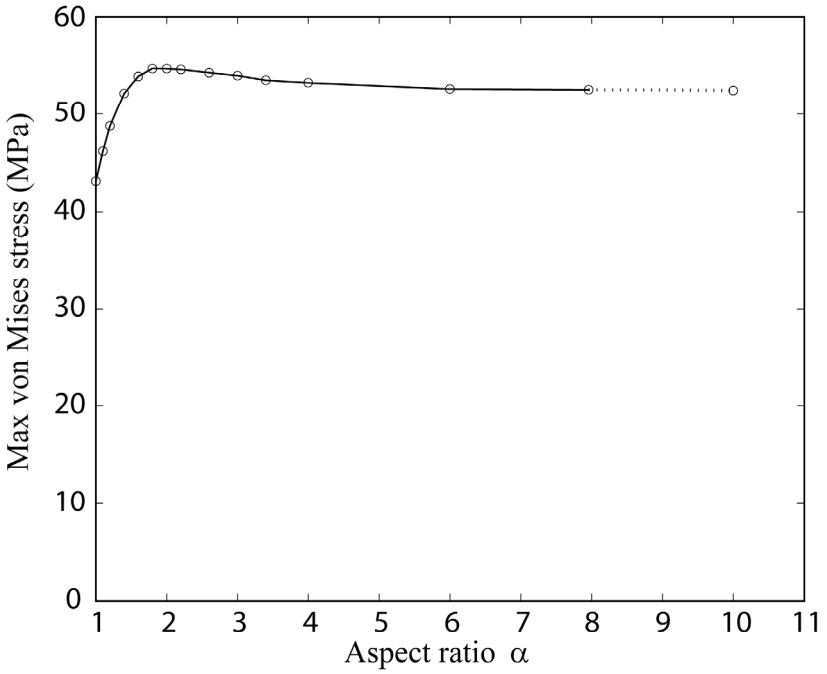

Figure 2.9: The effect of aspect ratio, for fixed shorter semi axes.

reaches the peak value. To quantitatively illustrate this point, for an ellipsoid with aspect ratio 10, the stress reaches its peak value at t = 721s. However, the simulation should terminate at t = 617.5s, when the surface concentration already reaches stoichiometric maximum. The maximum stress at t = 721s is 52.47MPa, and the stress at t = 617.5s is 52.26MPa. Therefore, the stress when the process is terminated, is only slightly smaller than the peak value.

4. CONCLUSION

Intercalation-induced stresses during the discharge process were simulated in this study using a stress-diffusion coupling model. Intercalation-induced stresses were simulated by analogy to thermal stress. Simulations of spherical particles show that larger particle sizes and larger discharge current densities give larger intercalation-induced stresses. Furthermore, internal stress gradients significantly enhance diffusion. Simulation results for ellipsoidal particles show that large aspect ratios are preferred, to reduce the intercalation-induced stresses. In total, these results suggest that it is desirable to synthesize electrode particles with smaller sizes and larger aspect ratios, to reduce intercalation-induced stress during cycling of lithium-ion batteries.

BIBLIOGRAPHY

1. H. Wang, Y.-I Jang, B. Huang, D. R. Sadoway, and Y.-M. Chiang, TEM Study of Electrochemical Cycling-Induced Damage and Disorder in $LiCoO_2$ Cathodes for Rechargeable Lithium Batteries, *Journal of the Electrochemical Society*, 146 (2), 473-480 (1999).

2. M.-R. Lim, W.-I. Cho, and K.-B. Kim, Preparation and characterization of gold-codeposited LiMn2O4 electrodes, Journal of Power Sources, 92, 168-176 (2001).

3. D. Wang, X. Wu, Z. Wang, and L. Chen, Cracking Causing Cyclic Instability of $LiFePO_4$ Cathode Material, *Journal of Power Sources,* 140, 125–128 (2005).

4. W. I. F. David, M. M. Thackeray, L. A. de Picciotto, and J. B. Goodenough, Structure Refinement of the Spinel-Related Phases $Li_2Mn_2O_4$ And $Li_{0.2}Mn_2O_4$, *Journal of Solid State Chemistry*, 67 (2), 316-323 (1987).

5. J. Christensen and J. Newman, A Mathematical Model of Stress Generation and Fracture in Lithium Manganese oxide, *Journal of the Electrochemical Society*, 153 (6), A1019-A1030 (2006).

6. Y.-B. Yi, C.-W. Wang, and A. M. Sastry, Compression of Packed Particulate Systems: Simulation and Experiments in Graphite Li-ion Anodes, *Journal of Engineering Materials and Technology*, vol. 128, 73-80 (2006).

7. S. Pyun, J. Go, and T. Jang, An Investigation of Intercalation-Induced Stresses Generated During Lithium Transport Through Li_{1-} CoO_2 Film Electrode Using a Laser Beam Deflection Method, *Electrochimica Acta,* 49 4477–4486 (2004).

8. Y. Kim, S. Pyun, and J. Go, An Investigation of Intercalation-Induced Stresses Generated During Lithium Transport Through So-Gel Derived $Li_xMn_2O_4$ Film Electrode Using a Laser Beam Deflection Method*, Electrochimica Acta,* 51, 441–449 (2005).

9. A. K. Padhi, K. S. Nanjundaswamy, and J. B. Goodenough, Phospho-olivines as Positive-Electrode Materials for Rechargeable Lithium Batteries, *Journal of the Electrochemical Society,* 144 (4), 1188-1194 (1997).

10. J. Christensen and J. Newman, Stress Generation and Fracture in Lithium Insertion Materials, *Journal of Solid State Electrochemistry*, 10 (5), 293-319 (2006).

11. S. Prussin, Generation and Distribution of Dislocations by Solute Diffusion, *Journal of Applied Physics*, 32(10), 1876-1881 (1961).

12. J. C. M. Li, Physical Chemistry of Some Microstructural Phenomena, *Metallurgical Transactions A*, 9A, 1353-1380 (1978).

13. F. Yang, Interaction between Diffusion and Chemical Stresses, *Materials Science and Engineering A*, 409, 153–159 (2005).

14. M. Doyle, J. Newman, and A. S. Gozdz, C. M. Schmutz, and J.-M. Tarascon, Comparison of Modeling Predictions with experimental Data from Plastic Lithium Ion Cells, *Journal of the Electrochemical Society*, 143(6), 1890-1903 (1996).

15. R. Darling and J. Newman, Modeling a Porous Intercalation Electrode with Two Characteristic Particle Sizes, *Journal of the Electrochemical Society*, 144(12), 4201-4208 (1997).

16. P. Arora, M. Doyle, A. S. Gozdz, R. E. White, and J. Newman, Comparison between Computer Simulations and Experimental Data for High-Rate Discharges of Plastic Lithium-Ion Batteries, *Journal of Power Sources,* 88, 219–231 (2000).

17. E. Deiss, D. Haringer, P. Novak, and O. Haas, Modeling of The Charge–Discharge Dynamics of Lithium Manganese Oxide Electrodes for Lithium-Ion Batteries, *Electrochimica Acta*, 46, 4185–4196 (2001).

18. R. Darling and J. Newman, Modeling Side Reactions in Composite $LiMn_2O_4$ Electrode, *Journal of the Electrochemical Society*, 145(3), 990-998 (1998).

19. C. Y. Ouyang, S. Q. Shi, Z. X. Wang, H. Li, X. J. Huang and L. Q. Chen, Ab Initio Molecular-Dynamics Studies on $Li_xMn_2O_4$ as Cathode Material For Lithium Secondary Batteries, *Europhysics Letters*, 67 (1), 28–34 (2004).

20. B. Ammundsen, J Roziere, and M. S. Islam, Atomistic Simulation Studies of Lithium and Proton Insertion in Spinel Lithium Manganates, *The Journal of Physical Chemistry. B* 101, 8156-8163 (1997).

21. S. P. Timoshenko and J. N. Goodier, *Theory of Elasticity*, McGraw-Hill, New York, (1970).

22. N. Noda, R. B. Hetnarski, and Y. Tanigawa, *Thermal Stresses* (second edition), Taylor & Francis, New York (2003).

23. W. R. McKinnon and R. R. Haering, Physical Mechanisms of Intercalation. In *Modern Aspects of Electrochemistry*, No. 15, edited by Ralph E. White et al. Plenum Press, New York (1983).

24. W. L. Wang, S. Lee, and J. R. Chen, Effect Of Chemical Stress On Diffusion in a Hollow Cylinder, *Journal of Applied Physics*, 91(12), 9584-9590 (2002).

25. A. Paolone, R. Cantelli, G. Rousse, and C. Masquelier, The Charge Order Transition and Elastic/Anelastic Properties of $LiMn_2O_4$, *Journal of Physics: Condensed Matter*, 15, 457-465 (2003).

CHAPTER III

SURROGATE-BASED ANALYSIS OF STRESS AND HEAT GENERATION WITHIN SINGLE CATHODE PARTICLES UNDER POTENTIODYNAMIC CONTROL*

1. INTRODUCTION

Excessive heat generation in Li batteries, resulting in thermal runaway, results in complete cell failure accompanied by violent venting and rupture, along with ignition of battery active materials [1, 2, 3, 4]. Stress-induced fracture also putatively degrades performance in these cells, as evidenced by observation of fractured surfaces in *post mortem* analysis of batteries [5, 6, 7]. Stress generation results from lithium ion extraction from the cathode (deintercalation), transport across the electrolyte and insertion into the anode (intercalation), and the reverse reaction [8]. Intercalation-induced stress varies cyclically, and thus damage aggregates with usage [5]. Particle-scale fracture of active materials results in performance degradation of batteries due to the loss of electrical contact and subsequent increase in the surface area subjected to side reactions [9]. These phenomena, heat and stress generation, undoubtedly amplify one another, and both phenomena are governed by cell kinetics. Inclusion of heat generation, mechanical

* The material in this chapter is a published paper: X. Zhang, A. M. Sastry and W. Shyy, Intercalation-induced Stress and Heat Generation within Single Lithium-Ion Battery Cathode Particles, *Journal of the Electrochemical Society,* 155(7), A542-A552 (2008).

stresses, and chemical kinetics in models at critical scales, i.e. particle scales, appears necessary, and progress in each is discussed in order.

It is important to distinguish between heat transfer and heat generation analyses in battery materials. We use “heat generation” to refer to the sources of heat in the cell; “heat transfer”, by contrast, refers to the resulting distribution of temperature. Though the sources of heat generation may be readily determined, solution for the distribution of temperature requires even more detailed understanding of both geometry and materials properties, as will be discussed later. Heat transfer analyses of Lithium-ion batteries have stemmed from work on full cells [10]. This classic work [10] was later extended to consider the effect of lithium concentration in intercalation compounds [1]. Foci of subsequent studies have mainly been on improved modeling of heat transfer, rather than refinement of geometric models to the particle scale. A three-dimensional (3D) model was been developed, considering anisotropic conductivity, to simulate the temperature distribution inside lithium polymer batteries under galvanostatic discharge for a dynamic power profile [11]. Later, a layerwise 3D model (assuming different conductivities for each homogeneous layer), was derived [12], in which radiation and convection were considered.

Thus, progress to date in heat transfer modeling has been restricted to consideration of continuum layers, though modeling at the particle scale appears necessary at this time, given our ability to select particle geometry within electrodes. Meanwhile, models have appeared in intercalation-induced stress which do address the particle scale, e.g. a one-dimensional model to estimate stress generation within spherical electrode particles [13] and a two-dimensional model to predict electrochemically

induced stresses [14]. Neither, however, has considered complex particle shapes or the effect of layerwise thickness on critical percolation limits [15]. In more recent work [16], a three-dimensional model based on a thermal stress analogy has been used to simulate the intercalation-induced stress inside cathode particles, but without consideration of electrochemical kinetics.

In order to fully and predictively link thermal and stress-induced failures, kinetic effects must also be understood, in tandem with detailed models of electrode architecture, in three dimensions, and for complex particle shape. Though it has been established that microscopic features of structures in batteries, including particle shape and size distributions, are important factors in battery performance [17], models have not been reported that incorporate electrochemical kinetics. Thus, in the present work, we model a $LiMn_2O_4$ cathode particle under potentiodynamic control, with linearly variable applied potential to the particle [18,19]. The cathode particle was assumed to be homogeneous. We had the following specific objectives:

1) To develop and numerically implement particle scale models to simulate intercalation-induced stress and heat generation, and to interrogate the interactions among intercalation, stress and heat generation, for spherical particles;

2) To understand, using surrogate-based analysis, how stress and heat generation depend upon the ratio of axial lengths for ellipsoidal cathode particles, and the operating conditions (discharge time).

Our general methodology comprised two sequential efforts. First, we developed a model that physically links intercalation-induced stress and thermal stress, following prior work [16]. Three distinct sources of heat generation were considered, namely, heat

of mixing, entropic heat, and resistive heating [1]. Though heat generation at this scale is different, we do not at present have sufficient information on local heat transfer coefficients within anisotropic particles to properly model heat transfer, and thus determination of localized temperature distribution via heat transfer analysis is not attempted here. Implementation of the model requires physical parameters, including partial molar volume [16], Young's modulus [16] and the derivative of open-circuit potential (OCP) over temperature [20].

The second effort, in surrogate modeling, comprised use of surrogate models to analyze relationships among stress and heat generation, and ellipsoidal particle morphology and operating conditions. We first conducted simulations on selected training points in critical regions, using the models developed to obtain the stress and heat generation. The simulation results were then approximated by surrogate models which were used, after validation, for further analysis of stress and heat generation for different particle geometries and cycling rates.

2. ELECTROCHEMICAL, MECHANICAL AND THERMAL MODELING

In lithium-ion batteries, actual cathode particle morphology varies with synthesis methods [21, 22, 23, 24]. Primary particles, made of crystalline grains, are agglomerated using polymeric binders (e.g. poly (vinylidene fluoride) (PVdF) [2, 25]) and conductive additives such as carbon black [25, 26], nonaqueous ultrafine carbon suspensions [27] and graphite [28, 29] are incorporated to form secondary particles. Typical cathode compositions and particle sizes are shown in Table 3.1 [Ref. 28, 25, 26, 22, 30, 31]. Sizes range from 0.3 to 4 μm for primary particles, and 11 to 60 μm for secondary particles.

active material	binder	additives	Ref.
$LiFePO_4$ 76-88 wt.%	PVdF 12 wt.%	carbon black 0-10 wt.% graphite 0-6 wt.%	28
$LiMn_2O_4$ 81.5 wt.%	PVdF 10 wt.%	carbon black 8.5wt.%	25
$LiMn_2O_4$ 80 wt.%	EPDM (ethylene propylene diene terpolymer) 5 wt. %	carbon black 15 wt.%	26

active material	synthesis method	Sizes	Ref.
$LiMn_2O_4$	calcination from Mn_3O_4 and Li_2CO_3	crystalline grain: ca. nanometers primary particle: ca. 3-4 μm	22
$Li[Mn_{1/3}Ni_{1/3}Co_{1/3}]O_2$	carbonate co-precipitation method at 950° C	primary particle: ca. 1 μm secondary particle: ca. 11 μm	30
$LiFePO_4$	microwave processing	primary particle: ca. 0.3 μm secondary particle: ca. 20-60 μm	31

Table 3.1: Representative cathode compositions and particle sizes.

Modeling of these aggregates at the scale of single crystals requires molecular or atomistic simulations. Thus, we restrict our considerations in the present study to a pure active material ($LiMn_2O_4$) without inclusions. Our model cathodes particles are homogeneous, isotropic single-phase ellipsoidal particles (prolate spheroids) or spherical particles. The stress localization due to interaction between the crystalline grains is not considered in stress generation simulations, and the temperature inside a particle is assumed to be uniform in heat generation simulations.

Determination of intercalation-induced stress and heat generation first requires mapping of concentration distribution and current density. Concentrations are obtained by solving the diffusion equation with appropriate boundary conditions for each case (see section 2.1.1). To model the intercalation-induced stress, a constitutive equation is used to relate intercalation-induced strain. A heat generation model developed for a whole cell [1] is used here, because our simulations rely on the assumption that the cathode particle behaves as one electrode of a whole cell, incorporating experimental parameters from microelectrode studies [18], wherein a single cathode electrode and the counter electrode (lithium foil) comprise the electrochemical cell.

2.1 Model of Intercalation

An intercalation process can ideally be modeled as a diffusion process with boundary flux determined by the electrochemical reaction rate. The model of the intercalation process presented in this section includes a Li-ion transport equation and a boundary condition determined by the electrochemical kinetics on the particle surface under potentiodynamic control.

2.1.1 Li-Ion Transport Equation

Li-ion diffusion is driven by the chemical potential gradient. For a given concentration and stress gradients, the diffusion flux is given by [16]

$$\mathbf{J} = -D\left(\nabla c - \frac{\Omega c}{RT}\nabla \sigma_h\right), \tag{1}$$

where c is the concentration of Li-ion, σ_h is the hydrostatic stress, defined as $\sigma_h = (\sigma_{11} + \sigma_{22} + \sigma_{33})/3$ (where σ_{ij} is the elements in stress tensor), D is the diffusion coefficient, R is the general gas constant and T is temperature. With substitution of Equation (1) into the mass conservation equation, we obtain the species transport equation as follows [16],

$$\frac{\partial c}{\partial t} + \nabla \cdot \left[-D\left(\nabla c - \frac{\Omega c}{RT}\nabla \sigma_h\right)\right] = 0 . \tag{2}$$

The boundary condition for this equation is that the flux on the particle surface is related to the discharge/charge current density $\mathbf{i}_n$ as

$$\mathbf{J} = -D\left(\nabla c - \frac{\Omega c}{RT}\nabla \sigma_h\right) = \frac{\mathbf{i}_n}{F}, \tag{3}$$

where F is Faraday's constant.

2.1.2 Electrochemical Kinetics under Potentiodynamic Control

The current density on the particle surface depends on the electrochemical reaction rate. The reactions at the positive electrode are

$$LiMn_2O_4 \Leftrightarrow Li_{1-x}Mn_2O_4 + xLi^+ + xe^-$$

During charge, the positive electrode is oxidized, and lithium ions are extracted from the positive electrode particle. During discharge, the positive electrode is reduced and lithium

ions are inserted into the positive electrode particle. Chemical kinetics (reaction rate) are described by the Butler-Volmer equation [32, 33], as

$$J = \frac{i_n}{F} = \frac{i_0}{F}\left\{\exp\left[\frac{(1-\beta)F}{RT}\eta\right] - \exp\left[-\frac{\beta F}{RT}\eta\right]\right\}, \tag{4}$$

where i_0 is exchange current density, η is surface overpotential, and β is a symmetry factor which represents the fraction of the applied potential that promotes the cathodic reaction[33].

The exchange current density i_0 is given by,

$$i_0 = Fk(c_l)^{1-\beta}(c_\theta)^{1-\beta}(c_s)^{\beta}, \tag{5}$$

where c_l is the concentration of lithium ion in the electrolyte, c_s is the concentration of lithium ion on the surface of the solid electrode, c_θ is the concentration of available vacant sites on the surface ready for lithium intercalation (which is the difference between stoichiometric maximum concentration and current concentration on the surface of the electrode $c_{\max} - c_s$), and k is a reaction rate constant[32].

In Equation (4), the surface overpotential is the difference between the potential of the solid phase (compared to the electrolyte phase) V and the open circuit potential (OCP) U [32]

$$\eta = V - U \tag{6}$$

A fit of the experimental results [34] of OCP for $LiMn_2O_4$ is illustrated in Figure 3.1 (a). OCP depends upon the state of charge y, i.e., the atomic ratio of lithium in the electrode $Li_yMn_2O_4$; this is a measure of the lithium concentration in the electrode. As shown in Figure 3.1 (a), there are two plateaus in the potential distribution, resulting from the ordering of the lithium ions on one half of the tetrahedral 8a sites of $LiMn_2O_4$ [35].

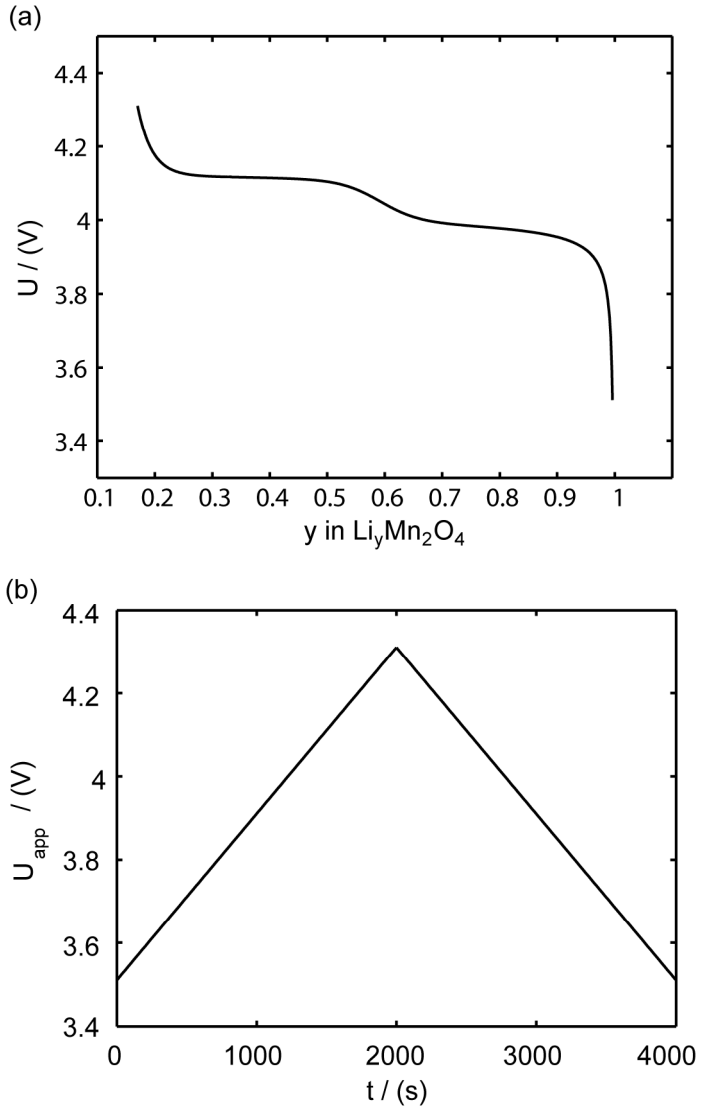

Figure 3.1: Potentials: (a) OCP of $LiMn_2O_4$ and (b) applied potential sweeping profile during one cycle.

Following the numerical study [19], the potential of the solid phase is assumed, because of the small size of particles, to be uniform within each particle, having the value of the applied potential,

$$V = U_{\text{app}}, \tag{7}$$

when under microvoltammetric study (for example, [18]). This assumption of a uniform potential distribution will be evaluated in Section 4. Under potentiodynamic control, the applied potential changes linearly with time [18, 19] for fixed potential sweep rate v. Once the applied potential reaches the upper bound, the potential sweep rate changes sign to sweep backward. Figure 3.1(b) shows an example of the potential sweep, with $v = 0.4\text{mV/s}$. Increasing applied potential, in the first half cycle, drives the charging process, while the decreasing applied potential, in the second half cycle, drives the discharging process. As the potential cycles between 3.5102V and 4.3102V [19], the electrode particle is thus charged and discharged.

For this applied potential stimulus, the initial condition for the species transport equation (Equation (2)) is $c|_{t=0} = c_0 = 0.996 c_{\max}$.

2.1.3 Parameters and Material Properties

A reasonable way to obtain the lithium ion concentration in the electrolyte c_l would be to solve the species transport equation in the electrolyte. However, it is assumed to be a constant value in this study following [19]. The values of parameters and material properties used in this study (unless otherwise stated) are listed in Table 3.2.

2.2 Intercalation-Induced Stress Model

The constitutive equation between stress and strain, including the effect of intercalation-induced stress by the analogy to thermal stress, is

symbol	value
β	0.5
c_l	1000 mol/m^3 [19]
c_{max}	2.37×10^4 mol/m^3[19]
k	1.9×10^{-9} m$^{5/2}$s^{-1}mol$^{-1/2}$ [19]
D	2.2×10^{-9} cm^2/s [19]
V	0.4 mV/s
r_0	5 μm

Table 3.2: Parameters and material properties for the intercalation model (where r_0 is the radius of a spherical particle).

$$\varepsilon_{ij} = \frac{1}{E}\left[(1+\nu)\sigma_{ij} - \nu\sigma_{kk}\delta_{ij}\right] + \frac{\tilde{c}\Omega}{3}\delta_{ij} \tag{8}$$

where ε_{ij} are strain components, σ_{ij} are stress components, E is Young's modulus, ν is Poisson's ratio, $\tilde{c} = c - c_0$ is the concentration change of the diffusion species (lithium ion) from the original (stress-free) value, and Ω is the partial molar volume of lithium [16]. Stress components are subjected to the force equilibrium equation

$$\sigma_{ij,i} = 0 \quad (j = 1, 2, 3)\,. \tag{9}$$

A Young's modulus $E = 10\text{GPa}$ and a partial molar volume $\Omega = 3.497\times10^{-6}\,\text{m}^3/\text{mol}$ [16] are assumed here. Equation (2) and (8) are coupled through concentration c, and stress σ_h.

2.3 Heat Generation Model

There are four sources of heat generation inside lithium ion batteries during operation [1]

$$\dot{Q}_g = I\left(V - U^{\text{avg}}\right) + IT\frac{\partial U^{\text{avg}}}{\partial T} + \sum_{\text{k}}\Delta H_{\text{k}}^{\text{avg}} r_{\text{k}} + \int\sum_{\text{j}}\sum_{\text{i}}\left(\overline{H}_{\text{ij}} - \overline{H}_{\text{ij}}^{\text{avg}}\right)\frac{\partial c_{\text{ij}}}{\partial t}\text{d}v \tag{10}$$

The first term, $I\left(V - U^{\text{avg}}\right)$, is the irreversible resistive heating, where I is the current of the cell, V is the cell potential, and U^{avg} is the volume averaged open circuit potential. Resistive heating is caused by the deviation of the cell potential from its equilibrium potential by resistance to the passage of current. The second term, $IT\,\partial U^{\text{avg}}/\partial T$, is the reversible entropic heat, where T is temperature. The third term, $\sum_{\text{k}}\Delta H_{\text{k}}^{\text{avg}} r_{\text{k}}$, is the heat change of chemical side reactions, where $\Delta H_{\text{k}}^{\text{avg}}$ is the enthalpy of reaction for chemical reaction *k*, and r_{k} is the rate of reaction *k*. The fourth term, $\int\sum_{\text{j}}\sum_{\text{i}}\left(\overline{H}_{\text{ij}} - \overline{H}_{\text{ij}}^{\text{avg}}\right)\partial c_{\text{ij}}/\partial t\,\text{d}v$, is the heat of mixing due to the generation and relaxation of concentration gradients, where c_{ij} is

the concentration of species i in phase j, $\mathrm{d}v$ is the differential volume element, and $\overline{H}_{\mathrm{ij}}$ and $\overline{H}_{\mathrm{ij}}^{\mathrm{avg}}$ are partial molar enthalpy of species i in phase j and the averaged partial molar enthalpy respectively.

The charge/discharge current I is obtained by the integration of current density i_n (determined by electrochemical kinetics as shown in Equation (4)) over the particle surface. The potential of solid electrode V equals to the applied potential, as in Equation (7). The volume averaged OCP U^{avg} is determined by using the volume averaged the state of charge and the experimental results of OCP, as shown in Figure 3.1(a). $\partial U^{\mathrm{avg}}/\partial T$ is measured concentration, and is thus dependent upon state of charge. Experimental results of $\mathrm{d}U/\mathrm{d}T$ for $LiMn_2O_4$ in [20] are used here. The experimental results of $\mathrm{d}U/\mathrm{d}T$ from [20] are fitted by a smoothing spline method (Matlab®), used commonly to characterize data with a high degree of noise [36]. Fit statistics for these data are $R^2 = 0.977$, $R_{adj}^2 = 0.967$; the fitted curve is shown in Figure 3.2(a).

The term $\sum_{\mathrm{k}} \Delta H_{\mathrm{k}}^{\mathrm{avg}} r_{\mathrm{k}}$ in Equation (10) is neglected, because of the assumption of no side reactions. The heat of mixing term is simplified as [1]

$$\dot{Q}_{\mathrm{mixing}} = \int \sum_{\mathrm{j}} \sum_{\mathrm{i}} \left(\overline{H}_{\mathrm{ij}} - \overline{H}_{\mathrm{ij}}^{\mathrm{avg}}\right) \frac{\partial c_{\mathrm{ij}}}{\partial t} \mathrm{d}v = \frac{\partial}{\partial t}\left[\frac{1}{2}\frac{\partial \overline{H}_s}{\partial c_s}\int \left(c_{\mathrm{s}} - c_{s,\infty}\right)^2 \mathrm{d}v\right] \tag{11}$$

by assuming that i) the volume change effect can be neglected such that the temporal derivative can be taken outside the integral; and ii) the particle is in contact with a thermal reservoir such that temperature is constant [1]. Equation (11) suggests that heat of mixing vanishes when the concentration gradient relaxes. In Equation (11), $\partial \overline{H}_{\mathrm{s}}/\partial c_{\mathrm{s}} = -F\,\partial U_{\mathrm{H}}/\partial c_{\mathrm{s}}$ where $U_{\mathrm{H}} = U - T\mathrm{d}U/\mathrm{d}T$ is enthalpy potential. The term $\partial \overline{H}_s/\partial c_s$ is obtained by numerical differentiation of enthalpy potential U_{H} over concentration. First,

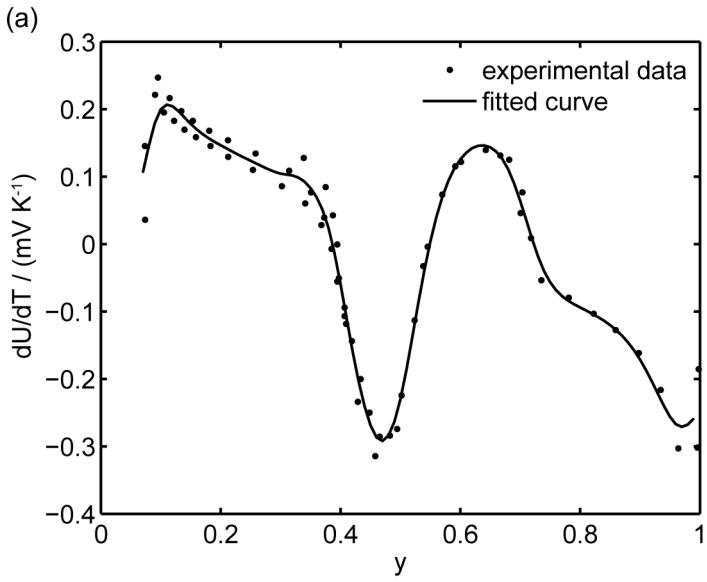

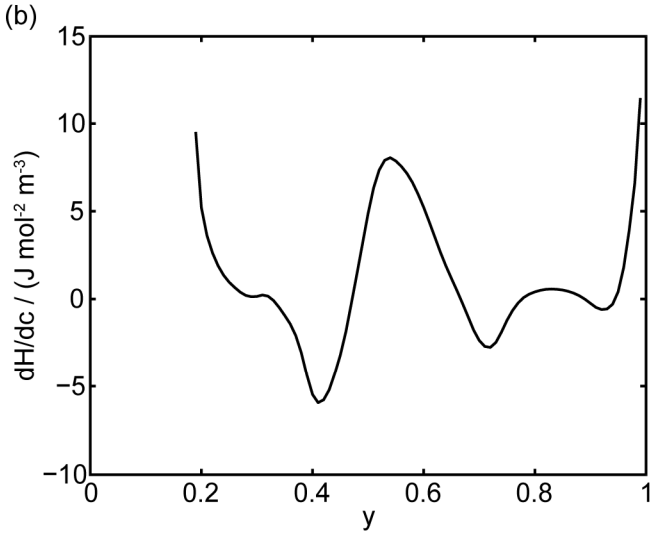

Figure 3.2: Material properties: (a) the derivative of OCP over temperature: curve fitting of the measured data from Ref. 20, and (b) the derivative of partial molar enthalpy over concentration obtained by $\partial\bar{H}/\partial c = -F\,\partial\left(U - T\mathrm{d}u/\mathrm{d}T\right)/\partial c$ based on the curve fit in (a).

U_H is calculated according to $U_H = U - T\mathrm{d}U/\mathrm{d}T$ by taking $T = 300\mathrm{K}$ and the curve fitting results in Figure 3.2(a). Then, U_H is numerically differentiated over concentration, and multiplied by $-F$, to obtain $\mathrm{d}\overline{H}/\mathrm{d}c$, plotted in Figure 3.2(b).

2.4 Spherical particle simulation results

The intercalation, stress and heat generation models described above were implemented on spherical particles with radius $r_0 = 5\mu m$ using the simulation tool COMSOL Multiphysics®. A potential sweep rate of $v = 0.4\mathrm{mV/s}$ was selected, giving a discharge/charge rate of 1.8C, falling in the range of typical rates for high-power applications of lithium-ion batteries.

2.4.1 Intercalation-Induced Stress inside Spherical Particles

The simulation results of reaction flux and stresses are shown in Figure 3.3. Figure 3.3(a) shows the diffusion flux, determined by electrochemical kinetics, on the particle surface during one cycle of voltammetry. It is positive in the first half cycle (as lithium ions are extracted from the cathode during charge) and negative in the second half cycle (as lithium ions are inserted into the cathode during discharge). This is a similar trend to those from simulations [19] and experiments [18]. The first principal stress (radial stress) is largest at the center of the particle, and the von Mises stress is largest on the particle surface. Figure 3.3(b) shows that radial stress, at the center of the particle, is negative (compressive) in the first half cycle and positive (tensile) in the second half cycle. In the first half cycle, lithium ions are extracted making the lattice contract in the particle's outer region. Therefore, the radial stress is compressive at the center of the particle. In the second half, lithium ions are inserted making the lattice expand in the

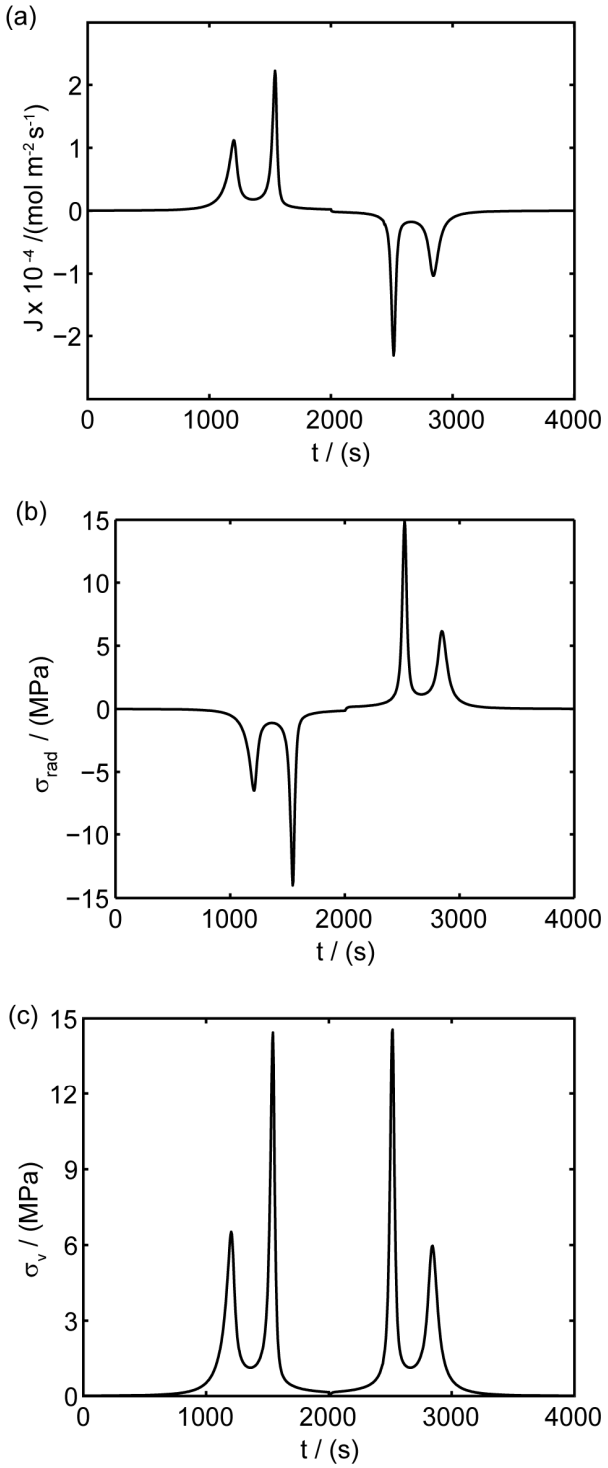

Figure 3.3: Simulation results of a spherical particle with $v = 0.4\text{mV/s}$, $r_0 = 5\mu m$: (a) diffusion flux on the particle surface, (b) radial stress at the center of the particle, and (c) von Mises stress on the particle surface..

particle's outer region. Therefore, the radial stress is tensile at the center of the particle in this half cycle.

Figure 3.3(c) shows the time history of von Mises stress on the particle surface. The flux and stress of charge and discharge half cycles are symmetric. This is because the symmetric applied potential dominates over simulation parameters for these conditions. The distribution of flux and stress may be asymmetric when other parameters, such as potential sweep rate and symmetry factor, are dominant.

Figures 3.3 (a)(b)(c) show that two peaks in species flux and stress time history arise in each half cycle. To determine the origin of these peaks, a detailed study of the first half cycle was conducted. The time histories of diffusion flux and von Mises stress on the surface in the charge half cycle are re-plotted in Figure 3.4(a) and (b). As shown in Figure 3.4(a), two peaks of surface flux occur at t=1202s and t=1541s. By the Butler-Volmer equation for electrochemical kinetics on particle surface (Equation (4)), surface flux depends on surface over-potential η and exchange current density i_0. Surface overpotential η is the difference between the applied potential and the OCP as shown in Equation (6) and (7). The applied potential increases linearly with time in the charge half cycle of the potentiodynamic process as illustrated in Figure 1(b). The open circuit potential changes with the lithium content in the electrode, as shown in Figure 1(a). During the charging process, OCP increases as lithium concentration decreases. The difference between the two increasing potentials, the surface overpotential, is shown in Figure 3.4(c). It is shown in Figure 3.4(c) that there are two peaks in the surface overpotential plot mainly due to the two plateaus in the open circuit potential shown in

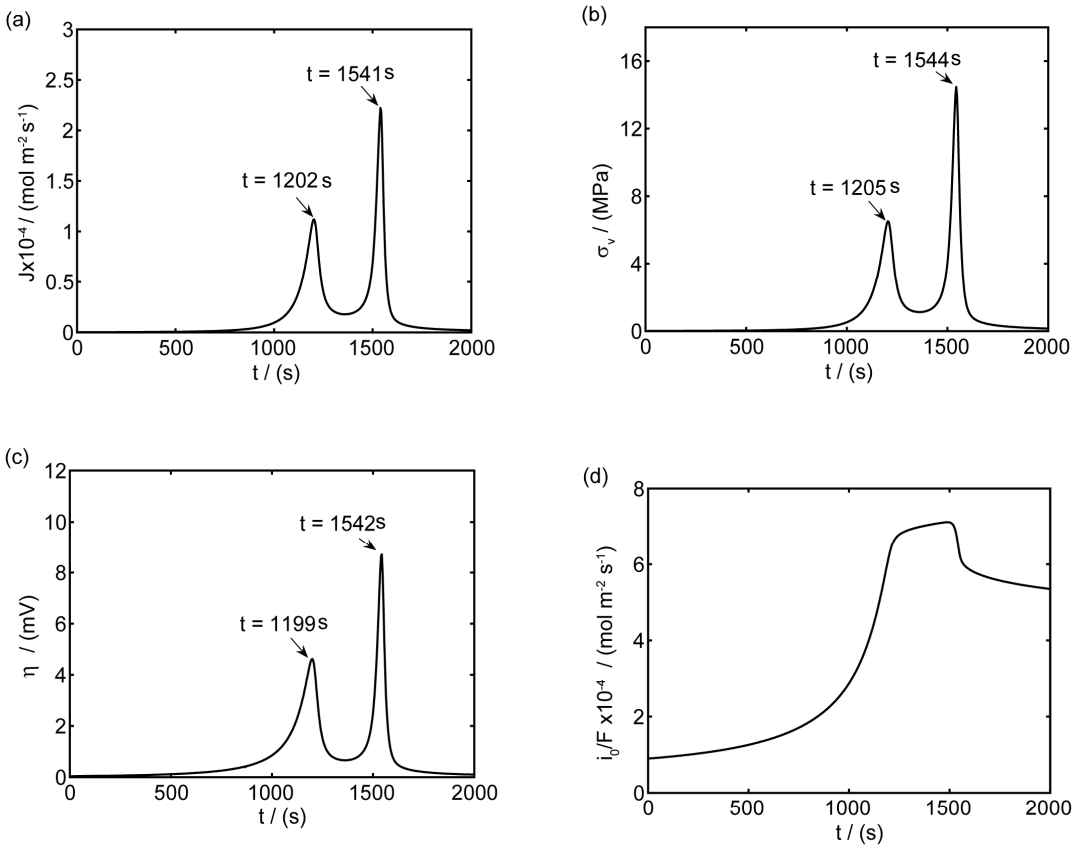

Figure 3.4: Simulation results of a spherical particle in the charge half cycle ($v = 0.4\text{mV/s}$,$r_0 = 5\mu m$): (a) reaction flux on the particle surface, (b) von Mises stress on the particle surface, (c) surface overpotential, and (d) exchange current density (divided by Faraday's constant).

Figure 3.1(a). Because surface overpotential appears in the exponential terms in Equation (4), it is the dominant factor for the resulting flux. Therefore, there are two peaks in the flux plot as shown in Figure 3.4(a). However, a closer look at the time instants for the peaks in Figure 3.4(a) and Figure 3.4(c) shows that the corresponding peaks appear at different times. This is attributable to the temporal distribution of exchange current density (as plotted in Figure 3.4(d)), because the flux is actually the product of exchange current density and the exponential terms, including surface overpotential, as shown in Equation (4). To summarize, the peaks in the flux distribution originate essentially from the two plateauss in the OCP distribution, which is an intrinsic property of the cathode material $LiMn_2O_4$, and the temporal variation of the applied potential.

To explain the peaks in the stress plot in Figure 3.4(b), we recall the expression of the von Mises stress on a spherical particle surface (von Mises stress has its maximum value on the particle surface $r = r_0$) [16]

$$\sigma_V(r=r_0) = \left|\sigma_{\text{rad}} - \sigma_{\text{tang}}\right|_{r=r_0} = \frac{\Omega E}{3(1-\nu)}\left(\frac{3}{r_0^3}\int_0^{r_0} \tilde{c} r^2 \mathrm{d}r - \tilde{c}(r=r_0)\right). \tag{12}$$

As shown in the Equation (12), the von Mises stress on the particle surface depends on the difference between the global average concentration $3\left(\int_0^{r_0} \tilde{c} r^2 \mathrm{d}r\right)/r_0^3$ and the local concentration of lithium ions. Figure 3.5 shows the distribution of concentrations at different times during charge. It may be seen that the concentration is quite uniformly distributed most of the time. At t=1205s and t=1544s, significant gradients are present in the concentration distribution (due to the two peak fluxes shown in Figure 3.4(a)), therefore we expect predominantly large stress at these times by Equation (12),

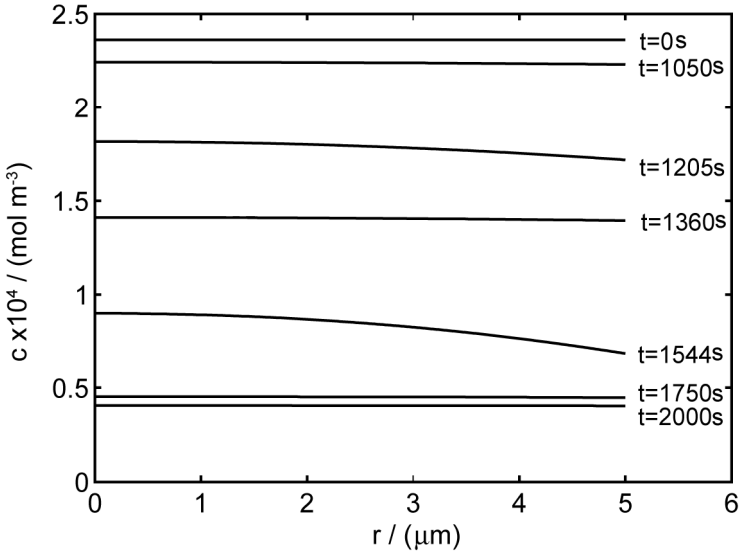

Figure 3.5: Distribution of lithium-ion concentration inside a spherical particle at different time instants during the charge half cycle.

explaining the two peaks shown in Figure 3.4(b). By comparing Figure 3.4(a) and (b), we also see that the peaks in the stress plot are a few seconds later than the corresponding peaks in the flux plot. This is because it takes time for the concentration distribution to respond to the change of the boundary flux in the diffusion process. The peaks in the radial stress plot in Figure 3.3(b) can be explained similarly, by considering that radial stress depends on the difference between the global and local average of concentrations [16]—in other words—the nonuniformity of the concentration distribution.

The above analysis shows that surface flux, concentration and stress are highly interrelated. Surface flux by electrochemical reaction and diffusion determine the concentration distribution, which in turn affects the OCP, the chemical kinetics and thus surface flux. Concentration distribution determines stress, the gradient of which in turn enhances the diffusion [16] because of the effect of stress gradient on diffusion as shown in Equation (1). The two peaks observed in the resulting flux and stress generation are attributable to the material property of $LiMn_2O_4$ (two plateaus in the OCP) and the applied potential.

2.4.2 Intercalation-Induced Stress inside Spherical Particles under a Higher Rate of Charge (20C)

A single simulation was also conducted for a spherical particle under a very high charge rate, 20C. The spherical particle radius was 5μm, and the potential sweep rate was increased to 4.4444mV/s. The time history of simulated surface reaction flux and von Mises stress on the particle surface is shown in Figure 3.6.

For this faster charge rate, the patterns of flux and stress time history in Figure 3.6 are different from those for 1.8C as shown in Figure 4 because the kinetics differs at the

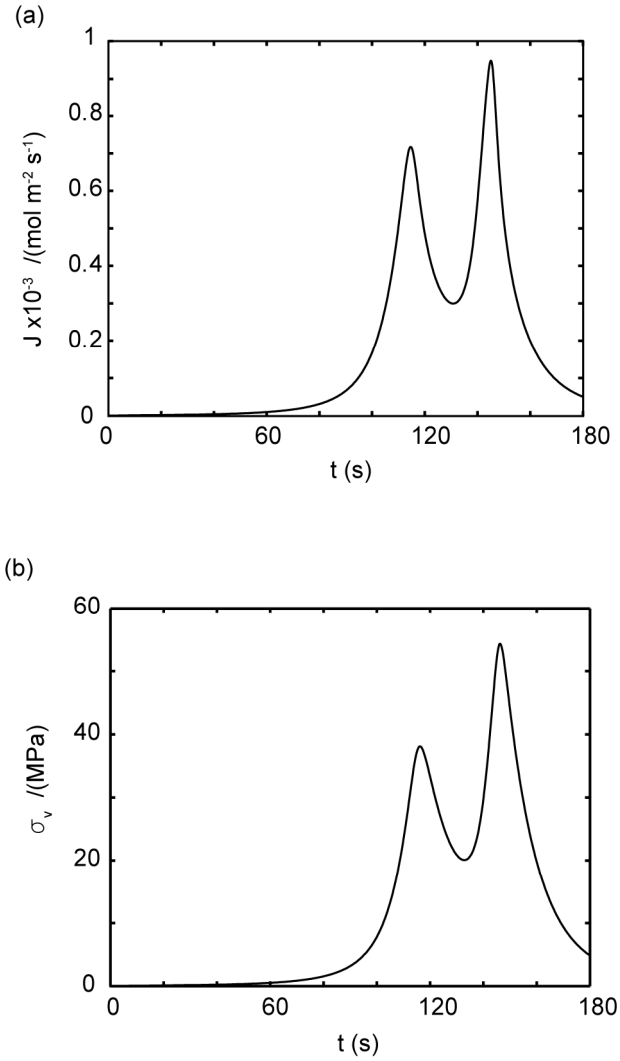

Figure 3.6: Simulation results of a spherical particle under 20C charge: (a) reaction flux on the particle surface, and (b) von Mises stress on the particle surface.

higher rate. Also, the peak value of surface reaction flux is 9.48×10^{-4} mol/m^2-s, which is about five times larger than the peak flux of 2.22×10^{-4} mol/m^2-s for 1.8C charge. Figure 3.6 also shows that the resulting stress (peak value) increases from 14.5MPa to 54.4MPa when the charge rate increases from 1.8C to 20C.

2.4.3 Heat Generation inside Spherical Particles

The time history of each heat generation term in charge half cycle is shown in the Figure 3.7. The entropic heat and heat of mixing, change signs during the charge half cycle, which is mainly attributable to the variation of material properties $\mathrm{d}U/\mathrm{d}T$ and $\mathrm{d}\overline{H}/\mathrm{d}c$ from experiment measurements.

Table 3.3 gives the time-averaged rate of each heat generation term during the charging process for two different potential sweep rates. The heat of mixing is negligible compared to resistive heat and entropic heat. Entropic heat is reversible; thus the heat generation due to this term is expected to cancel out during the charge and discharge half cycles. Therefore, the only term of interest is the resistive heat. Furthermore, resistive heat increases when the charge half cycle gets faster, which is expected because the polarization is larger for higher charge rates.

3. SURROGATE-BASED ANALYSIS OF ELLIPSOIDAL PARTICLES UNDER DIFFERENT CYCLING RATES

To understand how stress and heat generation behave with the particle geometric configuration and the operating condition, a surrogate-based analysis approach is used. Surrogate models, which are constructed using the available data generated from pre-selected designs, offer an effective way of evaluating geometrical and physical variables. The key steps of surrogate modeling include design of experiments, running numerical

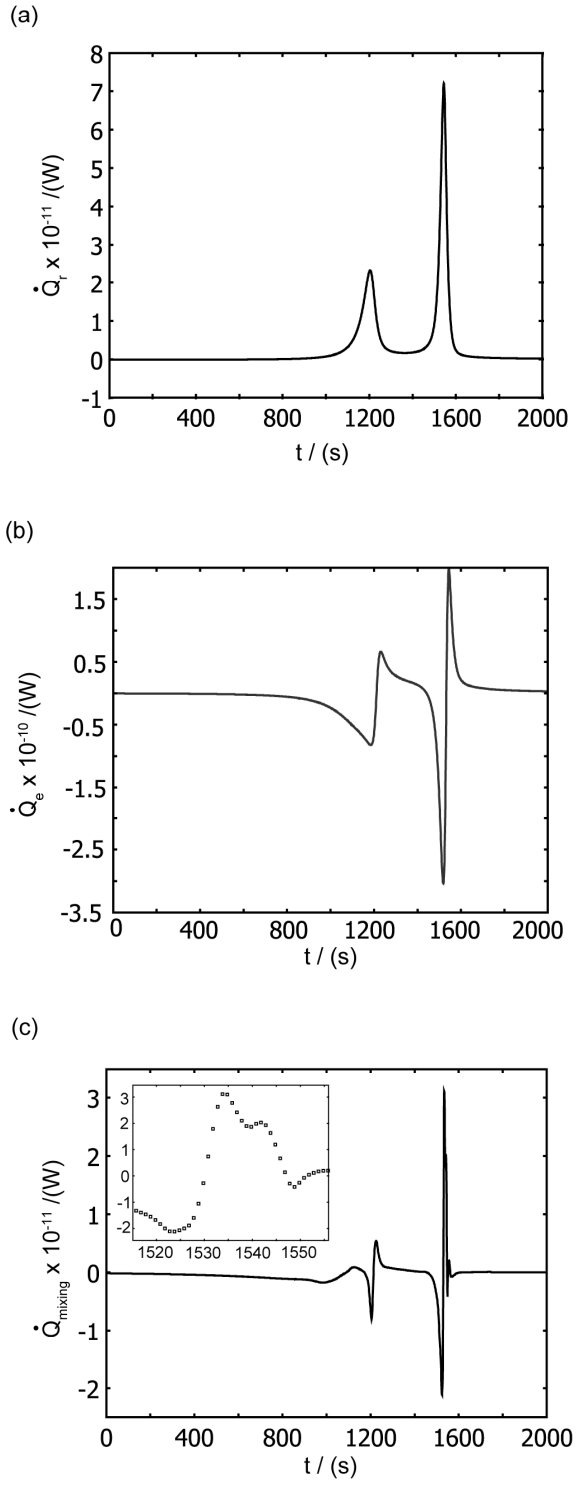

Figure 3.7: Simulation results of various heat generation sources during the charge half cycle: (a) resistive heating, (b) entropic heating, and (c) heat of mixing.

	case I	case II
potential sweep rate	0.4 mV/s	1 mV/s
charge time	2000 s	800 s
heat of mixing	-7.55×10^{-14} W	-2.31×10^{-13} W
resistive heating	2.88×10^{-12} W	1.63×10^{-11} W
entropic heat	-4.88×10^{-12} W	-1.24×10^{-11} W

Table 3.3: Averaged heat generation rates during charge process.

simulations (computer experiments), constructing surrogate models, validating and further refining, if necessary, the models [37, 38, 39].

The design of experiments is the sampling plan in the design variable space. There are several approaches available in the literature. The combination of face-centered composite design (FCCD) [40] and Latin hypercube sampling (LHS) [41] was used here. After obtaining the sampling points in the design variable space, numerical simulations (computer experiments) were run at selected training points, to obtain the value of objective variables. With simulation results for the training points, surrogate models were constructed to approximate the objective functions. Surrogate models available include polynomial regression model, krigging modeling and radial basis functions, among others [37]. The second order polynomial regression model was used in this study; the least square method was used to find the coefficients of the approximation. After constructing the response surface approximation, error estimations were necessary to validate the performance of the approximation. Common error measures used are root mean square (rms) error, prediction error sum of squares (PRESS), and (adjusted) coefficients of multiple determination R^2_{adj} [42]. The validated surrogate models were used for further analysis of the dependency between the objective functions and design variables to understand the underlying physics mechanisms.

3.1 Selection of Variables and Design of Experiments

Three design variables were selected in this study. Considering the geometric illustration of an ellipsoidal particle (prolate spheroid) shown in Figure 3.8, we set three semiaxis lengths as $c > a = b$. Two independent variables required to define the geometry, equivalent particle radius $\overline{R} = \left(a^2 c\right)^{1/3}$ and aspect ratio $\alpha = c/a$, were selected as design

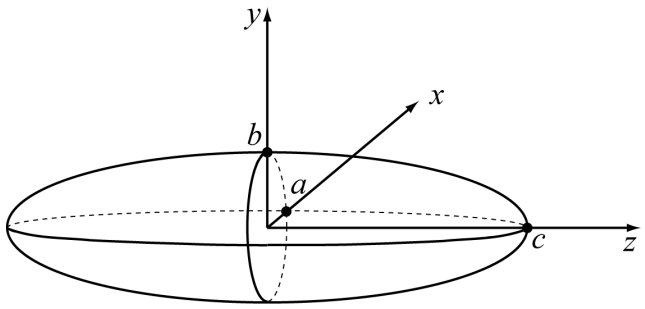

Figure 3.8: Geometric illustration of an ellipsoidal particle.

name	expression	range
equivalent radius	$\bar{R} = \left(a^2 c\right)^{1/3}$	$4\mu\text{m} < \bar{R} < 6\mu\text{m}$
aspect ratio	$\alpha = c/a$	$1 < \alpha < 3$
potential sweep rate	v	$0.6\text{mV/s} < v < 0.8\text{mV/s}$

Table 3.4: Design variables and design space.

variables. The third design variable was potential sweep rate v. The range of the three design variables is shown in Table 3.4. A spherical particle of radius $r_0 = 5\mu m$ was used in the experimental work of Uchida et al. [18], thus the range of equivalent particle radii was selected as a 20% perturbation around 5μm. The aspect ratio range was selected based on the experimental observation of particle morphology by scanning electron microscope (SEM). The selected potential sweep rate gave a charge/discharge rate of 2.7C to 3.6C, which falls into the range of high-power applications.

The two objective functions chosen in this study were the peak value of the cyclically varying maximum von Mises stress $\sigma_{\max}$ (in megapascal and the time-averaged resistive heat generation rate $\dot{Q}_{r,\text{avg}}$ (in picowatts). In fatigue analysis, mean value of the cyclically varying stress affects the number of cycles allowed before failure as well as the peak value [43]. In this study, numerical simulation results showed that mean stress and the peak value of the stress are highly correlated (the correlation coefficient is 0.992). Therefore, only the peak value of stress is considered as an objective function. Time-averaged resistive heat generation rate is the total resistive heat generation normalized by the overall charge half cycle time.

For the design of experiments, 20 points in total were selected in the design space defined in Table 3.4. Among these points, 15 of them are from FCCD and the remaining 5 points are from LHS. Numerical simulations were conducted on these 20 training points using the models described in the previous sections to obtain intercalation-induced stress and resistive heat.

3.2 Model Construction and Validation

To construct the surrogate model using the obtained simulation results on the 20 training points, a second order polynomial response surface was selected. The coefficients in the approximation were determined by minimizing the error of approximation at the training points in the least square sense. The approximations obtained for the two objective functions were

$$\sigma_{\max} = -18.0 + 4.81\overline{R} + 8.10\alpha + 4.13v - 0.065\overline{R}^2 - 0.275\overline{R}\alpha + 2.55\overline{R}v - 2.00\alpha^2 - 0.079\alpha v - 1.05v^2 \quad (13)$$

$$\dot{Q}_{r,\text{avg}} = 72.4 - 25.9\overline{R} + 5.29\alpha - 86.0v + 2.17\overline{R}^2 - 0.816\overline{R}\alpha + 18.1\overline{R}v - 0.018\alpha^2 - 3.09\alpha v + 18.9v^2 \quad (14)$$

The statistics of the response surface approximation are listed in Table 3.5. RMS error is the difference between the prediction and simulation values on the training points. Adjusted coefficients of multiple determination R^2_{adj} are a measure of how well the approximation explains the variation of the objective functions caused by design variables. For a good fit, this coefficient should be close to one. PRESS is a cross-validation error. It is the summation of squares of all PRESS residues, each of which is calculated as the difference between the simulation by computer experiments and the prediction by the surrogate models constructed from the remaining sampling points excluding the point of interest itself [42]. As shown in Table 3.5, the normalized RMS error and PRESS are small, and the adjusted coefficients of multiple determination R^2_{adj} is very close to one. Therefore, the surrogate models constructed approximate the objective functions quite well.

To further validate the accuracy of constructed surrogate models, they were tested by comparing the predicted and simulated values from computer experiments on four

statistic name	stress	resistive heat
# of training points	20	20
minimum of data	11.7	1.96
mean of data	19.9	8.86
maximum of data	27.5	23.6
RMS error (normalized *)	0.0368	0.0168
R^2_{adj}	0.984	0.996
PRESS (normalized *)	0.0498	0.0356

* Note: RMS error and PRESS are both normalized by the range of the objective functions, that is, the difference between the maximum and the minimum of data.

Table 3.5: Evaluation of the response surface approximations.

testing points different from the training points. The results of the comparison show that the differences between the prediction and simulation results are within 6%.

To summarize, the surrogate models constructed (13) and (14) not only explain the variation of objective functions resulting from design variables well, but also give a good prediction of the objective functions. Therefore, the obtained response surface approximations can be used with confidence to analyze dependencies among objective functions and design variables.

3.3 Analysis Based on Obtained Surrogate Models

These dependencies are shown in Figure 3.9. We note that 1) intercalation-induced stress $\sigma_{\max}$ increases with both increasing equivalent radius $\bar{R}$ and increasing potential sweep rate v; however, intercalation-induced stress $\sigma_{\max}$ increases first and then decreases as aspect ratio α increases; and 2) time-averaged resistive heat generation rate $\dot{Q}_{r,\text{avg}}$ increases with both increasing equivalent radius $\bar{R}$ and increasing potential sweep rate v; however, time-averaged resistive heat generation rate $\dot{Q}_{r,\text{avg}}$ decreases as aspect ratio α increases. This surrogate-based analysis suggests that ellipsoidal particles with larger aspect ratios are superior to spherical particles for improving battery performance when stress and heat generation are the only limiting factors considered.

As pointed out earlier, intercalation-induced stress depends on the concentration distribution. When equivalent radius $\bar{R}$ increases, the range of concentration distributions within the particle becomes wider, because of the longer diffusion path. Therefore, the intercalation-induced stress increases as equivalent radius $\bar{R}$ increases. When potential sweep rate v increases, the electrochemical reaction rate driven by the surface

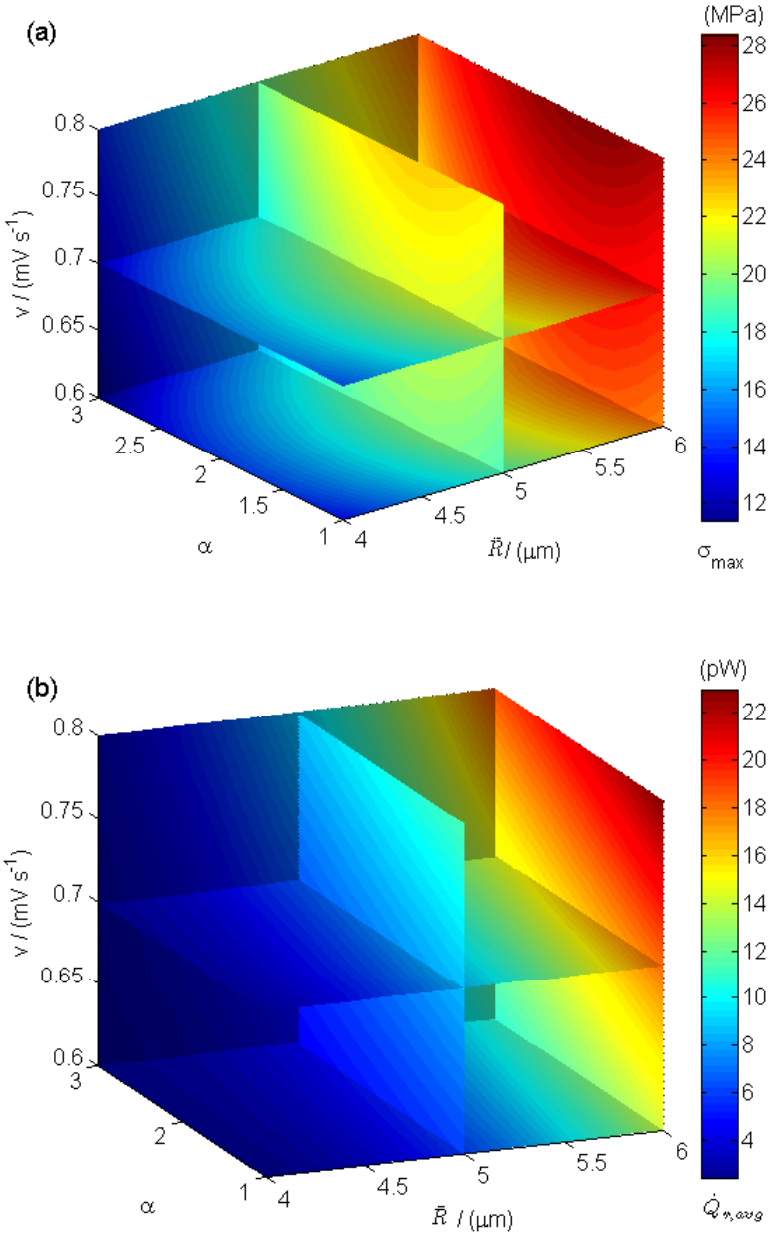

Figure 3.9: The dependency between objective functions and design variables (a) maximum von Mises stress (in megapascal), (b) time-averaged resistive heat rate (in picowatts).

overpotential becomes faster, which results in large flux on the particle surface boundary. Therefore, one expects a larger concentration gradient inside the particle and larger intercalation-induced stress for larger potential sweep rate v. When aspect ratio α increases, there are two competing effects: the shorter semi-axis lengths a and b decrease and the longer semi-axis length c increases. The increase of the longer semi-axis leads to stress increase, and the decrease of the shorter semi-axis leads to stress decrease. Therefore, intercalation-induced stress increases first and then decreases as aspect ratio increases.

As shown in Equation (10), resistive heat rate is the product of current and overpotential (or polarization), and the time-averaged heat generation rate over the charge half cycle is

$$\dot{Q}_{r,\text{avg}} = \frac{1}{\Delta t_{\text{charge}}} \int I\left(V - U^{\text{avg}}\right) \mathrm{d}t \,. \tag{15}$$

As the equivalent radius increases, the surface area subjected to reaction is larger, which results in larger total current. Therefore, the averaged resistive heat generation rate increases. When the potential sweep rate increases, the electrochemical reaction on the surface is driven faster, which results in larger polarization, or overpotential. Therefore, the averaged resistive heat generation rate increases even though the time duration for the charge half cycle decreases. When the aspect ratio increases, the shorter semiaxis length decreases; this results in the decrease of average polarization or overpotential due to the shorter average diffusion path. Therefore, the averaged resistive heat generation rate decreases.

Global sensitivity analysis, which is often used to study the importance of design variables, was conducted to quantify the variation of the objective functions caused by

three design variables. The importance of design variables is presented by main factor and total effect indices [37]. Main factor is the fraction of the total variance of the objective function contributed by a particular variable in isolation, while the total effect includes contribution of all partial variances in which the variable of interest involved (basically by considering those interaction terms in the response surface approximation as shown in Equation (13) and (14)). The calculated total effect results are listed in Table 3.6. It can be seen that, for the design space range selected in Table 3.4, equivalent particle radius contributes the most to the variation of the two objective functions, intercalation-induced stress and resistive heat (85 and 87% of total variation respectively).

4. ASSUMPTION OF A UNIFORM ELECTRIC POTENTIAL

In the current model, electric potential inside the particle is assumed to be uniform, though potential varies in a battery electrode particle due to electric current flow within the particle. From a modeling standpoint, the most important value to accurately estimate is the electric potential on the particle surface, because this value determines the electrochemical reaction rate via the Butler-Volmer equation. The simulation presented in this study follows an earlier microelectrode experimental work where an electric potential is applied through a filament in contact with a cathode particle [18].

The potential distribution inside the particle could have been obtained numerically in our model by solving Poisson's equation. Experimentally [18], potential was measured at a single point, but it is impractical to set up a similar boundary condition for the electric potential numerically, because the applied potential is applied, ideally, at a single point. To evaluate the significance of potential variation on the particle surface to the

variable	for stress	for resistive heat
equivalent radius $\bar{R}$	0.851	0.873
aspect ratio α	0.082	0.023
potential sweep rate v	0.069	0.128

Table 3.6: Global sensitivity indices (total effect) for stress and resistive heat.

intercalation process, we use a prescribed potential variation in the numerical simulation to investigate the significance of this variation.

The resistivity of $LiMn_2O_4$ is about $1.5\times10^4\Omega$-cm [44]. The peak value measured current drawn from a 5μm (radius) particle under 4C discharge is on the order of 2nA [18]. The electric potential variation inside a 5μm (radius) particle under 4C discharge is on the order of 10mV, which is comparable to the surface overpotential obtained (Figure 3.4). To evaluate the importance of this potential variation, we apply a prescribed electric potential to a 5μm (radius) particle. Figure 3.10 (a) shows the distribution of the potential at time instant t=1534s. The prescribed spatial potential variation follows the equation $0.005(x^2+y^2+(z-r_0)^2)/(2r_0)^2$, where r_0 (in microns) is the radius of the particle. Potentiodynamic control in this case has applied potential varying linearly with time.

Figure 3.10 (b) (c) (d) shows the simulation results of this case. The time history of von Mises stress (Figure 3.10 (b)) follows the same trend, when the potential is assumed to be uniform. The variation of electric potential results in a non-uniform distribution of surface overpotential and surface reaction flux, which, in turn, results in a shift in the concentration distribution as shown in Figure 3.10 (c). However, the distribution pattern of von Mises stress is not altered; it remains axisymmetric as shown in Figure 3.10 (d). The time instant of t=1534s is selected to present the results because this is the instant when von Mises stress reaches the temporal maximum value.

To sum up, although the variation of electric potential shifts the concentration distribution, it does not change von Mises stress distribution pattern. For simplicity and due to lack of more detailed empirical guideline, we assume that the electric potential is uniform inside the particle. Our finding does offer scientific insight into the interplay

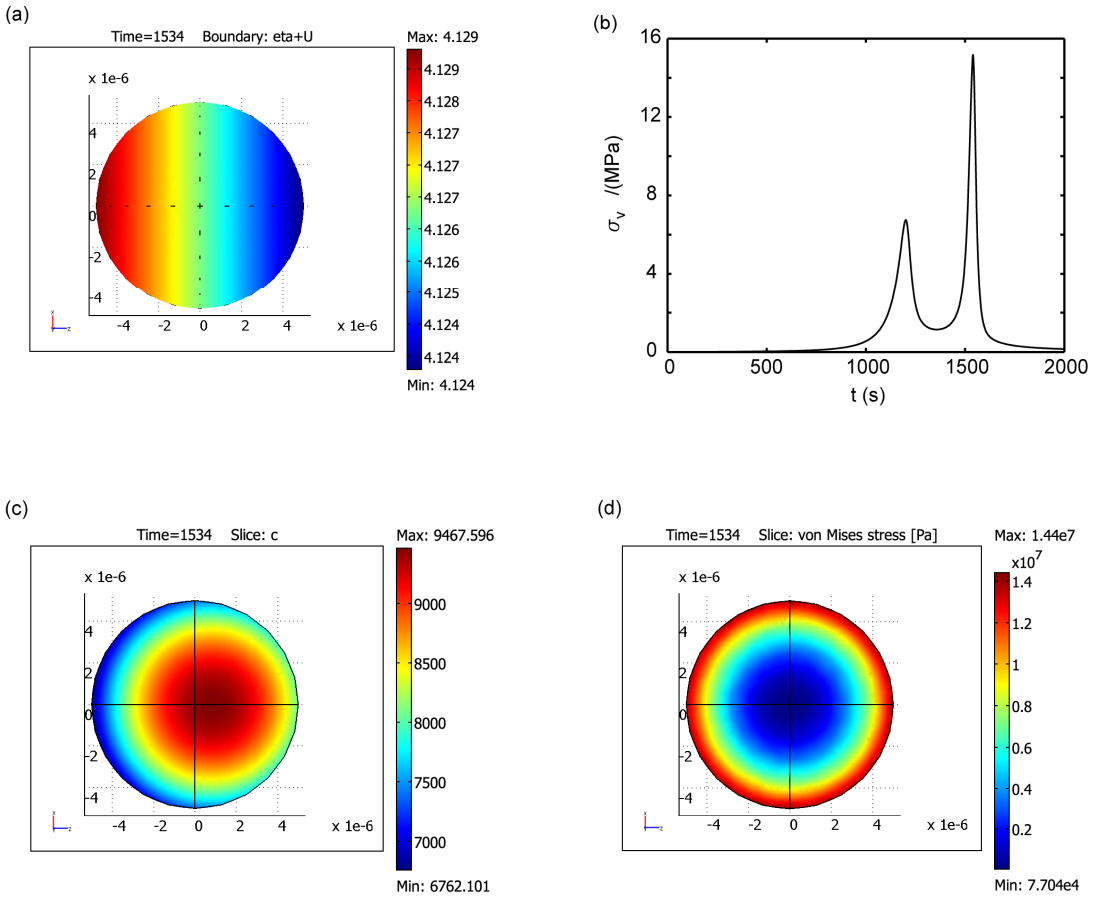

Figure 3.10: Simulation with a predescribed potential variation: (a) potential variation on particle surface at t=1534s, (b) time history of von Mises stress on particle surface, (c) concentration distribution inside the particle at t=1534s, and (d) von Mises stress distribution inside the particle at t=1534s.

between stress and heat generation, particle geometry (aspect ratio and equivalent size), and potential sweep rate.

5. CONCLUSIONS

Intercalation-induced stress and heat generation inside Li-ion battery cathode ($LiMn_2O_4$) particles under potentiodynamic control were simulated. It was found that Li-ion concentration, surface flux, and intercalation-induced stress are highly correlated through the diffusion process, electrochemical kinetics and the intercalation-induced lattice expansion. The two peaks observed in the flux and stress generation plots were attributable to intrinsic material properties (two plateaus in the OCP) and the applied potential. Three major heat generation sources, resistive heating, heat of mixing and entropic heat, were analyzed. The heat of mixing was found to be negligible (two orders of magnitude smaller than the other two sources) and resistive heat was identified as the heating source of greatest importance.

The surrogate-based analysis approach was used to study the relationship among the two objective functions (intercalation-induced stress and resistive heat) and the selected design variables (particle morphology and the operating condition). It was shown that both intercalation-induced stress and time-averaged resistive heat generation rate increase with increasing equivalent particle radius and potential sweep rate; intercalation-induced stress increases first, then decreases, as the aspect ratio of an ellipsoidal particle increases, while averaged resistive heat generation rate decreases as aspect ratio increases. A sensitivity analysis was conducted to rank the importance of each design variable on the stress and heat generation. It was shown that particle equivalent radius contributes the most to both stress and heat generation for the design space range

considered in this study (85 and 87% of the total variation, respectively). The observed variation trend from this systematic numerical study may also be explained from fundamental principles: intercalation-induced stress depends on the Li-ion concentration distribution and the resistive heat depends on a combination of total charge current and polarization (overpotential). The surrogate-based analysis conducted suggests that ellipsoidal particles with larger aspect ratios are preferred over spherical particles in improving battery performance, when stress and heat generation are the only factors considered.

The proposed models in this study are only valid for purely active material ($LiMn_2O_4$) without inclusions. The obtained results are fundamental, but for homogeneous particles. The general methodology of surrogate-based analysis presented in this study is extendable to consider more variables and geometries, such as more complicated geometric representation (aggregates) and applied potential profiles controlled by more parameters, or larger scales. In the next chapter, we will extend the models, developed here at the particle scale, to the whole cell scale with a volume averaging technique [45, 46, 47] in which a multiscale modeling methodology [48] will be applied to pass the information obtained on the microscopic scale to the macroscopic scale.

BIBLIOGRAPHY

1. K. E. Thomas, and J. Newman, Thermal Modeling of Porous Insertion Electrodes, Journal of the Electrochemical Society, 150, A176-A192 (2003).
2. H. Maleki, G. Deng, A. Anani, and J. Howard, Thermal Stability Studies of Li-Ion Cells and Components, Journal of the Electrochemical Society, 146 (9) 3224-3229 (1999).
3. A. Du Pasquier, F. Disma, T. Bowmer, A.S. Gozdz, G. Amatucci, and J.-M. Tarascon, Differential Scanning Calorimetry Study of the Reactivity of Carbon Anodes in Plastic Li-Ion Batteries, Journal of Electrochemical Society 145, 472-477 (1998).
4. R. Spotnitz, and J. Franklin, Abuse Behavior of High-Power, Lithium-Ion Cells, Journal of Power Sources, 113, 81-100 (2003).
5. M.-R. Lim, W.-I. Cho, and K.-B. Kim, Preparation and characterization of gold-codeposited LiMn2O4 electrodes, Journal of Power Sources, 92, 168-176 (2001).
6. D. Wang, X. Wu, Z. Wang, and L. Chen, Cracking Causing Cyclic Instability of LiFePO4 Cathode Material, Journal of Power Sources, 140, 125-128 (2005).
7. H. Wang, Y.-I. Jang, B. Huang, D. R. Sadoway, and Y.-M. Chiang, TEM Study of Electrochemical Cycling-Induced Damage and Disorder in LiCoO2 Cathodes for Rechargeable Lithium Batteries, Journal of the Electrochemical Society, 146, 473-480 (1999).
8. Y.-M. Choi and S.-I. Pyun, Effects of Intercalation-Induced Stress on Lithium Transport through Porous LiCoO2 Electrode, Solid State Ionics, 99, 173-183 (1997).
9. K. E. Aifantis and J. P. Dempsey, Stable crack growth in nanostructured Li-batteries, Journal of Power Sources, 143, 203–211 (2005).
10. D. Bernardi, E. Pawlikowski, and J. Newman, A General Energy Balance for Battery Systems, Journal of the Electrochemical Society, 132, 5-12 (1985).
11. Y. Chen and J.W. Evans, Three-Dimensional Thermal Modeling of Lithium-Polymer Batteries under Galvanostatic Discharge and Dynamic Power Profile, Journal of the Electrochemical Society, 141, 2947-2955 (1994).
12. S. C. Chen, C. C. Wan, and Y. Y. Wang, Thermal Analysis of Lithium-Ion Batteries, Journal of Power Sources, 140, 111-124 (2005).
13. J. Christensen and J. Newman, Stress Generation and Fracture in Lithium Insertion Materials, Journal of Solid State Electrochemistry, 10, 293–319 (2006).
14. R. E. Garcia, Y.-M. Chiang, W. C. Carter, P. Limthongkul, and C. M. Bishop, Microstructural Modeling and Design of Rechargeable Lithium-Ion Batteries, Journal of the Electrochemical Society, 152, A255-A263 (2005).

15. Y.-B. Yi, C.-W. Wang, and A. M. Sastry, Two-Dimensional vs. Three-Dimensional Clustering and Percolation in Fields of Overlapping Ellipsoids Journal of the Electrochemical Society, 151, A1292-A1300 (2004).

16. X. Zhang, W. Shyy, and A. M. Sastry, Numerical Simulation of Intercalation-Induced Stress in Li-Ion Battery Electrode Particles, Journal of the Electrochemical Society, 154, A910-A916 (2007).

17. A. Guerfi, P. Charest, K. Kinoshita, M. Perrier, and K. Zaghib, Nano Electronically Conductive Titanium-Spinel as Lithium Ion Storage Negative Electrode, Journal of Power Sources, 126, 163–168 (2004).

18. I. Uchida, H. Fujiyoshi, and S. Waki, Microvoltammetric Studies on Single Particles of Battery Active Materials, Journal of Power Sources, 68, 139-144 (1997).

19. D. Zhang, B. N. Popov, and R. E. White, Modeling Lithium Intercalation of a Single Spinel Particle under Potentiodynamic Control, Journal of The Electrochemical Society, 147, 831-838 (2000).

20. K. E. Thomas, C. Bogatu, and J. Newman, Measurement of the Entropy of Reaction as a Function of State of Charge in Doped and Undoped Lithium Manganese Oxide, Journal of The Electrochemical Society, 148, A570-A575 (2001).

21. I. Taniguchi, C.K. Lim, D. Song, and M. Wakihara, Particle Morphology and Electrochemical Performances of Spinel LiMn2O4 Powders Synthesized Using Ultrasonic Spray Pyrolysis Method, Solid State Ionics, 146, 239-247 (2002).

22. X. He, J. Li, Y. Cai, C. Jiang and C. Wan, Preparation of Spherical LiMn2O4 Cathode Material for Li-ion Batteries, Materials Chemistry and Physics, 95, 105-108 (2006).

23. W. Liu, G.C. Farrington, F. Chaput, and B. Dunn, Synthesis and Electrochemical Studies of Spinel Phase LiMn2O4 Cathode Materials Prepared by the Pechini Process, Journal of the Electrochemical Society, 143, 879-884 (1996).

24. S. H. Ju, D. Y. Kim, E. B. Jo, and Y. C. Kang, LiMn2O4 Particles Prepared by Spray Pyrolysis from Spray Solution with Citric Acid and Ethylene Glycol", Journal of Materials Science, 42, 5369-5374 (2007).

25. M. G. Lazarraga, S. Mandal, J. Ibanez, J. M.Amarilla, and J. M. Rojo, LiMn2O4-based Composites Processed by a Chemical-route Microstructural, Electrical, Electrochemical, and Mechanical Characterization, Journal of Power Sources, 115, 315–322 (2003).

26. L. Fransson, T. Eriksson, K. Edström, T. Gustafsson and J. O. Thomas, Influence of Carbon Black and Binder on Li-ion Batteries, Journal of Power Sources, 101, 1-9 (2001).

27. A. Momchilov, A. Trifonova, B. Banov, B. Pourecheva, and A. Kozawa, Nonaqueous UFC Suspensions, Used as Conductive Additive in Cathodes for Lithium Batteries, Journal of Power Sources, 81–82 566–570 (1999).

28. K. Zaghib, J. Shim, A. Guerfi, P Charest, and K. A. Striebel, Effect of Carbon Source as Additives in LiFePO4 as Positive Electrode for Lithium-Ion Batteries, Electrochemical and Solid-State Letters, 8, A207-A210 (2005).

29. Y.-H. Chen, C.-W. Wang, G. Liu, X.-Y. Song, V. S. Battaglia, and A. M. Sastry, Selection of Conductive Additives in Li-Ion Battery Cathodes A Numerical Study, Journal of The Electrochemical Society, 154, A978-A986 (2007).

30. T.H. Cho, S.M. Park, M. Yoshio, T. Hirai, Y. Hideshima, Effect of Synthesis Condition on the Structure and Electrochemical Properties of Li[Ni1/3Mn1/3Co1/3]O2 Prepared by Carbonate Co-Precipitation Method, Journal of Power Sources, 142, 306-312 (2005).

31. M. Higuchi, K. Katayama, Y. Azuma, M. Yukawa, M. Suhara, Synthesis of LiFePO4 Cathode Material by Microwave Processing, Journal of Power Sources, 119-121, 258-261 (2003).

32. T. F. Fuller, M. Doyle, and J. Newman, Simulation and Optimization of the Dual Lithium Ion Insertion Cell, Journal of the Electrochemical Society, 141, 1-10 (1994).

33. J. Newman and K.E. Thomas-Alyea, Electrochemical Systems (third edition), pp. 209-212, John Wiley & Sons, New Jersey, 2004.

34. M. Doyle, J. Newman, A. S. Gozdz, C. N. Schmutz, and J.-M. Tarascon, Comparison of Modeling Predictions with Experimental Data from Plastic Lithium Ion Cells, Journal of the Electrochemical Society, 143, 1890-1903 (1996).

35. M. M. Thackeray, Manganese Oxides for Lithium Batteries, Progress in Solid State Chemistry, 25, l-71 (1997).

36. C. de Boor, Spline Toolbox 3 User's Guide, The MathWorks Inc., pp. 3.8, Natick, MA, 2006.

37. N. V. Queipo, R. T. Haftka, W. Shyy, T. Goel, R. Vaidyanathan, and P. K. Tucker, Surrogate-based Analysis and Optimization, Progress in Aerospace Sciences, 41, 1-28 (2005).

38. J. I. Madsen, W. Shyy and R. T. Haftka, Response Surface Techniques for Diffuser Shape Optimization, AIAA Journal, 38, 1512-1518 (2000).

39. T. Goel, R. Vaidyanathan, R. T. Haftka, W. Shyy, N. V. Queipo, and K. Tucker, Response Surface Approximation of Pareto Optimal Front in Multi-Objective Optimization, Computer Methods in Applied Mechanics and Engineering, 196, 879–893 (2007).

40. G. E. P. Box and K. B. Wilson, On the Experimental Attainment of Optimum Conditions, Journal of the Royal Statistical Society, Series B (Methodological), 13, pp. 1-45 (1951).

41. M. D. McKay and R. J. Beckman and W. J. Conover, A Comparison of Three Methods for Selecting Values of Input Variables in the Analysis of Output from a Computer Code, Technometrics, 21, 239-245 (1979).

42. R. H. Myers, and D. C. Montgomery, Response Surface Methodology: Process and Product Optimization Using Designed Experiments, pp. 17-48, John Wiley & Sons Inc: New York, 1995.

43. N. E. Dowling, Mechanical Behavior of Materials: Engineering Methods for Deformation, Fracture, and Fatigue (second edition), pp. 357-400, Prentice Hall, Upper Saddle River, NJ 1999.

44. Y. Shimakawa, T. Numata, and J. Tabuchi, Verwey-Type Transition and Magnetic Properties of the LiMn2O4 Spinels, Journal of Solid State Chemistry, 131, 138-143 (1997).

45. W. Shyy, S. S. Thakur, H. Ouyang, J. Liu, and E. Blosch, Computational Techniques for Complex Transport Phenomena, pp. 231-258, Cambridge University Press, New York, 1997.

46. A. R. Martin, C. Saltiel, W. Shyy, Heat Transfer Enhancement with Porous Inserts in Recirculating Flows, Journal of Heat Transfer, 120, 458-467 (1998).

47. E. Sozer and W. Shyy, Modeling of Fluid Dynamics and Heat Transfer through Porous Media for Liquid Rocket Propulsion, AIAA-2007-5549, 43rd AIAA/ASME/SAE/ASEE Joint Propulsion Conference and Exhibit, Cincinnati, OH, 2007.

48. W. E, B. Engquist, X. Li, W. Ren, and E. Vanden-Eijnden, Heterogeneous Multiscale Methods: a Review, Communications in Computational Physics, 2, 367-450 (2007).

CHAPTER IV

SURROGATE-BASED SCALE BRDGING AND MICROSCOPIC SCALE MODELING OF CATHODE ELECTRODE MATERIALS

1. INTRODUCTION

1.1. Challenges for Li-Ion Battery Modeling

Modeling of Li-ion batteries is of significant importance for both understanding physicochemical characteristics of the electrochemical system and guiding design optimization of batteries. However, modeling of Li-ion batteries is a challenging problem due to the presence of two special characteristics of the electrochemical system, multiphysics processes and disparate length and time scales.

A complicated electrochemical system like a Li-ion cell involves transport of ions and electrons [1], electrochemical reactions on solid active material and liquid electrolyte interface [1], heat generation and transfer [2], and intercalation-induced stress generation [3]. The corresponding governing equations for these physicochemical processes are coupled and the electrochemical kinetics is nonlinear. It is a nontrivial problem to solve this coupled nonlinear equation system.

Modeling of Li-ion batteries also needs to deal with disparate length scales and time scales. A battery typically consists of several cells. A schematic diagram and dimensional scales for a cell and its components are shown in Figure 4.1. As can be seen in Figure 4.1, along the thickness direction, scales range from 0.52 mm for the thickness

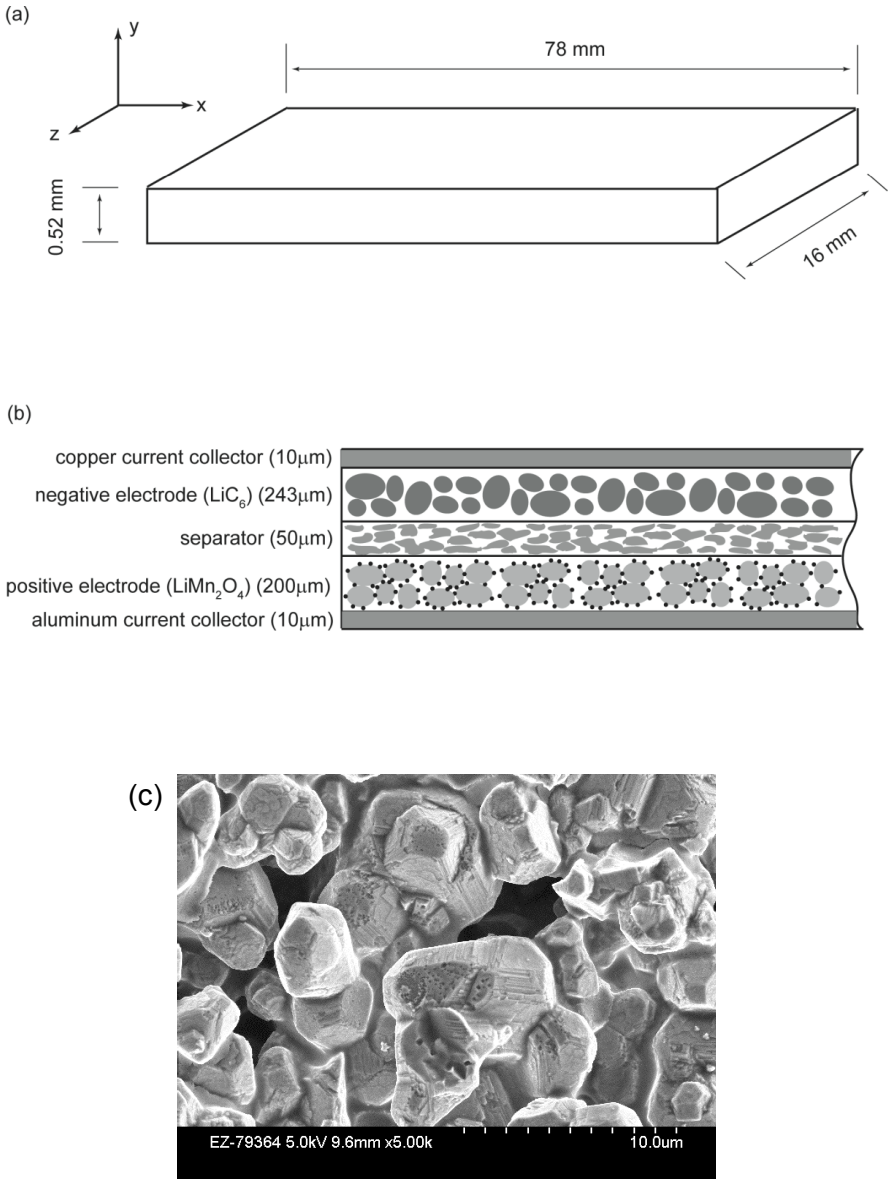

Figure 4.1: Scales in Li-ion batteries: (a) dimension for a single cell, (b) components and their dimensions inside a single cell along the thickness direction, and (c) a SEM image for $LiMn_2O_4$ positive electrode.

of a single cell to about 4 μm for the size of a single electrode particle. In this study, we refer to the battery scale as macroscopic scale and electrode particle scale as microscopic scale. It was shown in the numerical simulations of single particles [3], that solution for concentration has a relative 2-norm error of 1.78×10^{-4} and solution for intercalation-induced stress has a relative 2-norm error of 5.03×10^{-3} when 131 elements are used. For the single cell shown in Figure 4.1, there are 6×10^{8} electrode particles. Consequently, it requires 7.9×10^{10} elements to resolve all the microscopic scales to the electrode particle level assuming each particle contains 131 finite elements. Therefore, it cost tremendous computational power to resolve all the processes existing within each single electrode particle. It is also practically unfeasible to do so given the computation capability of existing computers. Time scales for physicochemical processes inside Li-ion batteries are given in Table 4.1. As shown in Table 4.1, time scale spans from seconds to hours during the cycling of batteries. From the modeling and numerical simulation point of view, very small time steps are required to resolve the process with the smallest time scale, and a large number of time steps are required to finish an entire discharge/charge cycle. In other words, the cost for the simulation of this transient process is very expensive. Special care has to be taken to devise a framework to tackle the disparate length and time scales in the modeling of Li-ion batteries.

1.2.Review of the Existing Li-Ion Battery Modeling Work in the Literature

Li-ion battery models in the existing literature with different fidelity are reviewed. There are equivalent-circuit-based models, physics-based pseudo 2D models, single particle 3D models, and a mesoscale 3D model.

Physicochemical processes	Characteristic time expression	Characteristic time representative values
Discharge	Q/I	~ 1 hour
Li ion diffusion in solid active material particles	r_s^2 / D_1	~ 4 minutes
Li ion diffusion in electrolyte	L^2 / D_2^{eff}	~ 2 minutes
Electrochemical reaction at interface	$1/\left[ak \left(c_{\max} \right)^{1/2} \right]$	~ 6 seconds

Table 4.1: Characteristic time scales for physicochemical processes inside a Li-ion battery.

Equivalent-circuit-based models, which originated from conventional electrochemical impedance spectroscopy (EIS) battery characterization techniques, use an equivalent electric circuit composed of resistors and capacitors to simulate cell performance and behavior [4, 5, 6]. This category of models does not require detailed understanding of the physicochemical mechanisms but requires certain parameters empirically fitted from experimental measurement data. Equivalent-circuit-based models are capable of rapidly predicting cell performance and behavior with simplified physics and adequate fidelity [5]. However, these models are also criticized because no detailed modeling of physicochemical processes is involved and they do not facilitate understanding of physical mechanisms.

Pseudo 2D models were first developed from porous electrode theory [7] by solving continuum scale governing equations for all the physicochemical processes over homogeneous media along the thickness direction of a cell [8]. The required effective material properties are commonly modeled by the classical Bruggeman equation. The volumetric reaction rate is calculated using a simplified separated spherical electrode particle by introducing a pseudo dimension. This category of models has been very successful not only for predicting cell performance and behavior but also for understanding the physical mechanisms of Li-ion batteries [9, 10, 11]. However, these models use oversimplified assumptions and models for effective material properties and volumetric reaction rates without detailed modeling of the microstructure architecture of electrode materials.

As an attempt to model the detailed 3D microstructure of electrode materials, a single electrode particle model was developed to model the intercalation-induced stress

and heat generation inside ellipsoidal cathode particles during the discharge and recharge cycles [3, 12]. This single particle numerical study showed that ellipsoidal particles with larger aspect ratios are preferred to reduce stress and heat generation. A mesoscale modeling approach was also proposed to implement the 3D detailed modeling of electrode materials consisting of regularly and randomly arranged cathode particles [13]. The results agreed well with experimental testing data. However, the amount of electrode particles included in the model was limited due to the excessive computation power requirement.

In summary, it appears that the multiphysics problem has been successfully addressed in the literature. However, the problem of disparate length and time scales has not been sufficiently studied to allow for detailed microstructural modeling of electrode architecture.

1.3. The Objectives of This Study

In this study, we will focus only on the treatment of disparate length scales to study the effect of microstructure. We will tackle the problem of disparate time scales by using sufficiently small time steps, assuming that we could afford conducting many time steps advancing temporally. To address the disparate length scales in modeling of Li-ion batteries, we set up the following objectives in this study.

(1) Develop a multiscale framework for Li-ion battery modeling to efficiently account for the effects of electrode microstructural architecture;

(2) Conduct microscopic modeling of electrode particle clusters and solve the closure terms in macroscopic scale governing equations as a first step toward implementing the multiscale framework.

2. METHODS

2.1. Li-Ion Cell Cycling Mechanisms and Governing Equations on Microscopic Scale

2.1.1. Li-Ion Battery Fundamentals

A Li-ion cell typically consists of the following components: positive and negative electrodes, a separator that isolates the two electrodes, and current collectors for both electrodes. Electrodes are typically made of particles glued together by binders. Pores inside electrodes and separator are commonly filled with liquid electrolyte that acts as a pathway for Li ions. Figure 1.1 shows a diagram for the components of a Li-ion cell and basic operation mechanisms for discharge/recharge cycling. During discharge of a cell, Li ions are extracted (deintercalated) from the negative electrode, transported through the electrolyte and finally inserted (intercalated) into the positive electrode. Meanwhile, electrons move from the negative electrode to the positive electrode through the external circuit and output work to the load. During recharge of a cell, Li ions and electrons are transferred in the reverse direction as opposed to the discharge process. This consumes work from the power supply to move the electrons. Intercalation and deintercalation comprise electrochemical reactions on the interface of solid active material and liquid electrolyte, diffusion of ions in the solid active material, and transport of electrons in the solid active material.

2.1.2.Transport Processes

The effect of existing electrons in solid active material on the species flux of lithium is assumed to be negligible because electrons are much more mobile than

intercalated atoms [14]. The chemical potential gradient is the driving force for the movement of lithium ions. Li ion transport is given as [14]

$$\mathbf{J} = c\mathbf{v} = -Mc\nabla\mu\,, \tag{1}$$

where $\mathbf{v}$ is the velocity of ion movements, M is the mobility of lithium ions, c is the concentration of Li ions, and μ is the chemical potential. Chemical potential depends on concentration, temperature, and stress field. In this study, only concentration-driven diffusion is considered. The governing equation for Li ion transport in solid active materials is then given by

$$\frac{\partial c_1}{\partial t} + \nabla\cdot\left(-D_1\nabla c_1\right) = 0\,, \tag{2}$$

where D is the diffusion coefficient of Li ions in the solid active materials and subscript 1 indicates variables for solid phase.

For the transport of lithium ion in the electrolyte, the concentrated solution theory is applied. The convection effect is neglected, and the species equation reads [1]

$$\frac{\partial c_2}{\partial t} = \nabla\cdot\left(D_2\nabla c_2\right) - \frac{\mathbf{i}_2\cdot\nabla t_+^0}{F}\,, \tag{3}$$

where subscript 2 indicates variables for liquid phase, $\mathbf{i}_2$ is the electric current in the liquid phase and t_+^0 is the transference number of lithium ions in solution and is assumed to be constant in this study. In other words, the last term on the right hand side of Equation (3) can be neglected.

The electron transport in the solid active material is governed by Poisson's equation

$$\nabla\cdot\mathbf{i}_1 = \nabla\cdot\left(\sigma_1\nabla V_1\right) = 0\,, \tag{4}$$

where $\mathbf{i}_1$ is electric current in the solid phase, σ_1 is conductivity of the solid phase, and V_1 is electrical potential in the solid phase.

The electrical potential in the liquid phase is governed by [1, 8]

$$\nabla \cdot \mathbf{i}_2 = \nabla \cdot \left(-\kappa \nabla V_2 - \frac{\kappa RT}{F} \left(1 + \frac{\partial \ln f}{\partial \ln c_2} \right) \left(1 - t_+^0 \right) \nabla \ln c_2 \right) = 0 , \tag{5}$$

where κ is conductivity of liquid electrolyte, V_2 is the potential of the liquid phase, R is the universal gas constant, T is absolute temperature, F is Faraday's constant, and f is the mean molar activity coefficient of the electrolyte (it is usually assumed to be constant due to lack of data). In Equation (5), a concentration dependant term is used to account for the charge carried by ionic motion in the electrolyte.

2.1.3.Electrochemical Kinetics

Chemical kinetics (reaction rate) are described by the Butler-Volmer equation [1, 9], as

$$j = \frac{i_n}{F} = \frac{i_0}{F} \left\{ \exp\left[\frac{(1-\beta)F}{RT} \eta \right] - \exp\left[-\frac{\beta F}{RT} \eta \right] \right\}, \tag{6}$$

where i_0 is exchange current density, i_n is the reaction current density per unit area, η is surface overpotential, and β is a symmetry factor that represents the fraction of the applied potential promoting the cathodic reaction[1]. The exchange current density i_0 is given by,

$$i_0 = Fk(c_l)^{1-\beta} (c_\theta)^{1-\beta} (c_s)^{\beta} , \tag{7}$$

where c_l is the concentration of lithium ion in the electrolyte, c_s is the concentration of lithium ion on the surface of the solid electrode, c_θ is the concentration of available vacant sites on the surface ready for lithium intercalation (which is the difference

between stoichiometric maximum concentration and current concentration on the surface of the electrode $c_{\max} - c_s$), and k is a reaction rate constant [9]. Surface overpotential η is given, without considering film resistance, by [9]

$$\eta = V_1 - V_2 - U\,, \tag{8}$$

where V_1 and V_2 are electric potential for the solid and liquid phase respectively, and U is the open-circuit potential, which depends on lithium ion concentration.

2.1.4.Intercalation-induced Stress Generation

When Li ions are intercalated into the lattice of active material in electrodes, the lattice is expanded accordingly. This lattice expansion causes strain inside the material. Non-uniform strain results in stress, the so-called intercalation-induced stress. To model this intercalation-induced stress, an analogy to thermal stress is proposed [3]. The constitutive equation between stress and strain is [3]

$$\varepsilon_{ij} = \frac{1}{E}\left[(1+\nu)\sigma_{ij} - \nu\sigma_{kk}\delta_{ij}\right] + \frac{\tilde{c}\Omega}{3}\delta_{ij} \tag{9}$$

where ε_{ij} are strain components, σ_{ij} are stress components, E is Young's modulus, ν is Poisson's ratio, $\tilde{c} = c - c_0$ is the concentration change of the diffusion species (lithium ion) from the original (stress-free) value, and Ω is the partial molar volume of lithium. Stress components are subjected to the force equilibrium equation

$$\sigma_{ij,\,i} = 0 \quad (j = 1,\, 2,\, 3)\,. \tag{10}$$

A Young's modulus $E = 10\text{GPa}$ and a partial molar volume $\Omega = 3.497 \times 10^{-6}\,\text{m}^3/\text{mol}$ [3] are used here.

2.1.5.Heat Generation and Transfer

There are four sources of heat generation inside lithium ion batteries during operation [15]

$$\dot{Q}_g = I\left(V - U^{\text{avg}}\right) + IT\frac{\partial U^{\text{avg}}}{\partial T} + \sum_{\text{k}} \Delta H_{\text{k}}^{\text{avg}} r_{\text{k}} + \int \sum_{\text{j}} \sum_{\text{i}} \left(\bar{H}_{\text{ij}} - \bar{H}_{\text{ij}}^{\text{avg}}\right) \frac{\partial c_{\text{ij}}}{\partial t} \text{d}v \tag{11}$$

The first term, $I\left(V - U^{\text{avg}}\right)$, is the irreversible resistive heating, where I is the current of the cell, V is the cell potential, and U^{avg} is the volume averaged open circuit potential. Resistive heating is caused when the cell potential deviates from its equilibrium because of resistance to the passage of current. The second term, $IT\partial U^{\text{avg}}/\partial T$, is the reversible entropic heat, where T is temperature. The third term, $\sum_{\text{k}} \Delta H_{\text{k}}^{\text{avg}} r_{\text{k}}$, is the heat change of chemical side reactions, where $\Delta H_{\text{k}}^{\text{avg}}$ is the enthalpy of reaction for chemical reaction *k*, and r_{k} is the rate of reaction *k*. The fourth term, $\int \sum_{\text{j}} \sum_{\text{i}} \left(\bar{H}_{\text{ij}} - \bar{H}_{\text{ij}}^{\text{avg}}\right) \partial c_{\text{ij}} / \partial t \, \text{d}v$, is the heat of mixing due to the generation and relaxation of concentration gradients, where c_{ij} is the concentration of species *i* in phase *j*, $\text{d}v$ is the differential volume element, and $\bar{H}_{\text{ij}}$ and $\bar{H}_{\text{ij}}^{\text{avg}}$ are the partial molar enthalpy of species *i* in phase *j* and the averaged partial molar enthalpy respectively. The study conducted on single particles showed that heat of mixing is negligible compared to resistive heat and entropic heat [12]. Therefore, there are only two heat generation sources of significance, resistive heat and entropic heat, without considering heat change due to side reactions.

Heat transfer inside Li-ion batteries can be modeled by the conventional heat conduction equation [16, 17],

$$\rho C_p \frac{\partial T}{\partial t} = \frac{\partial}{\partial x}\left(k_x \frac{\partial T}{\partial x}\right) + \frac{\partial}{\partial y}\left(k_y \frac{\partial T}{\partial y}\right) + \frac{\partial}{\partial z}\left(k_z \frac{\partial T}{\partial z}\right) + \dot{Q}, \tag{12}$$

where ρ is density, C_p is heat capacity, and k_x, k_y, k_z are heat conductivity along x, y and z directions respectively. Heat conductivity is generally anisotropic for battery materials due to different components inside batteries.

2.2. Multiscale Modeling Framework

2.2.1. Volume Averaging Technique

The main objective of multiscale modeling is to capture the physics to a certain desired accuracy in an efficient way. Microscopic models are accurate but computationally expensive, while macroscopic models are simplified and efficient. The combinational use of models on these two scales will help to achieve accuracy and efficiency at the same time. Microscopic and macroscopic models could be fundamentally different in terms of the physics principles applied. For example, one could apply molecular dynamics to the microscopic scale and continuum fluid dynamics to the macroscopic scale. Sometimes, one basic physics principle is applicable for all scales and scale disparity is caused by the geometric complexity, which is the case for the processes in porous electrode materials. For the multiscale modeling of the processes in porous media, there are two approaches that can be adopted to derive the macroscopic governing equations from their counterparts on the microscopic scale, volume averaging [18] and homogenization [19][20]. The volume averaging technique is used in this study.

In the volume averaging technique, the variable of interest is first averaged over a representative elementary volume (REV). The governing equations on the microscopic scale are then averaged over REV. In the differential equations, the volumetric averages of the temporal and spatial derivatives are transformed into the temporal and spatial derivatives of the averaged quantities by using the two theorems dealing with the

averages of derivatives [18]. There are additional closure terms, which require further modeling, appearing as the consequence of the averaging process. Volume averaging has been widely used for modeling fluid flow and transport in porous media [18, 21]. Volume averaging-like techniques have been applied for battery modeling to deal with the porous feature of electrode materials [8, 9, 22, 23]. However, closure terms for effective material properties and volumetric reaction rate have only been treated analytically using oversimplified assumptions instead of detailed numerical modeling of microstructural architecture.

There are two types of volume averages, defined as

- Intrinsic volume average

$$\overline{c_s}^{s} = \frac{1}{\mathrm{d}V_s}\int_{\mathrm{d}V} c_s \gamma_s \mathrm{d}V \,, \tag{13}$$

where $\mathrm{d}V$ is the volume of REV, $\gamma_s = 1$ in phase *s* and 0 elsewhere.

- Volume average

$$\overline{c_s} = \frac{1}{\mathrm{d}V}\int_{\mathrm{d}V} c_s \gamma_s \mathrm{d}V \,, \tag{14}$$

These two averages are related as

$$\overline{c_s}^{s} = g_s \overline{c_s} \tag{15}$$

where g_s is the volume fraction of phase *s*.

When the volume averaging technique is applied to partial differential equations, volume averages of temporal and spatial derivatives need to be transformed into derivatives of volume averages of variables following these two theorems,

$$\frac{1}{\mathrm{d}V}\int_{\mathrm{d}V}\left(\frac{\partial c_s}{\partial t}\right)\gamma_s \mathrm{d}V = \frac{\partial \overline{c_s}}{\partial t} - \frac{1}{\mathrm{d}V}\int_{A_s} c_s \mathbf{v}\cdot\mathbf{n}\mathrm{d}A \,, \tag{16}$$

$$\frac{1}{\mathrm{d}V}\int_{\mathrm{d}V}\nabla\cdot\left(D_s\nabla c_s\right)\gamma_s\,\mathrm{d}V=\nabla\cdot\left(\overline{D_s\nabla c_s}\right)+\frac{1}{\mathrm{d}V}\int_{A_s}\left(D_s\nabla c_s\right)\cdot\mathbf{n}\mathrm{d}A\,, \tag{17}$$

where $\mathbf{v}$ is the velocity of the microscopic interface and $\mathbf{n}$ is the outward unit norm of the infinitesimal area element $\mathrm{d}A$, if the terms in a transient diffusion equation is used for an example. In Li-ion battery modeling, the movement of solid active material and liquid electrolyte phase interface is negligible, which means the second term $1/\mathrm{d}V\int_{A_s}c_s\mathbf{v}\cdot\mathbf{n}\mathrm{d}A$ on the right side of Equation (16) vanishes. In Equation (17), two closure terms on the right side of the equation need special treatment. $\nabla\cdot\left(\overline{D_s\nabla c_s}\right)$ is the gradient of the averaged diffusion flux. Traditionally, the average of diffusion flux resulting from the concentration gradient is modeled by introducing a so-called effective diffusivity,

$$\overline{D_s\nabla c_s}=D_s^{\mathrm{eff}}\overline{\nabla c_s}\,, \tag{18}$$

and the effect diffusivity is conventionally modeled analytically using classical Bruggeman's relation

$$D_s^{\mathrm{eff}}=D_s^{\mathrm{bulk}}g_s^{\alpha}\,, \tag{19}$$

where D_s^{bulk} is the bulk diffusivity of homogeneous materials without inclusions, and α is Bruggeman's coefficient that is normally assumed to take the value of 1.5. However, it has been shown that a Bruggeman exponent of 1.5 is often invalid for real electrode materials [24]. In this study, we propose to calculate the volume average of the diffusion flux or the effective diffusivity directly from 3D microscopic scale simulations instead of modeling them analytically. The second term on right side of Equation (17) is the integral of diffusion flux over the phase interface. In Li-ion battery modeling, this term accounts for the flux due to electrochemical reaction on the interface of solid active material and liquid electrolyte. Therefore, the term of $J=1/\mathrm{d}V\int_{A_s}\left(D_s\nabla c_s\right)\cdot\mathbf{n}\mathrm{d}A$ is actually the Li ion

production or consumption per unit volume due to electrochemical reaction, and this term is called the volumetric reaction rate. In the conventional pseudo 2D models, this volumetric reaction rate term has been modeled using a simplified geometry of an isolated spherical particle as [8]

$$J = a_s j_n , \tag{20}$$

where $a_s = 3g_s / r_s$ is the specific interfacial area (per unit volume) of an isolated spherical particle with radius r_s given the solid phase volume faction g_s, and j_n is the reaction flux per unit area calculated by Butler-Volmer equation (Equation (6)) using the volume averaged Li-ion concentration in the liquid electrolyte, volume averaged electrical potential in both liquid and solid phases, and Li ion concentration on an isolated spherical particle surface by solving the diffusion equation on a pseudo dimension. In other words, Equation (20) assumes that

$$\begin{aligned} J &= 1/\mathrm{d}V \int_{A_s} \left(D_s \nabla c_s \right) \cdot \mathbf{n} \mathrm{d}A = 1/\mathrm{d}V \int_{A_s} j_n(\mathrm{c}_1, \mathrm{c}_2, \mathrm{V}_1, \mathrm{V}_2) \mathrm{d}A \\ &\approx \frac{\mathrm{d}A}{\mathrm{d}V} j_n(\mathrm{c}_1, \overline{\mathrm{c}_2}, \overline{\mathrm{V}_1}, \overline{\mathrm{V}_2}) \approx \frac{3g_s}{r_s} j_n(\mathrm{c}_1, \overline{\mathrm{c}_2}, \overline{\mathrm{V}_1}, \overline{\mathrm{V}_2}) \end{aligned} , \tag{21}$$

where reaction flux $j_n(\mathrm{c}_1, \mathrm{c}_2, \mathrm{V}_1, \mathrm{V}_2)$ is calculated by Butler-Volmer equation using local concentrations and electric potentials, and $j_n(\mathrm{c}_1, \overline{\mathrm{c}_2}, \overline{\mathrm{V}_1}, \overline{\mathrm{V}_2})$ is calculated by Butler-Volmer equation using local Li ion concentration in the solid phase, volume averaged Li ion concentration in the liquid phase, and volume averaged electric potentials in both phases. A trivial case where Equation (21) holds would be the case where all the concentrations and electrical potentials are uniformly distributed on the microscopic scale, and electrodes are made of isolated spherical particles. The treatment for this volume averaged reaction rate could be improved by direct calculation from microscopic scale

modeling and simulations, which is the focus of this study. Details about coupling between microscopic scale and macroscopic scales will be discussed in the section on scale bridging.

For the sake of clarity and completeness, the derivation of governing equations using the volume averaging technique will be described here even though similar derivations have been given in [22, 23]. The derivation of macroscopic governing equations using the volume averaging technique is presented as follows.

(1) Transport of Lithium Ions inside Liquid Electrolyte Phase

When the transference number t_+^0 is assumed to be constant, the transport equation for lithium ion concentration is simplified as

$$\frac{\partial c_2}{\partial t} = \nabla \cdot \left(D_2 \nabla c_2 \right). \tag{22}$$

Take the volume average of both sides,

$$\frac{1}{\mathrm{d}V} \int_{\mathrm{d}V} \left(\frac{\partial c_2}{\partial t} \right) \gamma_2 \mathrm{d}V = \frac{1}{\mathrm{d}V} \int_{\mathrm{d}V} \nabla \cdot \left(D_2 \nabla c_2 \right) \gamma_2 \mathrm{d}V \,. \tag{23}$$

With the theorems for the time derivative term and divergence term in volume averaging technique, Equation (23) becomes

$$\frac{\partial \overline{c_2}}{\partial t} = \nabla \cdot \left(\overline{D_2 \nabla c_2} \right) + \frac{1}{\mathrm{d}V} \int_{A_s} \left(D_2 \nabla c_2 \right) \cdot \mathbf{n} \mathrm{d}A + \frac{1}{\mathrm{d}V} \int_{A_s} c_2 \mathbf{v} \cdot \mathbf{n} \mathrm{d}A \,. \tag{24}$$

Neglect the movement of the interface (i.e. $\mathbf{v} \cdot \mathbf{n} = 0$), rewrite the average flux as $\overline{D_2 \nabla c_2} = D_2^{eff} \nabla \overline{c_2}$, and use J_{c_2} to represent volumetric rate, one transforms Equation (24) into

$$\frac{\partial \overline{c_2}}{\partial t} = \nabla \cdot \left(D_2^{eff} \nabla \overline{c_2} \right) + J_{c_2} \,. \tag{25}$$

(2) Electrical Potential inside Liquid Electrolyte Phase

The transport equation for the electric current inside the liquid electrolyte Equation (5) can be re-written as,

$$\nabla \cdot \left[\kappa \nabla V_2 + \kappa_D \nabla \left(\ln c_2 \right) \right] = 0 \,, \tag{26}$$

where $\kappa_D = \frac{\kappa RT}{F} \left(1 + \frac{\partial \ln f}{\partial \ln c_2} \right) \left(1 - t_+^0 \right)$. Take the volume averaging over the left side of Equation (26),

$$\frac{1}{\mathrm{d}V} \int_{\mathrm{d}V} \nabla \cdot \left[\kappa \nabla V_2 + \kappa_D \nabla \left(\ln c_2 \right) \right] \gamma_2 \mathrm{d}V = \nabla \cdot \left(\overline{\kappa \nabla V_2 + \kappa_D \nabla \left(\ln c_2 \right)} \right) + \frac{1}{\mathrm{d}V} \int_{A_s} \left(\kappa \nabla V_2 + \kappa_D \nabla \left(\ln c_2 \right) \right) \cdot \mathbf{n} \mathrm{d}A \,, \tag{27}$$

$J_{V_2} = \left(1/\mathrm{d}V \right) \int_{A_s} \left(\kappa \nabla V_2 + \kappa_D \nabla \left(\ln c_2 \right) \right) \cdot \mathbf{n} \mathrm{d}A$ is the volume averaged reaction current at the interface, and $\overline{\kappa \nabla V_2 + \kappa_D \nabla \left(\ln c_2 \right)}$ could be modeled as $\kappa^{eff} \nabla \overline{V_2} + \kappa_D^{eff} \nabla \left(\overline{\ln c_2} \right)$. Following [22], $\overline{\ln c_2}$ could be approximated using Taylor series expansion as

$$\overline{\ln c_2} = \frac{1}{V} \int_{V_2} \ln c_2 \mathrm{d}V \approx \frac{1}{V} \int_{V_2} \left[\ln \overline{c_2} + \frac{1}{\overline{c_2}} \left(c_2 - \overline{c_2} \right) \right] \mathrm{d}V = g_2 \ln \overline{c_2} \,, \tag{28}$$

thus Equation (27) becomes

$$\nabla \cdot \left[\kappa^{eff} \nabla \overline{V_2} + g_2 \kappa_D^{eff} \nabla \left(\ln \overline{c_2} \right) \right] + J_{V_2} = 0 \,. \tag{29}$$

(3) Transport of Lithium Ions inside Solid Active Material Phase

Applying the volume averaging technique to Equation (2) for diffusion of Li ions in solid phase with a similar procedure as that done for transport in liquid phase, Equation (22), we have the volume averaged equation for Equation (2) as

$$\frac{\partial \overline{c_1}}{\partial t} = \nabla \cdot \left(D_1^{eff} \nabla \overline{c_1} \right) + J_{c_1} \,, \tag{30}$$

where J_{c_1} is the volume averaged reaction rate.

(4) Transport of Electrons inside Solid Active Material Phase

Apply the volume averaging technique to the electrical potential equation in solid phase Equation (4), and notice that

$$\frac{1}{\mathrm{d}V}\int_{\mathrm{d}V}\nabla\cdot\left(\sigma\nabla V_1\right)\gamma_1\mathrm{d}V=\nabla\cdot\left(\overline{\sigma\nabla V_1}\right)+\frac{1}{\mathrm{d}V}\int_{A_s}\left(\sigma\nabla V_1\right)\cdot\mathbf{n}\mathrm{d}A\ , \tag{31}$$

one obtains,

$$\nabla\cdot\left(\overline{\sigma\nabla V_1}\right)+\frac{1}{\mathrm{d}V}\int_{A_s}\left(\sigma\nabla V_1\right)\cdot\mathbf{n}\mathrm{d}A=0\ , \tag{32}$$

$\overline{\sigma\nabla V_1}$ could be modeled as $\sigma^{eff}\nabla\overline{V_1}$ where σ^{eff} is effective conductivity. Term $(1/\mathrm{d}V)\int_{A_s}\left(\sigma\nabla V_1\right)\cdot\mathbf{n}\mathrm{d}A$ is a volume averaged boundary reaction current that can be represented by J_{V_1}. Consequently, Equation (32) turns to

$$\sigma^{eff}\nabla\overline{V_1}+J_{V_1}=0\ . \tag{33}$$

In Equation (33), effective conductivity σ^{eff} and volumetric reaction flux J_{V_1} are two closure terms requiring special treatment.

2.2.2.Scale Bridging

As shown in the previous subsection, there are some closure terms requiring special treatment in the volume averaged governing equations. These terms are the effective material properties, D_2^{eff}, κ^{eff}, κ_D^{eff}, D_1^{eff}, and σ^{eff}; and volume averaged reaction rates, J_{c_2}, J_{V_2}, J_{c_1}, and J_{V_1}. These closure terms highly depend on the detailed microstructural architecture of electrode materials. In this study, we propose to calculate the closure terms, based on their definitions, directly from 3D microscopic scale simulations.

Following the scale bridging concept from [25, 26], a REV on the microscopic scale is assigned to each integration point of the macro-mesh. Appropriate boundary

conditions, derived from information available from the macroscopic scale, are imposed on REV on the microscopic scale. A separate computation is then conducted for the REV, and the obtained variable values are averaged over REV to provide macroscopic closure terms with which the governing equations on macroscopic scale are solved. This provides an approach to determine the macroscopic response of heterogeneous materials with accurate accounting of micro-structural characteristics.

There are two categories of approaches to couple microscopic and macroscopic scales, concurrent coupling and serial coupling [27]. In the concurrent coupling approach, microscopic and macroscopic models are conducted concurrently with simultaneous information exchange. In serial coupling, an effective macroscopic model is determined from the microscopic model in a pre-processing step. It is expensive to conduct microscopic and macroscopic scale simulations concurrently since microscopic scale simulations are generally time consuming (in the case of battery modeling, microstructural information of electrode materials needs to be resolved). Therefore, in this study we preferred to adopt the serial coupling approach. To systematically arrange the simulations on microscopic scale and couple the two scales efficiently, the database approach [28] and look up table approach [29] have been used to map the microscopic information and macroscopic closure terms. In this study we propose a surrogate-based approach to bridge the scales serially. Surrogate-based approaches have been used for design optimization and analysis [30]. Surrogate models are constructed using numerical results obtained from simulations on carefully sampled points; they are capable of predicting the objective functions efficiently over the whole design space once these models are validated for sufficient accuracy. In applying a surrogate-based approach for

scale bridging in battery modeling, the input variables for the surrogate models are the microscopic structure information (such as volume fraction, aspect ratio of particles and equivalent particle radius) and boundary conditions, for microscopic scale simulations, from the nodes values on macroscopic scale mesh, and the output variables are those closure terms calculated from microscopic scale simulations, as illustrated in Figure 4.2. Details of surrogate-based scale bridging will be discussed in section 2.4.

2.3. 3D Microscopic Modeling of Electrode Particle Clusters

2.3.1.Microstructural Geometry Generation

To model the microstructural architecture, we use a collision-driven molecular dynamics algorithm [31] to generate clusters of electrode particles. A certain number of identical ellipsoidal particles with specified aspect ratio are packed inside a cubic box. Since electrolyte does not contribute to conduction of electrons, to create a continuous path for electron conduction the semi axes of these particles are multiplied by a coefficient (1.1 is used in this study) to create an artificial overlapping between particles. Those parts of the particles falling outside of the box are cut out. The remaining portion of the particle cluster consists of the solid active material phase of the electrode microstructure. The void space inside the cubic box not occupied by the particle cluster consists of the liquid electrolyte phase.

2.3.2.Microstructural Geometry Characterization Parameters

In this study, microstructure of the representative volume element is primarily characterized using volume fraction of solid phase, equivalent radius of solid particles, and aspect ratio of prolate solid particles. Volume fraction determines how much active material is available in the electrode and decides the maximum possible capacity of a

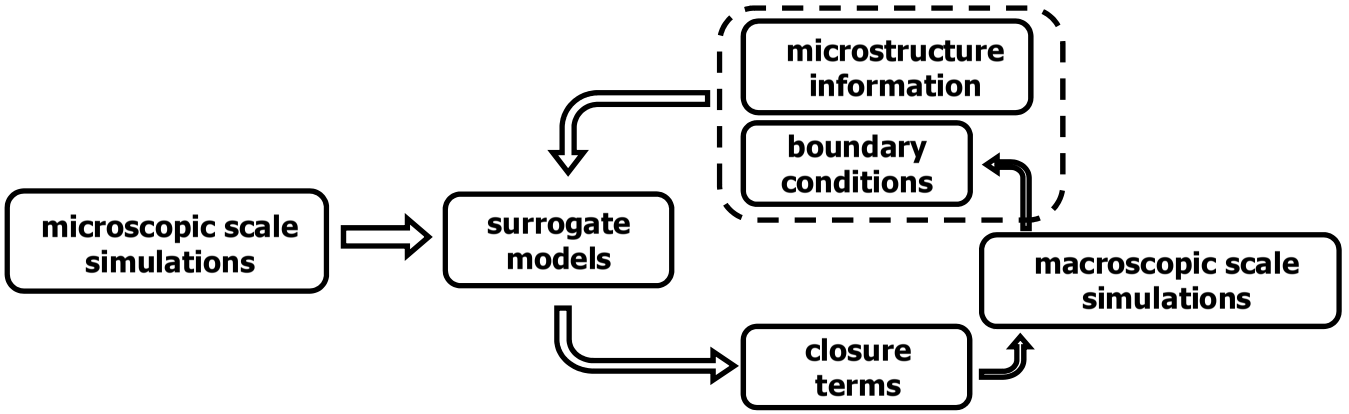

Figure 4.2: Surrogate-based scale bridging for multiscale modeling framework.

cell. On the other hand, volume fraction of solid phase also dictates the volume fraction of its counterpart, the liquid electrolyte phase. In the case of too small a volume fraction for liquid electrolyte, Li ions in the liquid electrolyte are depleted very quickly and cell performance is limited by transport of ions in the liquid electrolyte phase. Equivalent radius of ellipsoidal particles is defined as the radius of a sphere with the same volume. The equivalent particle size decides the characteristic length and time for diffusion; diffusion can be a limiting factor of battery performance, especially at very high cycling rates. In this study, we only consider ellipsoidal particles in prolate shape. The aspect ratio of a prolate particle is defined by the ratio between the long and short semi-axes. The surface area of a prolate particle with fixed volume increases as the aspect ratio increases. Therefore, the aspect ratio of particles actually determines the specific interfacial area available for electrochemical reaction and is an important characteristic for microstructure.

2.3.3.Governing Equations, Boundary Conditions, Material Properties and Implementation

The governing equations solved for 3D microscopic simulations over REV are Equation (2), (3), (4), (5), and (6). Steady state solutions are pursued. In other words, the unsteady terms from temporal derivatives are not solved in Equation (2) and (3). As described earlier, the boundary conditions take the node value from macroscopic scale simulations. The interface of solid and liquid phases has diffusional and current flux given by the Butler-Volmer equation. All other boundaries of the cubic box are set to be symmetric without net flux of electrons or ions.

Solid phase ($LiMn_2O_4$)	
Diffusivity	$D = 1\times10^{-13}\, m^2/s$
Conductivity	$\sigma = 3.8\ \mathrm{S}/m$
Maximum concentration	$c_{\text{total}} = 2.363\times10^{4}\ mol/m^3$
Open circuit potential	$U(y) = 4.06279 + 0.0677504 * \tanh(-21.8502y + 12.8268) - 0.105734(y^{-0.379571} - 1.575994) - 0.045\exp(-71.69y^{8}) + 0.01\exp(-200y - 0.19)\ \mathrm{V}$
Liquid phase ($LiPF_6$ in EC:DMC)	
Diffusivity	$D = 5.34\times10^{-10}\exp(-\frac{0.65c_2}{1000})\ m^2/s$
Ionic conductivity	$\sigma = 0.0911 + 1.9101\frac{c_2}{1000} - 1.052\left(\frac{c_2}{1000}\right)^2 + 0.1554\left(\frac{c_2}{1000}\right)^3\ \mathrm{S}/m$
Transference number	$t_0^+ = 0.4$

Table 4.2: Material properties for 3D microscopic scale simulations.

$LiMn_2O_4$ is selected as the active material for the cathode, and $LiPF_6$ in EC:DMC is selected as the electrolyte. Material properties used for simulations are summarized in Table 4.2.

The governing equations and boundary conditions are implemented in COMSOL Multiphysics®. Separate geometries are created for the solid and liquid phases respectively. The coupling between the two phases are implemented using the 'Extrusion Coupling Variables' capability in COMSOL Multiphysics®. The concentration and electric potential of the liquid phase at the two phase interface boundary are mapped to the boundary of the solid phase. This enables the calculation of reaction flux at the solid phase boundary by the Butler-Volmer equation. The calculated reaction flux is then mapped from the solid phase boundary to the liquid phase boundary, where the specified flux boundary condition is assigned for the transport equations of electrons and ions. This is a two-way coupling between the two phases; the coupling in both ways is carried out simultaneously when the governing equations are solved.

2.4. Surrogate-Based Scale Bridging

Surrogate models are used to rapidly predict the closure terms in macroscopic governing equations. The input variables (design variables) for surrogate models are the microstructural information and boundary conditions for microscopic scale simulations; the output variable (objective function) is the volumetric reaction rate. Surrogate models are constructed based on 3D microscopic simulations as described in the previous section. In this study, the microstructural information (volume fraction, aspect ratio of particles and equivalent radius of particles) is considered as fixed to reduce the dimensionality of the surrogate modeling problem. The concept demonstrated in this study could be easily

extended to include microstructure information. The key steps of surrogate modeling include design of experiments, running numerical simulations (computer experiments), construction of surrogate models, validation and further refinement of the models if necessary [30, 32, 33].

The design variables (boundary conditions for microscopic scale) are the concentration and its gradient of Li ions and the electric potential and its gradient in both solid and liquid phases. The ranges of the design variables are listed in Table 4.3, where normalized Li ion concentration $\tilde{c}_1 = c_1 / c_{\text{total}}$ in the solid active material phase is used and is equivalent to the state of charge *y*. The ranges of variables are decided based on their corresponding values in the possible pseudo 2D model solutions for cycling rates up to 3C. In Table 4.3, the variables of concentration and potential themselves are assigned to the center of a REV; the gradients of variables that carry the information of variable distribution are used, along with the variable values at the center of the REV, to calculate the values on the top and bottom boundaries of the REV. In the ideal case, the values of these variables come from solving the macroscopic governing. In this study, we assign the values arbitrarily without considering the constraint of the macroscopic scale governing equations, except for a constraint for solid phase concentration and electric potential, $-0.2 \le V_1 - U(\tilde{c}_1) \le 0.2$, in order to avoid numerical convergence issues potentially caused by the exponential terms in the Butler-Volmer equation. In the constrained design space, 189 points are selected by Latin hypercube sampling, and 128 points are selected at the corners of the design space to cover the boundary regions. Numerical simulations on microscopic scale are run on these sampled points.

Variables	Symbol	Range	Unit
Li ion concentration (solid)	$\tilde{c}_1$	0.2 ~ 0.9	1
Li ion concentration gradient (solid)	$\tilde{c}_{1,z}$	-3500~0	1/m
Electric potential (solid)	V_1	3.0 ~ 4.15	V
Electric potential gradient (solid)	$V_{1,z}$	-40~0	V/m
Li ion concentration (liquid)	c_2	600 ~ 1000	mol/m^3
Li ion concentration gradient (liquid)	$c_{2,z}$	$-6.5x10^6$~0	mol/m^4
Electric potential (liquid)	V_2	-1~0	V
Electric potential gradient (liquid)	$V_{2,z}$	-550~0	V/m

Table 4.3: Input variables and their range for 3D microscopic scale simulations.

The obtained simulations results are used to construct surrogate models. Commonly available surrogate models include polynomial response surface (PRS), kriging, radial basis neural network (RBNN), support vector regression and weighted average surrogates. Polynomial response surface, kriging, and radial basis neural network models will be used in this study.

After surrogate models are constructed, their accuracy is evaluated using error measures such as prediction error sum of squares (PRESS) and the adjusted coefficient of multiple determination R^2_{adj} [34] for polynomial response surface. The adjusted coefficient of multiple determination R^2_{adj} is a measure of how well the approximation explains variation of the objective functions caused by design variables. For a good fit, this coefficient should be close to one. PRESS is a cross-validation error. It is the summation of squares of all PRESS residues, each of which is calculated as the difference between the simulation by computer experiments and the prediction by surrogate models constructed from the remaining sampling points while excluding the point of interest [34]. The smaller the PRESS error, the more accurate the surrogate model will be. Surrogate models are also evaluated by comparing surrogate model prediction and actual numerical simulation results from microscopic scale modeling on testing points.

2.5. Summary of the Multiscale Modeling Framework

The proposed multiscale modeling framework is summarized in Figure 4.3. The volume averaging technique is used to derive macroscopic governing equations for cell scale modeling. The resulted closure terms are proposed to be calculated directly from 3D microscopic simulations instead of analytical modeling with oversimplified assumptions.

Microscopic scale:
3D electrode microstructure

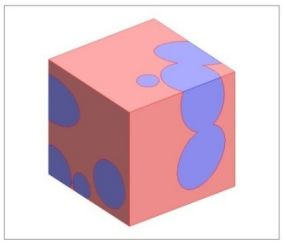

Macroscopic scale:
1D Li-ion cell

Anode | Separator | Cathode

$$\frac{\partial c_2}{\partial t} = \nabla \cdot \left(D_2 \nabla c_2 \right)$$

$$\nabla \cdot \left[\kappa \nabla V_2 + \kappa_D \nabla \left(\ln c_2 \right) \right] = 0$$

$$\frac{\partial c_1}{\partial t} + \nabla \cdot \left(-D_1 \nabla c_1 \right) = 0$$

$$\nabla \cdot \mathbf{i}_1 = \nabla \cdot \left(\sigma_1 \nabla V_1 \right) = 0$$

Volume averaging

$$\frac{\partial \overline{c_2}}{\partial t} = \nabla \cdot \left(D_2^{\text{eff}} \nabla \overline{c_2} \right) + J_{c_2}$$

$$\nabla \cdot \left[\kappa^{\text{eff}} \nabla \overline{V_2} + \varepsilon_2 \kappa_D^{\text{eff}} \nabla \left(\ln \overline{c_2} \right) \right] + J_{V_2} = 0$$

$$\frac{\partial \overline{c_1}}{\partial t} = \nabla \cdot \left(D_1^{\text{eff}} \nabla \overline{c_1} \right) + J_{c_1}$$

$$\sigma^{\text{eff}} \nabla \overline{V_1} + J_{V_1} = 0$$

Closure terms:

- **Effective material properties**

  D_2^{eff} κ^{eff} κ_D^{eff} D_1^{eff} σ^{eff}

- **Volumetric reaction rate**

  J_{c_2} J_{V_2} J_{c_1} J_{V_1}

- **Calculated directly from 3D microscopic simulations**

Training data from 3D microscopic scale simulations → Surrogate models → Prediction of closure terms for macroscopic scale simulations

Figure 4.3: Summary of the multiscale framework.

To efficiently bridge microscopic and macroscopic scales, training data from 3D microscopic simulations are used to construct surrogate models to rapidly and efficiently predict closure terms in macroscopic scale simulations.

3. RESULTS AND DISCUSSION

3.1. Analysis of 3D Microscopic Simulation Results

Figure 4.4 shows the generated geometry for two phases. The specified parameters for the microstructure are as follows: solid phase volume fraction is 0.6, particle aspect ratio is 2, and equivalent particle radius is 5.34μm. There are 10 identical ellipsoidal particles in the solid phase. The computational domain including both phases is 10μm×10μm×10μm.

Figure 4.5 shows an example solution of Li ion concentration in both phases and the reaction electric current at the interface. The boundary conditions at the bottom and top boundaries are node values taken from a pseudo 2D model simulation solution at z=170μm and z=180μm in the cathode at time t=2.173min. This indicates that the REV is placed at z=175μm on the macroscopic mesh. In the pseudo 2D simulation set up, the cell is discharged at 1C, the thickness for anode, separator, and cathode is 100, 25, and 100 μm, respectively. z axis goes from the anode to the cathode. The cathode starts from z=125μm to z=225μm. It is shown in Figure 4.5 (a) that Li ion concentration accumulates at the middle of the simulation domain for this particular case because the inserted Li ions could not be diffused out quickly enough due to the intrinsically low diffusivity of the solid active material phase. However, this is not the case for Li ion concentration distribution in the liquid electrolyte, as shown in Figure 4.5 (b), because liquid electrolyte

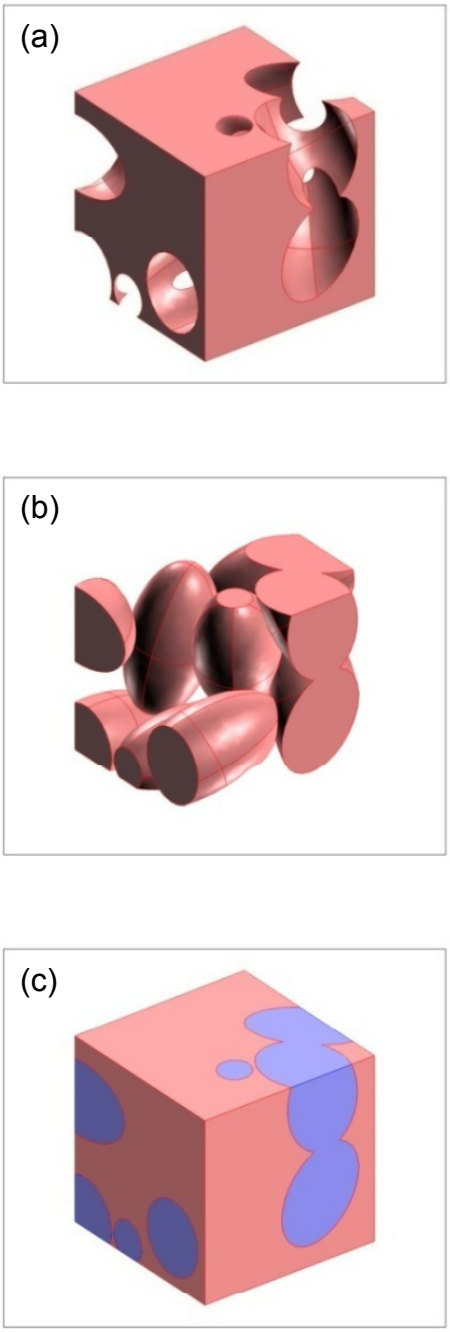

Figure 4.4: Generated microstructure: (a) liquid phase of electrolyte, (b) solid phase of active material, and (c) the whole simulation domain containing both phases.

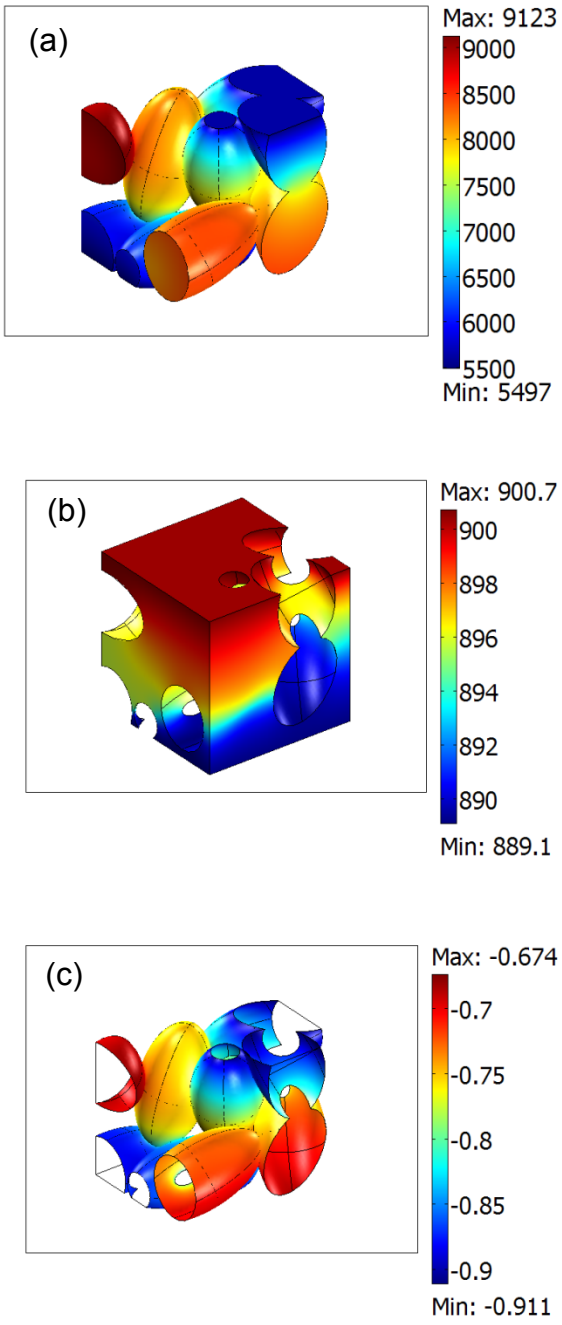

Figure 4.5: Results of a 3D microscopic scale simulation: (a) Li-ion concentration in the solid phase (mol/m^3), (b) Li-ion concentration in the liquid phase (mol/m^3), and (c) reaction current density at the phase interface (A/m^2).

has much higher diffusivity. Figure 4.5 (c) shows that the reaction current flux has the same pattern of distribution as Li ion concentration in the solid phase. This is because the reaction current flux depends on the surface overpotential whose distribution in this case is dominantly determined by open circuit potential, a Li ion concentration dependent material property of the solid active material.

Simulation results from the pseudo 2D model and detailed 3D microscopic model are also compared. The REV is placed at macroscopic mesh node z=130μm. The solutions from pseudo 2D model at z=125 μm and z=135 μm at t=2.173min are used as boundary conditions for 3D microscopic modeling. Due to the stochastic feature of the geometry modeling in detailed 3D microscopic modeling, three realizations of the simulations are conducted, and the averaged results over these three realizations are used. The comparison of specific interfacial area, reaction current density, and volumetric reaction current from both pseudo 2D models and 3D microscopic models are shown in Table 4.4. In Table 4.4, (normalized) reaction current density $\bar{i}$ of the 3D microscopic model is calculated by integrating the local reaction current density over the interfacial area and dividing the integral by the total area A of the interface

$$\bar{i} = \frac{\int_A i\left(c_1, c_2, V_1, V_2\right) \mathrm{d}A}{A}. \tag{34}$$

The volumetric reaction current J_V is calculated by multiplying the interfacial area a with the (normalized) reaction current density. Table 4.4 shows that simulation results from three different realizations are consistent. It is also shown in Table 4.4 that the 3D microscopic model gives large specific interfacial area for electrochemical reactions than the pseudo 2D model. This is because ellipsoidal particles with aspect ratio 2 used in the

Pseudo 2D model					
Particle radius		Volume fraction of solid phase	Specific surface area (m^{-1})	Reaction current density (A/m^2)	Volumetric reaction current (A/m^3)
5.34 μm		0.6	$3.371x10^5$	-1.18	$3.96x10^5$
3D microscopic model					
Variables		Volume fraction of solid phase	Specific surface area (m^{-1})	(Normalized) reaction current density (A/m^2)	Volumetric reaction current (A/m^3)
10 particle cluster	Realization 1	0.526	$4.82x10^5$	-1.01	$-4.88x10^5$
	Realization 2	0.524	$4.59x10^5$	-1.01	$-4.63x10^5$
	Realization 3	0.551	$5.05x10^5$	-0.996	$-5.03x10^5$
	Average	0.534	$4.82x10^5$	-1.01	$-4.85x10^5$
9 particle cluster	Realization 1	0.555	$5.04x10^5$	-0.998	$5.03x10^5$
	Realization 2	0.523	$4.85x10^5$	-1.01	$4.91x10^5$
	Realization 3	0.502	$4.75x10^5$	-1.05	$5.00x10^5$
	Realization 4	0.526	$4.83x10^5$	-1.08	$5.20x10^5$
	Average	0.527	$4.87x10^5$	-1.03	$5.03x10^5$

Table 4.4: Comparison of simulation results from pseudo 2D and 3D microscopic models.

3D microscopic model have larger surface area than spherical particles with the same volume used in the pseudo 2D model. Table 4.4 also shows that the (normalized) reaction current density $\bar{i}$ of the 3D microscopic model is different from that of the pseudo 2D model, because reaction current density is calculated directly using local variables in the 3D microscopic model and reaction current is calculated using volume averaged variables in the pseudo 2D model, as pointed out in Equation (21). In Table 4.4, volumetric reaction current from both models show different values. This implies that the source terms in the macroscopic governing equations derived from the volume averaging technique take different values from these two models. This difference eventually leads to different solutions of the macroscopic governing equations. In other words, the closure terms of volumetric reaction rate provided by pseudo 2D model and 3D microscopic model generate different solutions of the macroscopic governing equations.

To study the effect of the number of particles in the cluster, simulations were also conducted for 9 particle clusters. The simulation results are shown in Table 4.4. The particles used here have the same volume as those used in the 10 particle cluster case. All the other parameters (boundary conditions) used for the simulations are also the same as those used in 10 particle cluster simulation. It is shown in Table 4.4 that simulation results between 9 particle clusters and 10 particle clusters are consistent, which suggests that using 10 particles in the cluster might be sufficient to represent the random microstructure.

Normalized reaction current density from the pseudo 2D model and detailed 3D microscopic model are further compared. The REV is placed at macroscopic mesh node z=175μm. The temporal variations of (normalized) reaction current from two models are

compared as shown in Figure 4.6(a). The curves from two models show completely different temporal variation trends. To explain this discrepancy between two models, a detailed investigation is carried out for microscopic 3D simulations at t=10.77min and t=26.16min. Normalized reaction current densities are -0.78 A/m^2 and -0.23 A/m^2 for t=10.77min and t=26.16min, respectively. Normalized reaction current density is actually the averaged local reaction current density over the interfacial area. Local reaction current densities at the interface for both time instants are shown in Figure 4.6(b) and (c). It could be seen that the local current density distribution spans from -0.915 to -0.696 A/m^2 for t=10.77min, and it spans from -0.0125 to -1.024 A/m^2 for t=26.16min. Therefore, different averaged local reaction current densities for these two time instants are expected. To further understand the different distribution range of local current density for these two time instants, one needs to start from the plateaus in the open circuit potential profile caused by material phase changes. Figure 4.6(d) shows the ranges of open circuit potential distribution for both solutions at these two time instants. Though t=10.77min solution has wider distribution of Li ion concentration in solid phase than t=26.16min solution does, t=10.77min solutions spans a smaller range of open circuit potential than t=26.16min solutions does because t=10.77min solution locates around the plateau region of open circuit potential where phases change is experienced by the active material. A smaller range of open circuit potential results in a smaller range of surface over potential and local reaction current density for t=10.77min solution. Therefore, a big difference is observed in normalized current densities shown in Figure 4.6(a). To summarize, the effect of local variable distribution is very important for the normalized reaction current density. The 3D microscopic model is capable of revealing the local

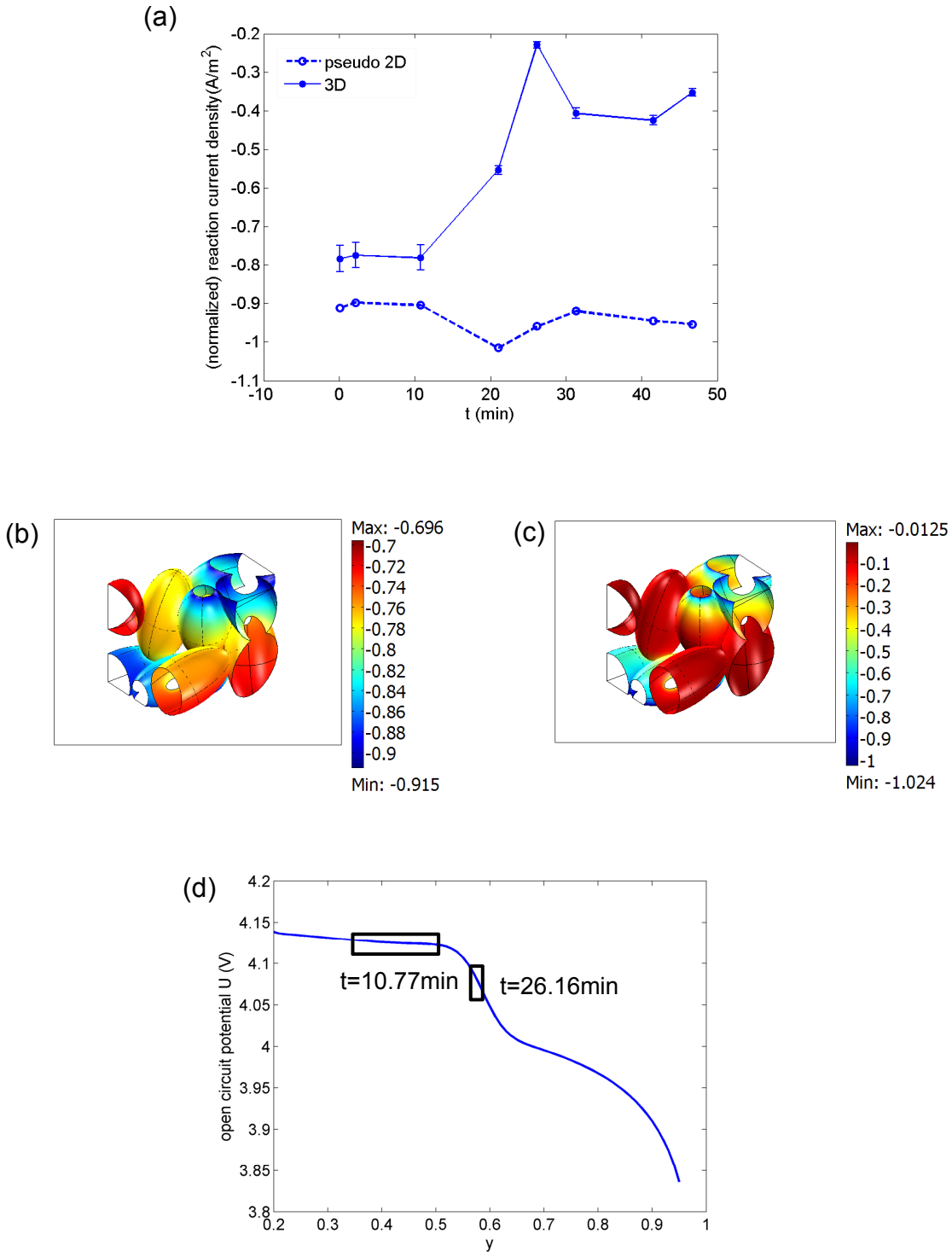

Figure 4.6: Comparison of (normalized) reaction current density: (a) the temporal variation for pseudo 2D and 3D microscopic models, (b) distribution of reaction current density (A/m^2) at t=10.77min by 3D microscopic model, and (c) distribution of reaction current density (A/m^2) at t=26.16min by 3D microscopic model.

distribution of variables. This demonstrates the importance of conducting 3D microscopic modeling.

3.2. Effective Material Property Calculations

The closure terms of effective material properties are calculated directly from 3D microscopic simulations. The calculated results of the ratio between effective and bulk (intrinsic) transport properties are shown in Table 4.5. Since effective transport properties D_2^{eff}, κ^{eff}, κ_D^{eff}, D_1^{eff}, and σ^{eff} are all defined in the same manner ($\overline{D_2\nabla c_2} = D_2^{eff}\nabla\overline{c_2}$, $\overline{\kappa\nabla V_2} = \kappa^{eff}\nabla\overline{V_2}$, $\overline{\kappa_D\nabla(\ln c_2)} = \kappa_D^{eff}\nabla(\overline{\ln c_2})$, $\overline{D_1\nabla c_1} = D_1^{eff}\nabla\overline{c_1}$, $\overline{\sigma\nabla V_1} = \sigma^{eff}\nabla\overline{V_1}$), they should share the same value of the ratio between effective and bulk properties. To calculate the effective materials properties, the generated 3D microstructure is scaled to a cube of 1m×1m×1m, and Poisson's equation $\nabla\cdot(D\nabla c) = 0$ is solved with top and bottom boundary specified as $c(z = 1\text{m}) = 1\ \text{mol/m}^3$, and $c(z = 0\text{m}) = 0\ \text{mol/m}^3$, and other boundaries specified as symmetric. A bulk diffusion coefficient $D^{\text{bulk}} = 1\ \text{m}^2/\text{s}$ is used. The effective diffusivity is calculated as

$$D^{\text{eff}} = \frac{\int_{A(z=1\text{m})} \left(D^{\text{bulk}}\nabla c\right)\text{d}A}{1\text{m}\times 1\text{m}\cdot\left[c(z=1\text{m}) - c(z=0\text{m})\right]/(1\text{m} - 0\text{m})}. \tag{35}$$

The ratio between the effective and bulk diffusivity is

$$\frac{D^{\text{eff}}}{D^{\text{bulk}}} = \frac{1}{1\text{mol/m}^2}\left[\int_{A(z=1)} (\nabla c)\text{d}A\right]. \tag{36}$$

For each of the three realizations of the specified geometry, this calculation is carried out three times by assigning the concentration difference boundary conditions along *x*, *y* and *z* directions respectively. Therefore, nine simulation results for this ratio between the effective and bulk diffusivity are obtained. The averaged value and deviation are calculated. Table 4.5 presents the ratios between effective and bulk (intrinsic) transport

	Bruggeman's Equation	3D microscopic model	
		Average	Deviation (%)
Solid phase	0.465	0.224	5.2
Liquid phase	0.253	0.276	2.5

Table 4.5: Ratio between effective and bulk (intrinsic) transport properties.

properties in solid and liquid phase from the conventional Bruggeman's equation and 3D microscopic simulations. It could be seen that 3D microscopic simulations give very different ratios those given by Bruggeman's equation. It should be pointed out that the effective transport properties for the solid phase of the microstructure depend a lot on the overlapping specified between the particles. It was mentioned that a coefficient of 1.1 was used to multiply the semi-axis of ellipsoids to create an artificial overlapping for a continuous conduction path. A better approach to determine the overlapping coefficient would be using experimentally measured effective and bulk (intrinsic) conductivity and 3D numerical simulations of microstructure for an iterative fitting.

3.3. Surrogate Model Construction for Reaction Current Density

3D microscopic scale simulation results of normalized reaction current density on 317 sampling points in total are used to construct 2nd order polynomial response surface, kriging and radial basis neural network models. The error measures used for evaluating the constructed models are summarized in Table 4.6. PRESS root mean square (RMS) error for all three models is less than 8%. R^2_{adj} for 2nd order polynomial response surface is 0.97, a value very close to one. The error measures suggest that the surrogate models constructed have sufficient accuracy for predicting the objective function, normalized reaction current. Among these three models, kriging has the smallest PRESS RMS, and will be used for further analysis.

To further evaluate the performance of the constructed kriging model, prediction results by the kriging model on 21 testing points are compared with the actual 3D microscopic simulation results. These 21 testing points are sampled using the Latin hypercube filling method to make sure that they do not overlap with any training points

Surrogate model	2^{nd} PRS	Kriging	RBNN
(normalized) PRESS RMS	0.030	0.014	0.074
R^2_{adj}	0.97	-	-

Table 4.6: Evaluation of the constructed surrogate models.

used for surrogate model construction. The error of prediction by the kriging model on these 21 testing points is summarized in Figure 4.7. Figure 4.7 gives the histogram of the prediction error for all 21 points. The horizontal axis is the value of prediction error, and the vertical axis is the number of points (or cases) where the error falls into the range indicated by the bars. As shown in Figure 4.7, most of the testing points have prediction error less than 10% except for 3 points which are found to be close to boundaries of the design space. 16 points have prediction error less than 4.5%. Therefore, the constructed kriging model generally gives good prediction of normalized reaction current density except for some regions close to boundaries. This lack of prediction accuracy in regions close to boundaries can be remedied by using more training points chosen from the boundary regions. The implication of poor prediction for regions close to boundaries is that the construct surrogate model does not accurately predict the current density for extreme cases of very high discharge rates. The constructed kriging model is generally adequate to deal with moderate discharge rates in the multiscale modeling of batteries.

Global sensitivity analysis, which is often used to study the importance of design variables, is conducted to quantify variation of the objective function (normalized reaction current density) caused by the design variables: concentration, electric potential and their gradients in both solid and liquid phases. The importance of design variables is presented by the main factor and total effect indices [30]. The main factor is the fraction of the total variance of the objective function contributed by a particular variable in isolation, while the total effect includes contribution of all partial variances in which the variable of interest is involved (basically by considering those interaction terms in the response surface approximation). The results of calculated main factor and total effect

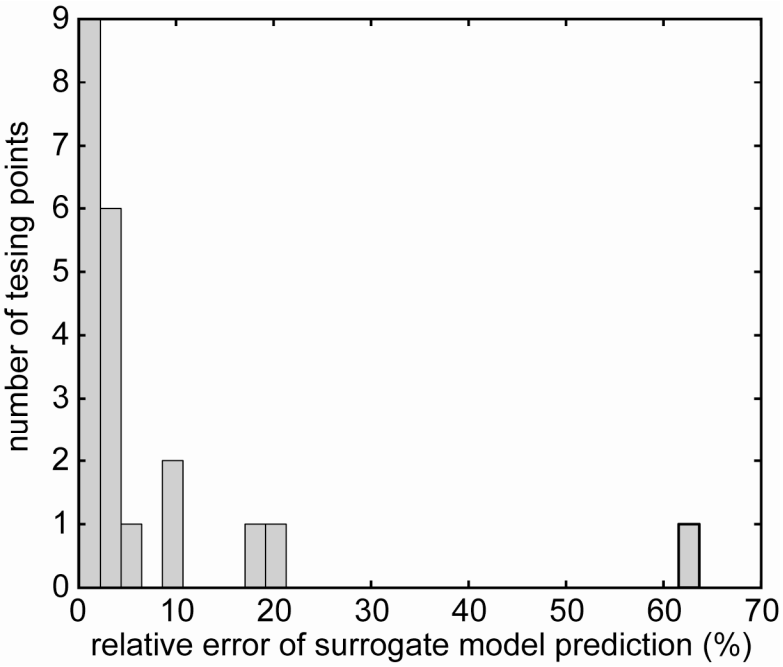

Figure 4.7: Histogram of surrogate model prediction errors on 21 testing points.

indices are shown in Table 4.7. It can be seen that the gradient of variables contribute very little to the variable of the objective function. This is because the ranges of the gradients of the concentration and electric potential variables are chosen based on their distribution on the microscopic scale, while the ranges of the variables themselves are chosen based on their distribution on the macroscopic scale. Table 4.7 also shows that the contribution of variables in the solid phase is larger than those variables in the liquid phase. This is because the solid phase variables dominantly affect the surface overpotential of the electrochemical reactions.

In summary, the constructed surrogate model is capable of predicting the closure term of normalized reaction current density, and will be used for scale bridging in the multiscale modeling framework.

4. CONCLUSIONS

A multiscale framework was proposed to include the electrode microstructure information in battery scale modeling. The resulting closure terms for macroscopic scale governing equations derived from the volume averaging technique were calculated directly from 3D microscopic scale simulations of microstructure consisting of multiple (ellipsoidal) electrode active material particles and liquid electrolyte phase. Comparison of simulation results from 3D microscopic particle clusters and the conventional pseudo 2D models showed that 3D microscopic model (1) gives larger interfacial area for electrochemical reaction; (2) generates different normalized reaction current density (a closure term for the macroscopic scale model) because the 3D microscopic model reveals the local distribution of variables. The calculated effective material properties also

Variable	$\tilde{c}_1$	$\tilde{c}_{1,z}$	V_1	$V_{1,z}$	c_2	$c_{2,z}$	V_2	$V_{2,z}$
Main factor index	0.439	3.50×10^{-5}	0.457	7.41×10^{-5}	0.0020	1.19×10^{-5}	0.020	5.09×10^{-6}
Total effect index	0.517	0.0009	0.533	0.0008	0.0040	0.0001	0.026	0.0002

Table 4.7: Global sensitivity indices calculated from kriging model.

showed very different values from those by the conventional Bruggeman's equation. These suggest the importance and necessity of conducting 3D microscopic modeling and incorporating it into battery scale modeling by the multiscale framework proposed. To efficiently exchange the information between microscopic and macroscopic scales, a surrogate-based approach was proposed for scale bridging. Surrogate models were constructed based on 3D microscopic scale simulation results on sampling points chosen by design of experiments. It was shown that the constructed surrogate models fit the training data of (normalized) reaction current density very well, and they can be used for bridging microscopic and macroscopic scale simulations.

BIBLIOGRAPHY

1. J. Newman and K. Thomas-Alyea, Electrochemical Systems (third edition), John Wiley & Sons, New Jersey, 2004.

2. Y. Chen and J.W. Evans, Three-Dimensional Thermal Modeling of Lithium-Polymer Batteries under Galvanostatic Discharge and Dynamic Power Profile, Journal of the Electrochemical Society, 141, 2947-2955 (1994).

3. X. Zhang, W. Shyy, and A. M. Sastry, Numerical Simulation of Intercalation-Induced Stress in Li-Ion Battery Electrode Particles, Journal of the Electrochemical Society, 154, A910-A916 (2007).

4. M. W. Verbrugge and R. S. Conell, Electrochemical and Thermal Characterization of Battery Modules Commensurate with Electric Vehicle Integration, Journal of The Electrochemical Society, 149, A45-A53 (2002).

5. B. Y. Liaw, G. Nagasubramanian, R. G. Jungst, and D. H. Doughty, Modeling of Lithium Ion Cells – A Simple Equivalent-Circuit Model Approach, Solid State Ionics, 175, 835-839 (2004).

6. P. L. Moss, G. Au, E. J. Plichta, and J. P. Zheng, An Electrical Circuit for Modeling the Dynamic Response of Li-Ion Polymer Batteries, Journal of The Electrochemical Society, 155, A986-A994 (2008).

7. J. Newman and W. Tiedemann, Porous-Electrode Theory with Battery Applications, AIChE Journal, 21, 25-41 (1975).

8. M. Doyle, T. F. Fuller, and J. Newman, Modeling of Galvanostatic Charge and Discharge of the Lithium Polymer Insertion Cell, Journal of The Electrochemical Society, 140, 1526-1533 (1993) .

9. T. F. Fuller, M. Doyle, and J. Newman, Simulation and Optimization of the Dual Lithium Ion Insertion Cell, Journal of The Electrochemical Society, 141, 1-10 (1994).

10. K. Smith and C.-Y. Wang, Solid-State Diffusion Limitations on Pulse Operation of a Lithium Ion Cell for Hybrid Electric Vehicles, Journal of Power Sources, 161, 628–639 (2006).

11. G. Sikha, B. N. Popov, and R. E. White, Effect of Porosity on the Capacity Fade of a Lithium-Ion Battery – Theory, Journal of The Electrochemical Society, 151, A1104-A1114 (2004).

12. X. Zhang, A. M. Sastry, and W. Shyy, Intercalation-Induced Stress and Heat Generation within Single Lithium-Ion Battery Cathode Particles, Journal of The Electrochemical Society, 155, A542-A552 (2008).

13. C.-W. Wang and A. M. Sastry, Mesoscale Modeling of a Li-Ion Polymer Cell, Journal of The Electrochemical Society, 154, A1035-A1047 (2007).

14. W. R. McKinnon and R. R. Haering, Physical Mechanisms of Intercalation. In Modern Aspects of Electrochemistry, No. 15, edited by Ralph E. White et al. Plenum Press, New York (1983).

15. K. E. Thomas, and J. Newman, Thermal Modeling of Porous Insertion Electrodes, Journal of the Electrochemical Society, 150, A176-A192 (2003).

16. Y. Chen and J. W. Evans, Heat Transfer Phenomena in Lithium/Polymer-Electrolyte Batteries for Electric Vehicle Application, Journal of The Electrochemical Society, 140, 1833-1838 (1993).

17. S. C. Chen, C. C. Wan, and Y. Y. Wang, Thermal analysis of lithium-ion batteries, Journal of Power Sources 140, 111–124 (2005).

18. W. Shyy, S. S. Thakur, H. Ouyang, J. Liu, and E. Blosch, Computational Techniques for Complex Transport Phenomena, Cambridge, 1997.

19. U. Hornung (editor), Homogenization and Porous Media, Springer, New York, 1997.

20. E. Sanchez-Palencia, Non-Homogeneous Media and Vibration Theory, edited by J. Ehlers et al, Lecture Notes in Physics, Springer-Verlag, New York, 1980.

21. E. Sozer and W. Shyy, Multi-scale Thermo-fluid Transport in Porous Media, International Journal of Numerical Methods for Heat & Fluid Flow, 18(7/8) 883-899 (2008).

22. P. D. Vidts and R. E. White, Governing Equations for Transport in Porous Electrodes, Journal of The Electrochemical Society, 144, 1343-1353 (1997).

23. W. B. Gu, C. Y. Wang, and B. Y. Liaw, Micro-Macroscopic Coupled Modeling of Batteries and Fuel Cells, Journal of the Electrochemical Society, 145, 3407-3418 (1998).

24. K. K. Patel, J. M. Paulsen, and J. Desilvestro, Numerical Simulation of Porous Networks in Relation to Battery Electrodes and Separators, Journal of Power Sources 122, 144–152 (2003).

25. R. J. M. Smit, W. A. M. Brekelmans, and H. E. H. Meijer, Prediction of the Mechanical Behavior of Nonlinear Heterogeneous Systems by Multi-Level Finite Element Modeling, Computer Methods in Applied Mechanics and Engineering, 155, 181-192 (1998).

26. V. Kouznetsova, W. A. M. Brekelmans, and F. P. T. Baaijens, An Approach to Micro-Macro Modeling of Heterogeneous Materials, Computational Mechanics 27, 37-48 (2001).

27. W. E, B. Engquist, X. Li, W. Ren, and E. Vanden-Eijnden, Heterogeneous Multiscale Methods: a Review, Communications in Computational Physics, 2, 367-450 (2007).

28. L. Tan and N. Zabaras, Multiscale Modeling of Alloy Solidification Using a Database Approach, Journal of Computational Physics 227, 728–754 (2007).

29. O. Rohrle, J. B. Davidson, and A. J. Pullan, Bridging Scales: A Three-Dimensional Electromechanical Finite Element Model of Skeletal Muscle, SIAM Journal on Scientific Computing, 30, 2882–2904 (2008).

30. N. V. Queipo, R. T. Haftka, W. Shyy, T. Goel, R. Vaidyanathan, and P. K. Tucker, Surrogate-based Analysis and Optimization, Progress in Aerospace Sciences, 41, 1-28 (2005).

31. A. Donev, F. H. Stillinger, and S. Torquato, Neighbor List Collision-Driven Molecular Dynamics Simulation for Nonspherical Particles. I. Algorithmic Details II. Applications to Ellipses and Ellipsoids, Journal of Computational Physics, 202, 737-764 (part I) and 765-793 (part II) (2005).

32. J. I. Madsen, W. Shyy and R. T. Haftka, Response Surface Techniques for Diffuser Shape Optimization, AIAA Journal, 38, 1512-1518 (2000).

33. T. Goel, R. Vaidyanathan, R. T. Haftka, W. Shyy, N. V. Queipo, and K. Tucker, Response Surface Approximation of Pareto Optimal Front in Multi-Objective Optimization, Computer Methods in Applied Mechanics and Engineering, 196, 879–893 (2007).

34. R. H. Myers, and D. C. Montgomery, Response Surface Methodology: Process and Product Optimization Using Designed Experiments, pp. 17-48, John Wiley & Sons Inc: New York, 1995.

CHAPTER V

CONCLUSIONS AND FUTURE WORK

To improve Li-ion battery performance for application in electrifying automotive drivetrains, this study focuses on (1) improving calendar life by reducing performance degradation due to stress-induced electrode particle fracture and heat generation through modeling and numerical simulations, and (2) creating models including electrode materials microstructural information for computer simulations that can lead to optimizing battery design for improved energy output per unit volume and mass.

An intercalation-induced stress model with the analogy to thermal stress modeling was proposed to determine localized intercalation-induced stress in electrode particles. Intercalation-induced stress was first calculated within ellipsoidal electrode particles with a constant diffusion flux assumed at the particle surface. It was found that internal stress gradients significantly enhance diffusion. Simulation results suggest that it is desirable to synthesize electrode particles with smaller sizes and larger aspect ratios, to reduce intercalation-induced stress during cycling of lithium-ion batteries.

Stress and heat generation were modeled for single ellipsoidal particles under potentiodynamic control, in which case the flux at particle surface is determined by electrochemical kinetics, Butler-Volmer equation. It was found that Li-ion concentration, surface flux, and intercalation-induced stress are highly correlated through the diffusion process, electrochemical kinetics and the intercalation-induced lattice expansion. The two

peaks observed in the flux and stress generation plots were attributable to intrinsic material properties (two plateaus in the OCP) of the material studied ($LiMn_2O_4$) and the applied potential. The heat of mixing was found to be negligible (two orders of magnitude smaller than the other two sources) and resistive heat was identified as the heat generation source of greatest importance. To systematically investigate how intercalation-induced stress and resistive heat generation are affected by electrode particle geometric shape and cycling rate, a surrogate-based analysis was conducted. It was shown that smaller sizes and larger aspect ratios of (prolate) particles reduce the heat and stress generation inside electrode particles.

A multiscale framework was proposed to include the electrode microstructure information in battery scale modeling. The resulting closure terms for macroscopic scale governing equations derived from the volume averaging technique were calculated directly from 3D microscopic scale simulations of microstructure consisting of multiple (ellipsoidal) electrode particles and liquid electrolyte. Comparison of simulation results from 3D microscopic particle clusters and the conventional pseudo 2D models showed that the 3D microscopic model (1) gives larger interfacial area for electrochemical reaction; (2) generates different normalized reaction current density (a closure term for the macroscopic scale model) because the 3D microscopic model reveals the local distribution of variables. This suggests the importance and necessity of conducting 3D microscopic modeling and incorporating it into battery scale modeling by the multiscale framework proposed. To efficiently exchange the information between microscopic and macroscopic scales, a surrogate-based approach was proposed for scale bridging. Surrogate models were constructed based on 3D microscopic scale simulation results on

sampling points chosen by design of experiments. The inputs for surrogate models are boundary conditions for 3D microscopic scale simulations taken from the nodal values of macroscopic scale simulations. The output is the (normalized) reaction current density for closure term in macroscopic scale simulations. It was shown that the constructed surrogate models fit the training data very well and give good prediction of the closure term modeled, reaction current density.

Future work is proposed in the following areas:

- Use the constructed surrogate models for the closure term of volumetric reaction rate to complete the multiscale modeling framework.
- Incorporate material phase change in the diffusion and intercalation-induced stress modeling. It is well know that electrode active materials undergo phase change during intercalation and deintercalation. Different phases of the material have different diffusion coefficient and structural properties. It is important to include this phase change information into models.
- Include stress analysis and heat generation and transfer modules into the proposed multiscale modeling framework. In this study, stress and heat generation were studied for single electrode particles. With the understanding of stress and heat generation mechanisms inside single particles, it is necessary to analyze stress and heat transfer on the cell scale to further understand the effect of electrode microstructure on stress generation and heat generation and transfer.
- Further explore the effect of 3D microstructure on battery performance. A fixed set of microstructure characteristic parameters were used in this study. It is necessary to improve the robustness of the geometry modeling and meshing

process so that it is feasible to fully explore the effect of the 3D microstructure of electrode materials.

- Further explore the application of the surrogate-based approach for modeling and optimization. Surrogate models are reduced order models with adequate fidelity. They predict the objective functions efficiently compared to physics-based models. For example, surrogate models can be potentially used for battery control algorithms where rapid prediction of state variables is required. Furthermore, surrogate models can also be used for design optimization purpose. Design adjustable parameters for a Li-ion cell include electrode thickness, volume fractions of active material, conductive additives, and electrolyte in the electrode, electrode particle size, separator thickness, and other adjustable material properties. The objective functions for optimization can include cost, energy and power output. The surrogate-based approach can be used to deal with this kind of high dimensional multi-objective design optimization problem based on either experimental or computational results.